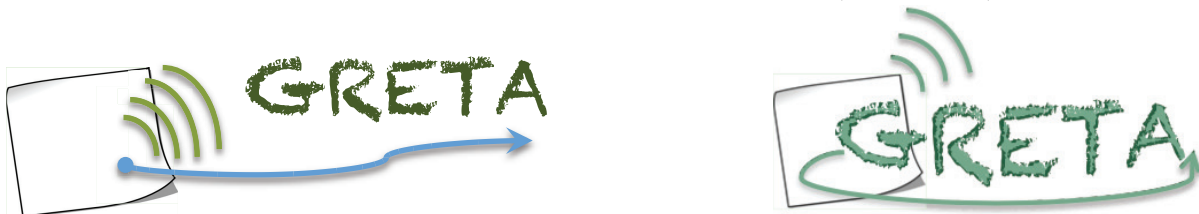


Ministero dell'Istruzione, dell'Università e della Ricerca
PROGRAMMI DI RICERCA SCIENTIFICA DI RILEVANTE INTERESSE NAZIONALE
(PRIN)
Anno 2010-2011 - Progetto GRETA, prot. 2010WHY5PR

ETICHETTE E SENSORI ECO-COMPATIBILI LOCALIZZABILI ED
IDENTIFICABILI CON TECNICHE WIRELESS A BANDA ULTRA LARGA

**GREEN TAGS AND SENSORS WITH UTRAWIDEBAND IDENTIFICATION
AND LOCALIZATION CAPABILITIES (GRETA)**



GRETA
Deliverable Number: D2
Report on the First Year of Activity

Date of Delivery: March 2014 (T0+12)

Editor(s): Anna Guerra, Francesco Guidi, Davide Dardari

Participating institutions: UNIAQ, UNIBO, UNIFE, UNIPG, UNIPV

Contributors: UNIAQ, UNIBO, UNIFE, UNIPG, UNIPV

Workpackage number: WP1-WP2-WP3

Nature: R

Dissemination Level: Public

Version: final

Abstract:

This document focuses on the set of possible technologies that can be considered in the project GRETA (GReen TAgS and sensors with ultra-wide-band identification and localization capabilities), concerning both energy efficient communication schemes between the reader and tags, and "green" technologies that can be adopted to implement the tags.

An overall description of the first year's achievements of GRETA is initially given by summarizing the main topics addressed.

Subsequently, some reader and tag architectures and their respective technologies, which are suitable to achieve the project requirements, are proposed and analyzed with the objective to obtain energy autonomous tags able to harvest sufficient energy from the surrounding environment through ultra-high frequency (UHF) antennas.

A link budget and power analysis for each architecture is presented to identify the best network configuration for maximal area coverage in the proposed scenarios.

Finally, a preliminary demonstrator architecture which will be set up to provide a first experimental assessment of the system is illustrated.

Keyword list: RFID, UWB, Green, energy harvesting, localization

CONTENTS

List of acronyms	5
1 Introduction	17
1.1 Notation	17
2 Summary of 1st Year of Activity	19
2.1 Typical application cases and Reference Scenario	20
2.2 GRETA Specifications Refinement	20
2.2.1 Performance Metrics	20
2.2.2 Specifications	22
3 Architecture and Technologies	23
3.1 Introduction	23
3.2 General System Architecture	23
3.3 Reader-Tag Architecture Solutions	25
3.4 Tag Architectures Investigated	26
3.4.1 Reader-Tag Architectures Suitable for the Project	28
3.5 Signal Format	29
3.5.1 Stand-Alone ultra-wide band (UWB)-UHF Tag Communication Scheme	29
3.5.2 UWB as Add-On of Standard Gen.2 UHF Tag Communication Scheme	31
3.5.3 Interrogation signal	32
3.5.4 Tag Timing	34
3.5.5 Tags Codes Design	35
3.6 Synchronization Schemes	39
3.6.1 Clock synchronization	40
3.6.2 Code synchronization	40
3.7 Energy harvesting component	41
3.8 Sensor component	43
3.9 UWB backscatter modulator	44
3.9.1 Preliminary study with lumped diodes	48
3.10 Antenna system	49
3.10.1 Harvester antenna	49
3.11 Green Technologies	53
3.11.1 Selection and EM characterization of paper-based substrates	53
3.11.2 Design of paper-based transmission lines	59
3.11.3 Design and fabrication of paper-based SIW interconnects	66
3.12 Localization and tracking algorithm	67
3.12.1 Bayesian Filtering	69
3.12.2 Case Study: Order of Arrival Estimation via Bayesian Tracking	70
3.13 Network Management Protocols	74
3.13.1 Anti-collision schemes	75
3.13.2 Spread-spectrum sequences	75
3.13.3 Spread-spectrum model for RFID tags	76
3.13.4 Preliminary results for the spread-spectrum model	78
3.13.5 ISO/IEC 18000-6C anti-collision protocol	80
3.13.6 Proposed algorithm for fast identification with ISO/IEC 18000-6C MAC	81
3.13.7 Preliminary results for the proposed enhancement of ISO/IEC 18000-6C MAC	82

4 Link and Power Budget	84
4.1 Link budget	84
4.1.1 Channel Path Loss	84
4.1.2 Link Budget Analysis	86
4.1.3 Coverage Results	88
4.2 Power budget	94
5 Demonstrator Definition	97
5.1 University of Bologna	97
5.2 University of Ferrara	97
5.3 University of Perugia	97
6 Dissemination Activity	99
6.1 University of Bologna	99
6.2 University of Ferrara	100
6.3 University of L'Aquila	100
6.4 University of Pavia	100
6.5 University of Perugia	101
References	102

LIST OF ACRONYMS

ADC	analog-to-digital converter
AF	amplify-and-forward
AFL	anchor-free localization
ACK	acknowledge
AGNSS	assisted-GNSS
AGPS	assisted GPS
AltBOC	alternate binary offset carrier
AOA	angle-of-arrival
AOD	angle of departure
AP	access point
API	application programming interface
ARNS	aeronautical radio navigation services
A-S	anti-spoofing
AS	azimuth spread
ASIC	application specific integrated circuit
AWGN	additive white Gaussian noise
BCH	Bose-Chaudhuri-Hocquenghem
BEP	bit error probability
BER	bit error rate
BLAS	basic linear algebra subprograms
BOC	binary offset carrier
bps	bits per second
BPSK	binary phase shift keying
BPZF	band-pass zonal filter
BS	base station
BSC	binary symmetric channel
C/A	coarse/acquisition
C/NAV	commercial/navigation
CAD	Computer Aided Design
CAP	contention access period

CAWGN	complex additive white Gaussian noise
CBOC	composite binary offset carrier
CC	central cluster
cdf	cumulative distribution function
CDF	cumulative density function
CDMA	code division multiple access
CF	characteristic function
CFP	contention free period
CH	cluster head
CIR	channel impulse response
CKF	cubature Kalman filter
CL	civil-long
CM	civil-moderate
CMOS	Complementary Metal Oxide Semiconductor
Coop-POCS	cooperative projection onto convex sets (POCS)
Coop-OA	cooperative outer-approximation (OA)
COTS	commercial off-the-shelf
CNLS	constrained non-linear least squares (NLS)
CNSS	Compass navigation satellite system
CPR	channel pulse response
cps	chips per second
CRB	Cramér-Rao bound
CRLB	Cramér-Rao lower bound
CRC	cyclic redundancy check
CRPF	cost reference particle filter
CS	control segment/commercial service
CSI	channel state information
CSS	chirp spread spectrum
CTS	clear-to-send
CW	continuos wave
DAA	Detect and Avoid

DC	Direct Current
DGPS	differential GPS
DIFS	DCF inter-frame spacing
DM	data mining
DMLL	distributed maximum log-likelihood
DLL	delay-locked loop
DOA	Direction of Arrival
DoD	Department of Defense
DP	direct path
DPE	direct position estimation
DS	delay spread
DSSS	direct sequence spread spectrum
dwMDS	distributed weighted multidimensional scaling
EB	energy-based
EBG	Electromagnetic Band Gap
ECEF	Earth-centered, Earth-fixed
ED	energy detector
EGNOS	European geostationary navigation overlay system
EH	energy harvesting
EIRP	effective isotropic radiated power
EKF	extended Kalman filter
EKFBT	extended Kalman filter with bias tracking
e.m.	electro-magnetic
EPE	Ekahau positioning engine
ERP	Effective Radiated Power
ERQ	enhanced robust quad
ESA	European Space Agency
EU	European Union
F/NAV	freely accessible navigation
FET	field-effect transistor
FCC	federal communications commission

FDMA	frequency division multiple access
FEC	forward error correction
FFD	full function device
FIM	Fisher information matrix
FLL	Frequency-locked loop
FOC	full operational capability
FOM	figure of merit
FPGA	field programmable gate array
FPK	Flächen-Korrektur-Parameter (area correction parameters)
GAGAN	GPS aided GEO augmented navigation
GANSS	Galileo/Additional navigation satellite systems
GDOP	geometric dilution of precision
GEO	geostationary
GIOVE	Galileo In-Orbit Validation Element
GIS	geographical information system
GLONASS	global orbiting navigation satellite system
GML	generalized maximum likelihood
GNSS	global navigation satellite system
GPRS	general packet radio service
GPS	global positioning system
GS	geodetic system
GSM	Global System for Mobile communications
HB	Harmonic Balance
hdwMDS	hybrid dwMDS
HEO	highly-inclined elliptical orbits
HMM	hidden Markov model
HOW	handover word
HPOCS	hybrid POCS
HW	hardware
i.i.d.	independent,identically distributed
I/NAV	integrity/navigation

ICD	interface control document
ICT	information and communication technologies
IC	integrated circuit
ID	IDentification
IE	informative element
IF	intermediated frequency
IGSO	inclined geosynchronous orbit
ILS	instrument landing system
IMU	inertial measurement unit
INS	inertial navigation system
IRNSS	regional navigation satellite system
IR-UWB	impulse radio UWB
ISM	industrial scientific medical
ISRO	Indian space research organization
IST	information society technologies
IVP	inertial virtual platform
JBSF	jump back and search forward
KDD	Knowledge Discovery
KF	Kalman filter
KNN	k-nearest-neighbor
LAAS	local area augmentation system
LAN	local area network
LAPACK	linear algebra package
LBS	location-based services
LCS	location services
LDC	low duty-cycle
LDPC	low density parity check
LDR	low data rate
LEO	Localization Error Outage
LLC	logical link control
LLR	log-likelihood ratio

LLS	linear least squares
LOB	line-of-bearing
LOS	line-of-sight
LR	likelihood ratio
LRT	likelihood ratio test
LS	least-squares
LSE	least squares estimator
MAC	medium access control
MAP	maximum a posteriori
MBOC	multiplexed binary offset carrier
MB-UWB	multi-band UWB
MPP	maximum power point
MPPT	maximum power point tracking
MCRB	modified Cramér–Rao bound
MDS	multi-dimensional scaling
MEMS	micro-electro-mechanical systems
MESS	maximum energy sum selection
MEO	medium earth orbit
MF	matched filter
MGF	moment generating function
MHT	multiple hypotheses testing
MIMO	multiple-input multiple-output
MISO	multiple-input single-output
ML	maximum likelihood
MLE	maximum likelihood estimator
MMSE	minimum mean squared error
MQKF	multiple quadrature Kalman filtering
MRC	maximal ratio combining
MS	mobile station
MSAS	multi-functional satellite augmentation system
MSB	most significant bit

MSE	mean squared error
MSK	Minimum-shift Keying
MST	minimum spanning tree
MTSAT	multi-functional transport satellite
MUI	multi-user interference
N/A	not available
NAV	navigation
NAVSTAR	navigation system for timing and ranging
NB	narrowband
NBI	narrowband interference
NDIS	network driver interface specification
NG	network green
NLOS	non-line-of-sight
NLS	non-linear least squares
NN	neural network
NPE	Navizon positioning engine
NQRT	new quad robustness test
NRZ	non-return to zero
NSI5	non-standard I5
NSQ5	non-standard Q5
NTP	network time protocol
OA	outer-approximation
OCS	operational control segment
OFDM	orthogonal frequency division multiplexing
OMA	open mobile alliance
OOK	on-off keying
O-QPSK	offset quadrature shift keying
OQRT	original quad robustness test
ORQ	original robust quad
OS	open service
OTDOA	observed TDOA

P2P	peer-to-peer
PIE	Pulse Interval Encoding
P2PP	P2P-positioning
PAM	pulse amplitude modulation
PAN	personal area network
PDA	personal digital assistant
pdf	probability density function
PDP	power delay profile
PF	particle filter
PHY	physical layer
PLL	phase-locked loop
PMU	Power Management Unit
PN	pseudo-noise
POC	payload operation center
POCS	projection onto convex sets
PN	pseudo-noise
PPM	pulse position modulation
PPS	precise position service
PR	Pseudo-random
PRN	pseudo-random noise
PRS	public regulated service
PRT	partial robustness test
PSD	power spectral density
PSDP	power spatial delay profile
PSK	phase shift keying
pTOA	pseudo time of arrival
PV	position-velocity
PVT	position, velocity, and time
QKF	quadrature Kalman filter
QZSS	quasi-zenith satellite system
RDSS	radio determination satellite service

RF	radio frequency
RFD	reduced function device
RFID	Radio frequency identification
R-GML	reduced complexity generalized maximum likelihood
RIMS	ranging and integrity monitoring stations
RLE	robust location estimation
RMS	root-mean square
RMSE	root mean square error
RMU	remote measurement unit
RNSS	regional navigation satellite system
ROC	receiver operating characteristics
RQ	robust quadrilateral
RRC	root raised cosine/radio resource control
RRLP	radius resource location protocol
RSMB	root square of mean biased value
RSS	received signal strength
RT	robust trilateration
RTCM	radio technical commission for maritime services
RTLS	real-time locating systems
RTK	real-time kinematic
RTS	ready-to-send
RTT	round-trip time
r.v.	random variable
RV	random variable
SA	selective availability
SAR	search and rescue
SAW	surface acoustic wave
SBAS	satellite-based augmentation system
SBS	serial backward search
SBSMC	serial backward search for multiple clusters
SCKF	square-root cubature Kalman filter

SDR	software defined radio
SDS	symmetric double sided
SET	SUPL enabled terminal
S-GML	soft generalized maximum likelihood
SIR	sequential importance resampling
SLP	SUPL location platform
SIFS	short inter frame spacing
SIMO	single-input multiple-output
SIS	signal-in-space
SISO	single-input single-output
SMD	Surface Mounting Device
SoA	state-of-the-art
SoL	safety-of-life
SMC	sequential Monte Carlo
SNR	signal-to-noise ratio
SNIR	signal-to-noise-plus-interference ratio
SPAWN	sum and product algorithm over a wireless network
SPKF	sigma-point Kalman filter
sps	symbols per second
SPS	standard position service
SQKF	square-root quadrature Kalman filter
SRN	secondary reference nodes
SS	spread spectrum/space segment
ST	simple thresholding
SUPL	secure user-plane location
SV	satellite vehicle
SW	software
SIW	substrate integrated waveguide
TDMA	time division multiple access
TDOA	time difference-of-arrival
TDR	Time-domain reflectometry

TI	trilateration intersection
TFTC	Thin Film Transistor Circuit
TLM	telemetry
TMBOC	time-multiplexed binary offset carrier
TOA	time-of-arrival
TOF	time-of-flight
TOW	time of week
TH	time-hopping
TNR	normalized threshold
TTFF	time-to-first-fix
TW-TOA	two-way-TOA
U.S.	United States
UE	user equipment
UERE	user equivalent range error
UHF	ultra high frequency
UKF	unscented Kalman filter
ULP	user location protocol
UMTS	universal mobile telecommunications system
URE	user range error
US	user segment
UL	uplink
UT	user terminal
UTC	coordinated universal time
UTM	universal transverse Mercator
UTRA	UMTS terrestrial radio access
UWB	ultra-wide band
UWB-IR	ultra-wide band impulse radio
VANET	vehicular ad-hoc network
VRS	virtual reference station
WAAS	wide area augmentation system
WADGPS	wide area differential GPS

WARN	wide area reference network
WB	wideband
WE	wireless extensions
WGS84	world geodetic system
WiMAX	worldwide interoperability for microwave access
WLAN	wireless local area network
WLS	weighted least squares
WMAN	wireless metropolitan area network
WPAN	wireless personal area network
WR API	wireless research application programming interface
WSN	wireless sensor network
WT	wireless tools
WWB	Weiss-Weinstein bound
ZZB	Ziv-Zakai lower bound
ZZBT	Ziv-Zakai Bellini-Tartara

1 INTRODUCTION

The present deliverable provides an overall description of the first year's achievements of GRETA project (GReen TAgS and sensors with ultra-wide-band identification and localization capabilities). The main purpose of this project is to realize a demonstrator of a wireless ecological system for identification, tracking, and monitoring of mobile subjects adopting zero-power ultra-wide band (UWB) communication techniques, energy harvesting solutions and eco-compatible materials. First of all, the identification of reference applications, requirements and scenarios has lead to designate three possible field of interests:

- eHealth for biomedical and hospital scenarios;
- ICT for food for the production and commercial distribution chain;
- Logistic.

Once the possible scenarios had been defined, the most significant performance metrics (i.e. the maximum tolerable localization uncertainty, detection probability, bit error probability..) have been investigated. Different different tag and network architectures have been compared and an analysis of the benefits and of the drawbacks for each of them is provided. In particular, four types of tags have been taken into consideration: active tags, UWB-UHF stand alone tags, UWB as an add on of UHF Gen. 2 Standard tags and active reflector tags. The two passive tag architectures based on UWB backscatter communication have been selected thanks to their extremely low energy consumption and the possibility to adopt energy harvesting techniques via UHF RF signals. In fact the energy necessary for communication is harvested from the interrogator device's signal, and no radio-frequency (RF) circuits such as amplifiers, oscillators, converters are required in the tag. Thus the main cause of energy consumption is the RF switch and the relative digital control logic, whereas the link budget is bounded only by the interrogator device power constraints. Both the selected architectures present interesting aspects: the high level of innovation for the former and the compatibility with previous standard for the latter. For these reasons both will be investigated by means of a modular approach. The two selected architectures have then been investigated from a communication and technological point-of-view.

This report is organized as follows.

Section 2 contains a summary of the activity carried out during the first year of GRETA project.

The purpose of the *Section 3* is to provide a detailed explanation of the general system architecture: different tag solutions are reported and analyzed, the communication scheme of the reader-tag system chosen is detailed, the synchronization procedure is described and in conclusion, some localization and tracking algorithms are presented. Some technological aspects are investigated such as the antenna and energy harvester circuits. In addition, the selection and characterization of the paper-based substrates is provided with the purpose to design a green tag.

Section 4 provides a link and power budget analysis.

In *Section 5* a description of an experimental test-bed to perform a preliminary measurement campaign is reported.

Finally, *Section 6* the dissemination plan of each unit is reported.

1.1 Notation

Hereafter the main mathematical notation rules used throughout the text are listed for the reader convenience. Meanings and formats will be maintained along the text, unless otherwise stated.

x, y, z, \dots	scalar variables, either deterministic or stochastic (depending on the context), either real or complex (depending on the context).
$\mathbf{a}, \mathbf{b}, \mathbf{c}, \dots$	vector variables, column-wise defined, either deterministic or stochastic, either real or complex.
$\mathbf{A}, \mathbf{B}, \mathbf{C}, \dots$	matrix variables, either deterministic or stochastic, either real or complex.
\mathbb{R}^M	Field of the real numbers, M -dimensional.
\mathbb{C}^M	Field of the complex numbers, M -dimensional.
$\mathbf{a} \in \mathbb{R}^M$	M -element real vector.
$\mathbf{b} \in \mathbb{C}^N$	N -element complex vector.
$\mathbf{A} \in \mathbb{R}^{M,N}$	Real matrix, with M rows and N columns.
$\Re\{\cdot\}$	Real part.
$\Im\{\cdot\}$	Imaginary part.
$(\cdot)^T$	Transpose operator.
$(\cdot)^*$	Complex conjugate operator.
$(\cdot)^H$	Hermitian operator (transpose, complex conjugate).
$(\cdot)^\dagger$	Moore-Penrose pseudo-inverse.
$\mathbf{A} \succeq \mathbf{B}$	The matrix $(\mathbf{A} - \mathbf{B})$ is nonnegative definite.
$\mathbf{A} \succ \mathbf{B}$	The matrix $(\mathbf{A} - \mathbf{B})$ is positive definite.
$\mathbb{E}\{\cdot\}$	Expected value (stochastic) operator.
\triangleq	Equal by definition.
$\nabla_{\mathbf{x}}(\mathbf{d}(\mathbf{x}))$	Jacobian matrix (partial derivatives of $\mathbf{d}(\mathbf{x})$ w.r.t. \mathbf{x}).
$g(t)$	Function of a continuous variable. E.g., signal or process as a function of the continuous time.
$g[n]$	Function of a discrete variable. E.g., signal or process in the discrete time domain.
f_c	Carrier or central frequency.
B_W	Bandwidth
f_s	Sampling frequency.
T_c	Chip interval.
T_s	Symbol/Pulse interval.
c	Speed of light.
τ_{mean}	Mean excess delay.
σ_τ	Delay spread (RMS).
$P(\cdot)$	Power or Probability (depending on the context).
$p(\cdot)$	Probability density function.
d	Distance (in meters).
(x, y, z)	Cartesian coordinates of a point.

2 SUMMARY OF 1ST YEAR OF ACTIVITY

During the first year of GRETA project, different aspects have been investigated from the system and technological point of view.

From the system architecture perspective, various potential solutions have been analyzed corresponding to different impacts in terms of energy consumption, complexity and performance. Specifically, both active and passive architectures, the latter based on UWB backscatter modulation, have been considered. For each solution link budget and coverage analysis have been carried out. To overcome the limited coverage obtained when using passive tags, some solutions have been proposed. Specifically, multiple low-complexity transmitters have been considered to be placed on the ceiling (multi-static scenario) that act as energy and signal "showers". Simulation results have shown the beneficial impact of the multi-static solution, especially in rooms with reduced height. Summarizing, the following considerations can be remarked:

- very limited link-budget available in backscatter mode (passive tags);
- active tags provide a good coverage but they are not adoptable for the project due to their incompatibility with energy harvesting techniques;
- the adoption of showers (multi-static scenario) can increase the coverage for moderate roof heights;
- the use of non-regenerative relays improves the coverage in the presence of obstacles.

Among the different communication strategies investigated, the following have been considered compatible with GRETA requirements: UWB for ranging and communication and UHF for energy harvesting and synchronization; UWB for ranging and UHF for communication (Gen.2 compatible) and energy harvesting. Both strategies make use of UHF and UWB signaling in backscatter mode to realize very low power consumption tags. The UHF channel is also adopted to provide the tag the sufficient energy to power up. Suitable communication protocols has been defined in addition to the corresponding parameters.

Time synchronization is the main critical aspect in backscattered UWB communications. Two important aspects concerning synchronization have been distinguished: clock synchronization and code synchronization; Code synchronization is achieved in two steps. First, the reader should synchronize with the tag code. Once the reader and tag are aligned, the reader needs to estimate the signal time-of-arrival (TOA) estimation for fine synchronization. An investigation of the synchronization problem in terms of procedures, algorithms and architecture in both scenarios is a major near term research topic.

The localization and tracking process typically consists of two phases: (i) a measurement phase, during which readers make position-dependent measurements; (ii) a location-update phase, during which tags positions are inferred using an algorithm that incorporates both prior knowledge of their positions and new measurements. The measurement process has a crucial impact on the overall system tag localization accuracy. In the scenarios of GRETA the requirement on localization accuracy is stringent and the link budget of backscattered pulse is poor. TOA-based ranging techniques are adopted to exploit the properties of UWB signals. Preliminary results about the localization error in line-of-sight (LOS) and obstructed-line-of-sight (OLOS) conditions, have been shown. In the next period, the research activity will also investigate hybrid angle-of-arrival (AOA)-TOA localization approaches.

From network management protocols point of view two levels of data exchange have been identified: Tag-Reader and Reader-to-Reader; these two communication levels of the network architecture have different requirements and energy constraints, which are related to the protocols used to manage the system. While the tag-reader communication is more complex, the communication among readers is less critical from a power consumption perspective because their energy budget is usually not an issue. In reader-to-tag communication the collision problem is very relevant while the main issue in readers communication happens when more than one reader is interrogating the same tags; in this case redundant readings have to be avoided by means of cooperation among nodes. For all these reasons, the main challenge is to guarantee deadlines while delivering messages; for this purpose specific protocols are needed to ensure that all readers will be able to satisfy the delivery requirements and deadlines imposed by the applications. Main parameters as number of nodes, distance among readers, latency, variability,

number of gateways, reader capabilities, etc... have to be defined to start the analysis of realistic scenario.

From technological point of view, an overview of the innovative substrate integrated waveguide (SIW) technology, have been provided, in conjunction with eco-friendly materials and manufacturing techniques, considering that planar technologies represent the ideal choice for the implementation of microwave and mm-wave integrated complex circuitry. Different types of antenna design, that combines the characteristic of being planar and exploit SIW technology, have been considered; the most common structures are the SIW slot array antenna, the SIW leaky-wave antenna, and the SIW cavity-backed slot antenna.

For the harvester antenna a highly efficient rectifying antenna (rectenna), able to collect energy from the environment and to provide sufficient Direct Current (DC) power to supply the entire GRETA system, has been proposed. In the analysis of the proposed solutions, the effect of the use of paper substrate has been taken into consideration. A conversion RF-DC circuit have been proposed and the rectified powered estimated.

The operating principle of the UWB backscatter modulator for passive tag architectures has been presented. Two different architectures, based on diodes and transistors, have been proposed in agreement with a further fabrication with off-the-shelf components and with the integrated circuit (IC) design, respectively.

Particular attention has been reserved to the role played by the sensor electrical interface; transduced quantities have to be detected and converted into digital form with satisfactory accuracy, repeatability, and precision. In GRETA, one of the most challenging issues is the definition of an acceptable trade-off between the energy consumption and performance. The proposed sensing electrical interface will be designed for being compatible with generic impedance sensors.

2.1 Typical application cases and Reference Scenario

The proposed technology, with its characteristic of eco-compatibility, energy autonomy, and sensing abilities, can be used to implement smart tags in various areas of application:

- **eHealth:** energetically autonomous and not invasive sensors for biomedical or drugs monitoring, and in general for efficient hospital management (blood bags tracker, smart band aid, temperature sensor, smart plasters).
- **ICT for food:** on-paper tags with embedded sensors (temperature, humidity, air composition) for continuous monitoring of the product along the production and commercial distribution chain (e.g. cold chain, ...).
- **Logistic:** goods tracking and monitoring along the industrial process (sorting in conveyor belts, store inventory, green smart shelf, supply chain management, ...).

2.2 GRETA Specifications Refinement

2.2.1 Performance Metrics

We list a series of indicators which serve to evaluate the quality of the performance of the system in different situations: when tags have to be detected, when their positions have to be inferred and when they should be tracked or ordered.

During reader-tag communication, the first task that has to be accomplished is tag detection. In this case, meaningful performance indexes for the tag's detection are the probability of detection P_D and the false alarm probability P_F : respectively, the probability that the tag is correctly detected when it is effectively present in the scenario and the probability that, due to interference and noise, the tag is detected even if it is not present in the considered environment respectively. Formally, given a binary hypothesis set ($\{\mathcal{H}_0, \mathcal{H}_1\} = \{\text{tag is absent}, \text{tag is present}\}$) and two possible decisions ($\{\mathcal{D}_0, \mathcal{D}_1\} =$

{decide for \mathcal{H}_0 , decide for $\mathcal{H}_1\}$), we have:

$$P_D = P(\mathcal{D}_1 | \mathcal{H}_1) \quad (1)$$

$$P_F = P(\mathcal{D}_1 | \mathcal{H}_0) \quad (2)$$

Typically, binary detection is accomplished by comparing the sufficient statistics, extracted from the received signal, with a suitable threshold. The choice of the threshold affects the performance of the detection scheme in terms of probability of detection and probability of false alarm. Low values for the threshold lead to higher P_F and higher P_D .

The second task is the tag localization: a performance metric is the position estimation error (localization error). It is given by the Euclidean distance between the estimated tag position $\hat{\mathbf{p}}$ and the true tag position as \mathbf{p} :

$$e(\mathbf{p}) = \|\hat{\mathbf{p}} - \mathbf{p}\|. \quad (3)$$

The root-mean-square error (RMSE) of position estimates is then given by

$$e_{\text{RMS}}^{\text{loc}} = \sqrt{\mathbb{E}\{e(\mathbf{p})^2\}} \quad (4)$$

where $\hat{\mathbf{p}}(i)$ and $\mathbf{p}(i)$ are the i th estimated and true position respectively and where $\mathbb{E}\{\cdot\}$ represents the statistical expectation over space and time.

The localization error outage (LEO) evaluated over the entire localization area and time is defined by:

$$\text{LEO} = P\{e(\mathbf{p}) > e_{\text{th}}\} \quad (5)$$

where e_{th} is the target (i.e., the maximum allowable) position estimation error, and the probability is evaluated over the ensemble of all possible spatial positions and time instants.

Similarly, the detection coverage is defined over the ensemble of all possible spatial positions and time instants:

$$C = P\{P_D > P_D^*\} \quad (6)$$

where we have defined P_D the detection probability in (1) and with P_D^* the desired detection probability (see Sec. 2.2.2 for typical values) whose value is application-dependent.

Finally, an additional performance parameter is the refresh rate, i.e. the rate at which a complete interrogation cycle is completed. Different parameter choices could affect this performance index. In fact, if from one side a high number of transmitted pulses per symbol and a long symbol time improves the received signal-to-noise ratio (SNR) and thus the coverage, from the other side this leads to a slowing down of the refresh rate.

We now define the performance metrics for the characterization of tracking and ordering systems.

The tracking error, at time t_n , is given by

$$e(\hat{\mathbf{p}}_n) = \|\hat{\mathbf{p}}_n - \mathbf{p}_n\| \quad (7)$$

which represents the Euclidean distance between the estimated position $\hat{\mathbf{p}}_n$ and the true position \mathbf{p}_n of a tag at time index n . Based on (7), the tracking root mean square error (RMSE), e_{RMS} , is defined as

$$e_{\text{RMS}} = \sqrt{\mathbb{E}\{e(\hat{\mathbf{p}}_n)^2\}} \quad (8)$$

The performance can be also characterized in terms of tracking error outage (TEO) which is defined as the tracking-error-based outage probability, that is given by

$$P_{\text{TEO}} = \mathbb{P}\{e(\mathbf{p}_n) > e_{\text{th}}\} = \mathbb{E}\{\mathbb{1}_{(e_{\text{th}}, +\infty)}(||\hat{\mathbf{p}}_n - \mathbf{p}_n||)\}. \quad (9)$$

In (9), $\mathbb{1}_{\mathcal{A}}(x) = 1$ when $x \in \mathcal{A}$ and 0 otherwise. The TEO can be interpreted as the probability that the localization error at a particular position exceeds the target localization error e_{th} as the agent moves along the trajectory.

When tags sorting have to be performed, as happens in the conveyor belt scenario or in similar logistic applications, a useful set of performance metrics is given by the absolute order-of-arrival (OOA) success rate R_a , the relative OOA success rate R_r , and the object detection rate R_D , and the object misdetection rate, all over N trials, respectively as

$$R_a = \frac{1}{NN_o} \sum_{n=1}^N \sum_{i=1}^{|\mathcal{D}^{(n)}|} \delta(\mathbf{o}^{(n)}[i], \hat{\mathbf{o}}^{(n)}[i]) \quad (10)$$

$$R_r = \frac{1}{NN_o} \sum_{n=1}^N \sum_{i=1}^{|\mathcal{D}^{(n)}|} \delta(\mathbf{o}_D^{(n)}[i], \hat{\mathbf{o}}^{(n)}[i]) \quad (11)$$

$$R_D = \frac{1}{N} \sum_{n=1}^N \frac{|\mathcal{D}^{(n)}|}{|\mathcal{O}^{(n)}|} \quad (12)$$

$$R_M = 1 - R_D \quad (13)$$

where we considered a stream of N_o objects with index set \mathcal{O} , and for the n th trial: $\delta(m, n)$ is the Kronecker delta function; $\mathbf{o}^{(n)}[i]$ is the i th element of the true OOA vector; $\hat{\mathbf{o}}^{(n)}[i]$ is the estimated vector; $\mathbf{o}_D^{(n)}[i]$ is the true OOA vector conditional on detection; $\mathcal{D}^{(n)}$ is the set of detected objects; and $\mathcal{O}^{(n)}$ is the set of objects.¹

On the other side, if data have to be transmitted in the UWB link to identify the tag, the related indicator is the bit error probability (BEP).

2.2.2 Specifications

In Table 2, a set of reasonable values for system performance indicators is listed with reference to the applications of interest for GRETA.

Table 1: List of requirements.

System Parameter	Target Value
LEO	$\leq 25\%$
e_{th}	$< 1 \text{ m}$
Refresh Rate	$4 - 5 \text{ Hz}$
C	$\geq 75\%$
P_D^*	$\geq 90\%$
P_F^*	$\leq 0.1\%$
BEP	$< 10^{-3}$
max operating range	5m
Operative tag consumption	$10 \mu \text{W}$
Sensor measure precision	8bits
Biodegradable mass/total mass ratio	90%

¹The $|\mathcal{A}|$ indicates the cardinality of the set \mathcal{A} .

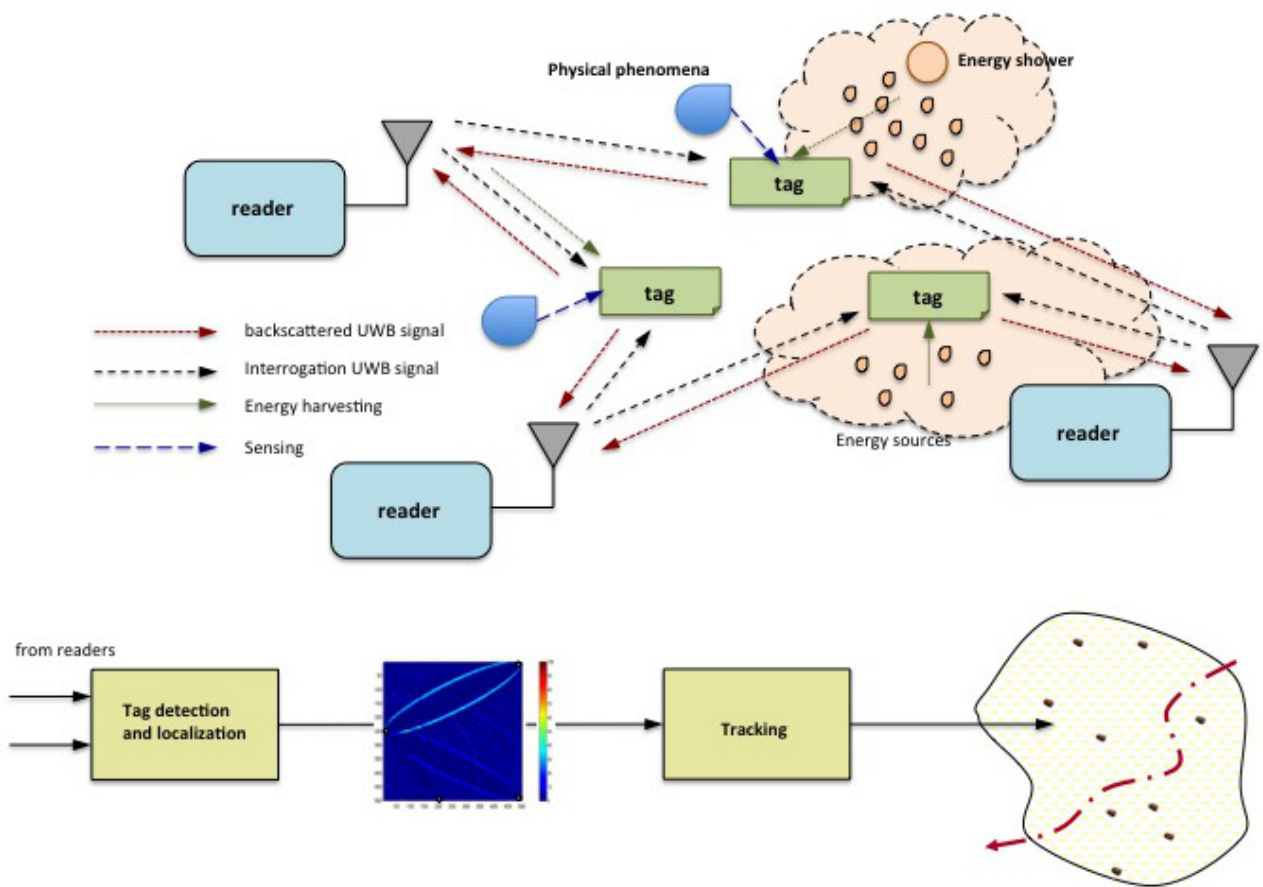


Figure 1: The proposed NG-RFID system architecture.

3 ARCHITECTURE AND TECHNOLOGIES

3.1 Introduction

The purpose of this section is the identification of the viable technologies and the general system architecture considered in GRETA according to the application requirements. Afterwards, possible tag architectures are analysed in order to understand which represents the best trade-off.

3.2 General System Architecture

This project aims at realizing a network of wireless ecological devices for identification, tracking, and monitoring of mobile entities (persons and things), as shown in Fig. 1. The intention is to employ zero-power UWB communication techniques, eco-compatible materials and energy harvesting solutions which help to store the energy from the surrounding environment. The new system herein proposed is expected to provide, among all, the trajectory of observed objects, to sense, store and share in the network the associated parameters, in a non-ambiguous fashion and for a great number of objects. This goal will be achieved through the development of systems composed of a multiplicity of readers connected in a network (Network Green RFID - NG-RFID) and capable to interrogate a great number of green tags offering sensing capabilities.

Different network configurations, depicted in Fig. 2, are of particular interest in GRETA.

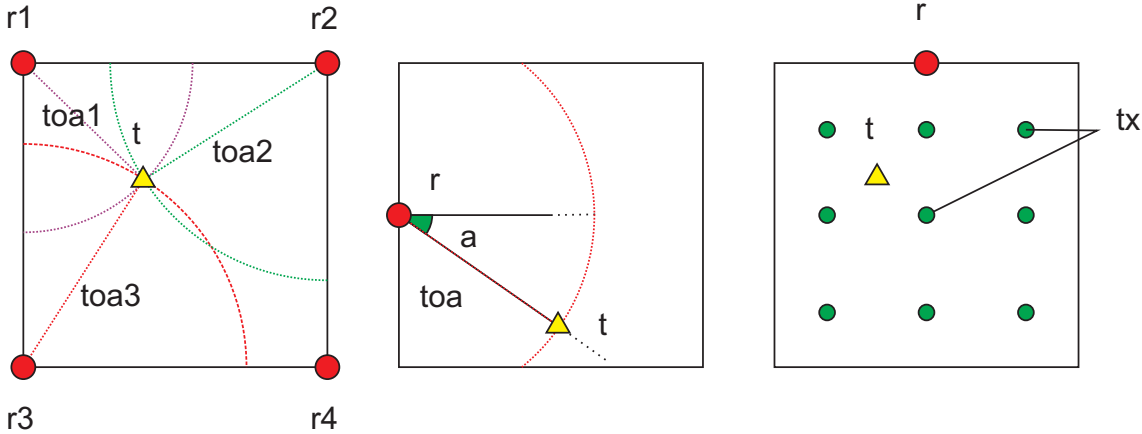


Figure 2: Reader-tag configurations of interest: monostatic configuration (left), reader array configuration (middle), multistatic with "energy shower" (right).

The first one, shown in Fig. 2-left, shows a monostatic configuration in which each reader is either equipped with a transmitting and a receiving section. After the interrogation of the tags placed in the environment, each reader collects the overall tag and environment response. Thanks to TOA measurements and a triangulation process, it is possible to localize the tag with at least three readers.

The second scenario under analysis of Fig. 2-middle, involves only one reader to infer tag's position, as a joint Direction of Arrival (DOA)-time difference-of-arrival (TDOA) estimation is performed. The unique reader is equipped with an antenna array which performs beamforming, thus reducing the number of necessary receivers and improving the link budget. The employment of antenna arrays at receiver section is an interesting opportunity, as it implies that one receiver is sufficient for localization with respect to the three needed for triangulation, by estimating the signal DOA and TOA. Moreover, arrays implies higher gains, narrow beams and beam steering capabilities opening the possibility of scanning the environment and thus improving the system coverage. It is expected, however, that this configuration will lead to higher detection time with respect to the case in which the reader's antenna presents a wider beam.

The last scenario depicted in Fig. 2-right represents an alternative solution to both the previous configurations: in fact, it represents a multistatic approach in which different transmitters (also called "energy shower") are placed at the top of the environment to reduce the receiver complexity. Such a solution has a great appeal as it offers the typical potentialities of a multistatic scenario, improving the coverage for moderate roof heights. Such showers might operate either at UHF and at UWB frequencies, according to the tag architecture chosen (see Sec. 3.4.1). A possibility is that a UWB interrogation signal is transmitted in parallel with the UHF signal used for energy harvesting or to synchronize the network. In the following sections, a deeper insight on tag architecture and reader-tag solutions is provided.

Actually, due to the very limited link-budget available, especially when passive tags are adopted and backscatter communication is exploited, further solutions can be conceived in order to enhance the performance, such as the adoption of non-Regenerative Relays, or improving the processing gain.

In fact, jointly with energy showers, the use of non-regenerative relays can improve the coverage in the presence of non-line-of-sight (NLOS) conditions [1, 2]. In this case, the adoption of relays placed in strategic positions in the monitored environment, plays the role of useful signal's repeaters enhancing the localization and identification of the tags even in the presence of harsh propagation conditions.

Another interesting possibility is the increase of the processing gain by incrementing the number of transmitted pulses per symbol [3]. Such a solution implies the coherent accumulation of several pulses at receiver side: from one hand, the received SNR is improved, but from the other hand a longer symbol time has to be accounted. Since the acquisition time is increased, the system can be more affected by detrimental effects, such as tags' clock drift and low refresh rate [4]. In the transmitted signal design, such trade-off is investigated 3.5.3.

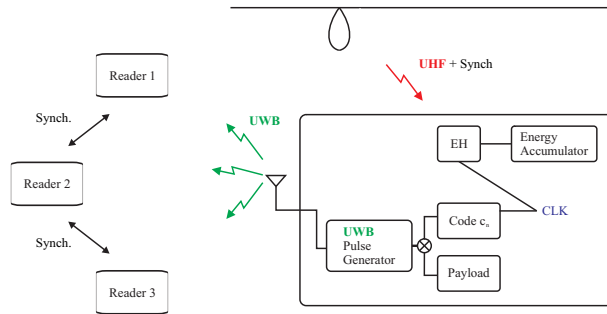


Figure 3: Active Tag.

3.3 Reader-Tag Architecture Solutions

If the UHF and UWB technologies are jointly adopted, tag design should face different issues to guarantee both UHF and UWB operation capabilities. For what the UWB section is concerned, UWB signalling represents the most natural candidate for accurate ranging through round-trip time measurement of the backscattered signal (in case of passive tags) or through precise TDOA measurement of the UWB pulse generated by the tag it self (in case of active tag). As a consequence, tags' codes generators have to be kept synchronized at pulse level for identification and ranging purposes.

To accomplish this feature, a possible solution is to exploit the UHF signal, used for energy harvesting, for synchronization at chip level (around $1\mu s$ accuracy). This solution does not need an oscillator and it results in a less energy consuming tag. Thus, the joint adoption of these two technologies seems a viable solution to overcome the limitations of UHF and UWB when are separately adopted. Moreover, it would be appreciated to have a backward compatibility with previous radio-frequency identification (RFID) technologies to open the way at numerous market-oriented applications.

In the following, we will refer to different tag architectures according to the active or passive nature of the tag (see Deliverable GRETA D1 for a classification of tags).

Active tags have an internal power source meanwhile semi-passive and passive tags must be energized and activated by an outside source, generally the reader. As a consequence, (semi-)passive devices have the capability to store energy for a short period, since they do not have the necessity to feed-up an active transmitter. Another difference between active and passive/semi-passive tags is the RF transmitting section: in fact, active tags have a complete transmitter able to generate and modulate the signal, while passive and semi-passive tags are generally based on backscattering modulation reflecting and modulating the signal generated by the reader. For these reasons and their low complexity, passive and semi-passive tags and backscatter communications are very promising, especially in the perspective of the adoption of efficient energy scavenging techniques to supply power to the control logic.

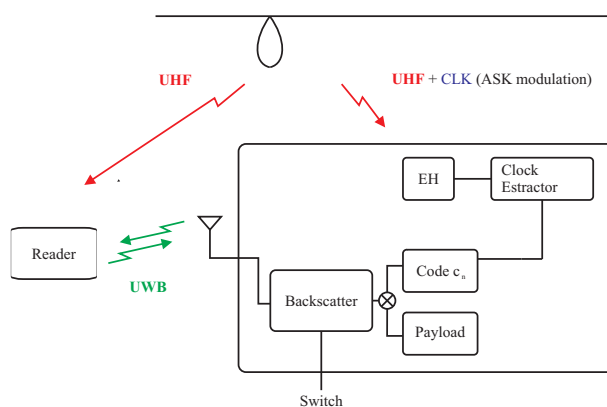


Figure 4: Stand-alone UWB-UHF passive tag.

3.4 Tag Architectures Investigated

We now describe the possible reader-tag solutions that might be adopted inside GRETA. For each solution, the advantages and the disadvantages are analysed.

3.4.0.1 Active Tags

The first tag architecture we want to analyse is the active one. As previously stated, the term active refers to the tag capability to generate an UWB signal thanks to a waveform generator included in the tag itself (refer to Fig. 3 where the active part is denoted by the UWB Pulse Generator).

If from one side, this choice translates into an improved coverage, as we have only 1-hop path in the tag-reader communication (from the active tag to the receiver), on the other side the transmitting section makes the tag particularly energy consuming and neither eco-compatible nor recyclable. In addition, another limitation of such architecture is the need of a TDOA scheme with tight synchronized readers to cope with the lack of synchronization in the UWB pulses generation process.

To resume, the advantages and disadvantages of this solution are:

- ~ improved coverage;
- ~ energy-consuming tag;
- ~ non-green tag;
- ~ synchronization among readers required for TDOA estimation.

As depicted in Fig. 3, the tag is composed of an UWB pulse generator, that modulates the signal with the coded sequence produced by the spreading unit to uniquely identify the tag, connected to an UHF antenna (in the diagram the coded sequence is described by the $\{c_n\}$ code-block and the data to be transmitted with the payload-block). On the other side, the UHF part takes advantages of the UHF showers signalling to activate the energy harvester and to extract the synchronism.

As the main idea of GRETA is to adopt energy harvesting techniques to power-up the tag, a super-cap is necessary to store enough energy to activate the transmission unit. This leads to a not easily viable solution as the time required to accumulate sufficient energy might be of several seconds as evaluated in section IV.

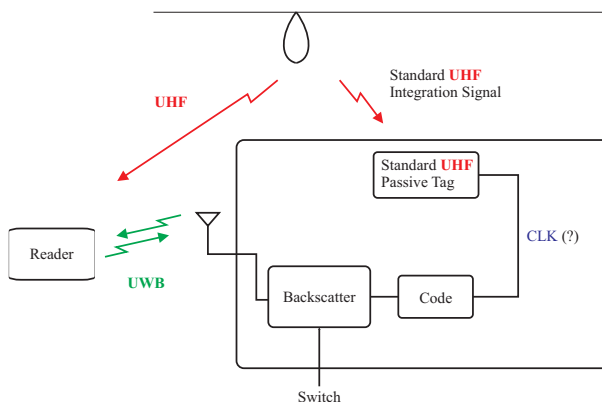


Figure 5: UWB as add-on of standard Gen.2 UHF passive tag.

3.4.0.2 Stand-alone UWB-UHF passive tag

We now analyse the possibility to adopt a stand-alone UWB-UHF passive tag (see Fig. 4). The main idea is to exploit the UWB signalling for both tags identification and data transmission, performing a precise ranging as well, while UHF energy showers are adopted for energy harvesting and system synchronization only. Additionally, the clock signal to the tag code generator can be extracted from the UHF impinging wave, guaranteeing a good synchronism.

This type of architecture has not a backward compatibility with Second Generation RFID systems but it is totally new, cheap and easy to optimize.

Tags are passive and modulate the reflected signal via backscatter modulation: several tags can be interrogated simultaneously as each of them can be characterized by a different spreading code. With this configuration, the tag architecture is simple and potentially green. In fact, the backscatter modulator performs the signal modulation of the electromagnetic waves generated by the reader (or by the "energy shower"'s oscillators) without the need of integrating the pulse generator (as done in active solutions) but just adopting an UWB switch alternating between two different load conditions [5]. As the modulator reduces to a switch, the complexity of the architecture drastically decreases .

However, to detect several tags at the same time, the reader should have multiple de-spreading units (one for each tag's coded sequences) increasing its complexity and cost at infrastructure level.

The tag's UHF section consists of an energy harvester to activate the tag itself and it provides the clock (thus avoiding the local oscillator in the tag and clock drift problems). In principle, more than one reader could interrogate the same tag simultaneously (using different coded signals), however the inter-reader interference could be detrimental.

Another limitation of this solution is the poor link budget due to the two-hop communication link between readers and tags. Even if several solutions might be adopted to counteract such issue, this effect can dramatically reduce the overall system performance.

As already mentioned this approach does not guarantee backward compatibility, since UHF is only used for energy harvesting (EH) and to provide the clock synchronism but it is non standard-compliant.

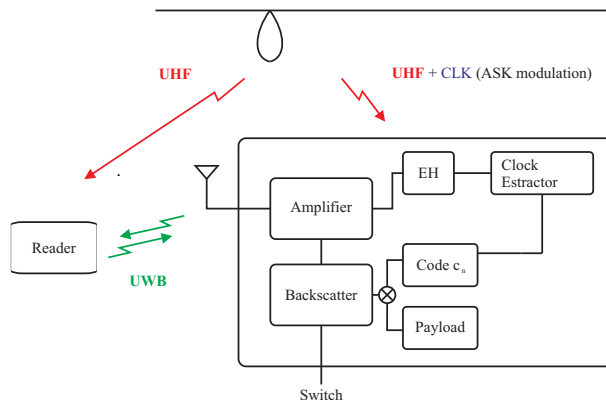


Figure 6: Tag operating as an active reflector.

To sum up, the positive and negative aspects of this architecture are here listed:

- ~ low complexity and green tag architecture;
- ~ good synchronism via UHF signalling;
- ~ no backward compatibility;
- ~ poor link budget;
- ~ high complexity and cost of readers architecture.

3.4.0.3 UWB as add-on of standard Gen.2 UHF passive tag

The solution herein proposed aims to integrate UWB tag as add on of a standard Gen.2 UHF tag (see Fig. 5): Backward compatibility opens a wider range of potential applications in current industrial markets. The UWB link is used only for high-accuracy ranging, while the standard Gen.2 protocol is adopted to read and write data from/to the tag. One of the problems to be faced while adopting this approach is an easy integration of the UWB and sensor part with the standard UHF chip.

Among the possible benefits of such a solution, it is important to remark that multiple access is solved by the Gen. 2 UHF protocol: since only one tag per time is allowed to communicate with the reader, there is not multi user interference problem in the UWB link. In addition, the communication is

faster as no data are transmitted in the slow UWB communication link, and only 1-2 UWB symbols and 1 unique spreading code are necessary for ranging (1-2 ms interrogation duration). As a consequence, a simple reader is required to perform tag detection and localization, guaranteeing also high refresh rate (the standard guarantees about 200 reads/s). For more details see Sec. 3.5.3.

The benefits and the drawbacks of this solution are:

- ↪ low complexity and "green" tag architecture;
- ↪ low complexity of reader architecture;
- ↪ backward compatibility with current UHF RFID, which is appealing for industrial applications;
- ↪ high refresh rate;
- ↪ market-oriented;
- ↪ feasibility of an easy integration of the UWB and sensor part with the standard UHF chip to be investigated.

3.4.0.4 Tags as Active Reflectors

The last solution we propose is the adoption of the tag as an active reflector (see Fig. 6). It is a modification of the stand-alone joint UWB-UHF solution in which an UWB power amplifier is added in the architecture to strengthen the backscatter signal and improve the link budget.

As before, the UHF signal transmitted by the shower is exploited by both readers and tags to perform synchronization, and it is also used as clock signal at tag side and for energy harvesting as well. Such a solution implies an improved coverage and a precise UWB synchronization, but the amount of energy to be stored to power up the UWB amplifier and how to harvest it is still a point under investigation. Again, the main drawback of this solution is a less green solution leading this approach far from the project objectives.

Some benefits and drawbacks are here reported:

- ↪ improved coverage;
- ↪ precise synchronism;
- ↪ no backward compatibility;
- ↪ reduced greenness of tag architecture;
- ↪ high complexity and cost of readers architecture.

3.4.1 Reader-Tag Architectures Suitable for the Project

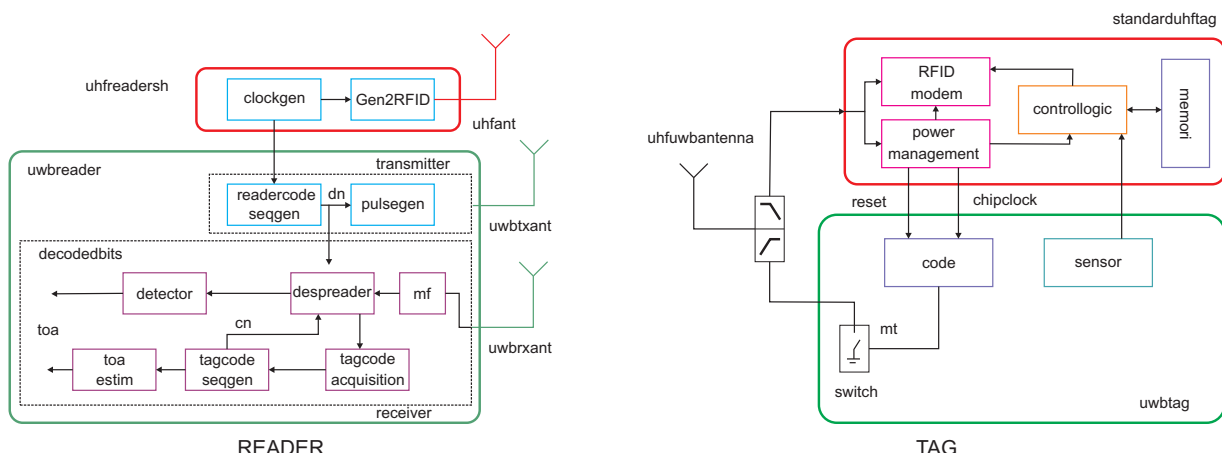


Figure 7: UWB as an add-on of standard Gen.2 UHF reader-tag - Block Diagram.

Considering all the features of the proposed solutions, the two main candidates for the final reader-tag green architecture are the adoption of UWB as an add-on of standard UHF RFID and the stand-alone UWB solution. In Fig. 7 and 8 we report the reader's and tag's structure for each solution.

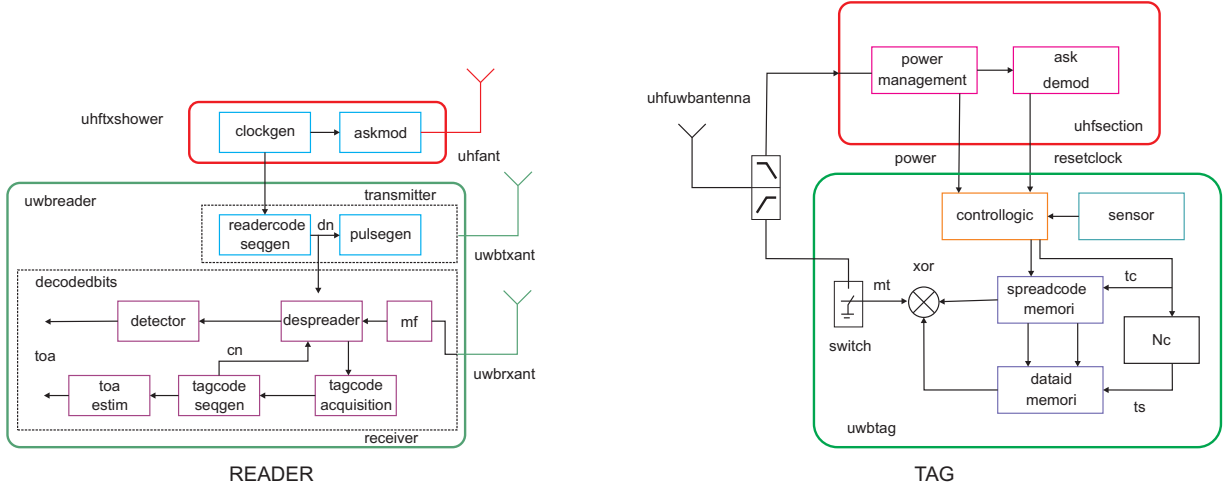


Figure 8: Stand-Alone UWB-UHF reader-tag - Block Diagram.

The main difference between the two architectures is the backward compatibility with the standard Gen.2 RFID technology and reader complexity. In fact, consider the UHF section: the joint UWB-UHF stand-alone solution is mainly composed of an amplitude shift keying (ASK) modulator (see Fig. 8), while in Fig. 7, the UHF section reduces to a Gen.2 RFID reader guaranteeing the backward compatibility with the UHF standard. With reference to the block scheme, the UWB transmitter section is composed of a UWB pulse generator and of a spreading sequence (reader's code) generator that produces an antipodal binary sequence $\{d_n\}$ of length N_c symbols (chips). Each chip modulates in amplitude the transmitted pulses (PAM modulator) as will be better illustrated in the Sec. 3.5. The generated signal is sent to the antenna connector and radiated in air.

The compatible Gen.2 UWB-UHF reader of Fig. 7 interacts with a tag whose control logic and memory functions are accomplished by the UHF standard while the UWB section drastically simplifies, as it is exploited only for ranging. As a consequence, it becomes an appealing solution for current industrial applications: the state of the art of UHF RFID systems can be simply equipped with a UWB section (mainly composed of a UWB switch for backscatter modulation, and a sensor) that performs high ranging capabilities while maintaining the compatibility with UHF RFID standard.

Consider now the joint UWB-UHF stand-alone system of Fig. 8. It requires a more complex reader and tag's UWB section but with a lower power consumption and a newer structure with respect to the traditional UHF tag, as it is completely based on UWB backscatter communication.

Figure 9 reports an equivalent scheme of the UWB reader-tag backscatter communication: pulses radiated by the reader according to the sequence $\{d_n\}$, are received by the tag and multiplied by the code $\{c_n\}$ and the data. Successively they are backscattered and received by the reader. A de-spreading stage realizes the product of the received signal and the composite sequence given by the reader and tag code, and a decision stage demodulates the data bit sent by the tag [6–8], where it is evident how the tag modulates the reflected signal according to the information data b_n and the reader's and tag's code.

3.5 Signal Format

This section aims at providing the communication protocol to be adopted. The signal format is strictly related to the two tag architectures which seems to be the most promising ones for the project, that is the *stand-alone UHF-UWB tag* and to the *UWB as add-on of standard Gen.2 UHF tag*.

3.5.1 Stand-Alone UWB-UHF Tag Communication Scheme

In Fig. 10 the communication between a reader and a stand alone UWB tag is shown, where the UHF link is exploited for energy harvesting and system synchronization, while the UWB link is adopted for

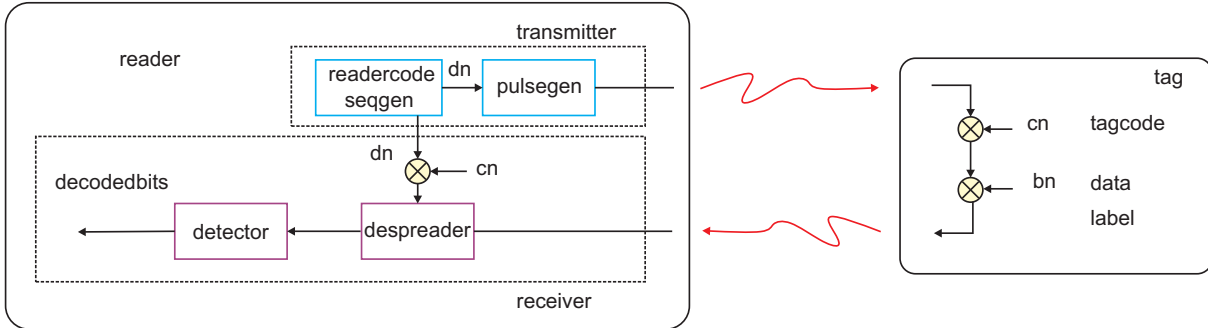


Figure 9: Equivalent Scheme for the Backscatter Link.

tags identification, data transmission and ranging. Note that in this case, the scenario is monostatic, as the reader plays both the transmitting and receiving role.

A multistatic alternative, depicted in Fig. 11, considers the adoption of distributed energy showers consisting of different transmitters. In this alternative version, the UHF and UWB interrogation signals could be generated by energy showers deployed in the environment to facilitate the coverage and the energy harvesting procedure, while the tags' backscattered signals are collected by the UWB readers. The main issue of this architecture could be how to synchronize multiple showers, which is far from being trivial, and the real advantages of adopting a multistatic scenario, which are analysed in the following.

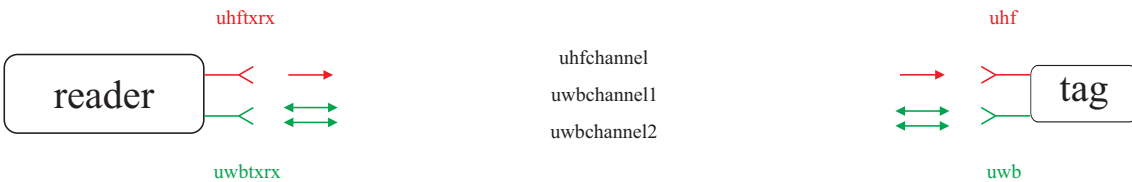


Figure 10: Reader and stand-alone UWB tag

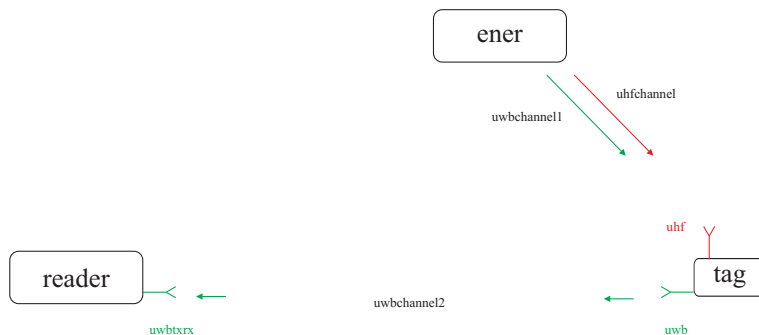


Figure 11: Reader and stand-alone UWB tag with energy shower

For the stand alone architecture the interrogation cycle is shown in Fig. 12. Reader-tag communication takes place during an interrogation of duration cycle T_{cycle} involving different steps: first of all, the reader interacts with the tag via a UHF wake-up signal in order to power up the tag and activate the UWB switching control responsible of antenna load variations (wake-up period of duration $T_{\text{wake-up}}$). Once the tag has been powered up and the synchronization process has ended (after a fixed time T_{synch}), a sequence of UWB pulses (of duration T_{int}) is transmitted by the reader to interrogate the tag and obtain the data stored on them.

The reader modulates the UWB transmitted sequence using an antipodal binary code of period T_s and length N_c given by $\{d_n\} \in \{-1, +1\}$, which allows to uniquely identify the reader (reader's code).

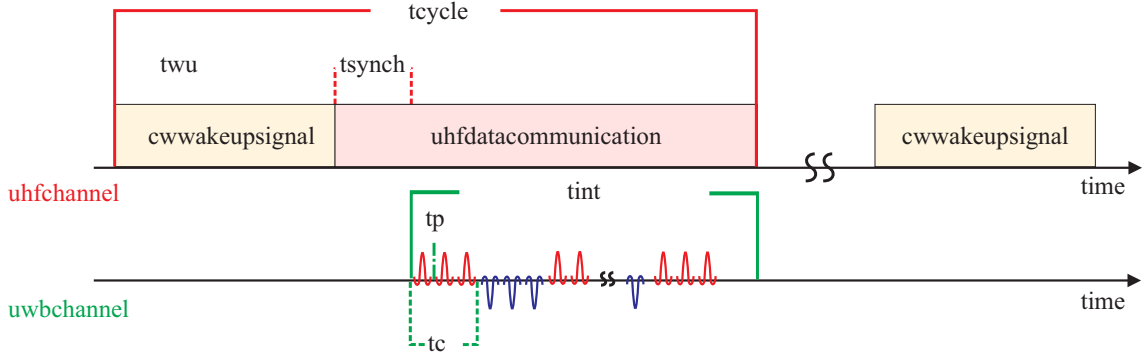


Figure 12: Interrogation cycle Stand-Alone Tag.

Each transmitted pulse is backscattered by all tags as well as by all the surrounding scatterers present in the environment determining, at reader side, the clutter component. In particular, at each chip time T_c , the k th tag changes its load conditions (short or open circuit) in order to modulate the backscattered signal, according to an antipodal tag's code $\{c_n^{(k)}\} \in \{-1, +1\}$ of period N_c . The backscattered signal associated with this tag is so modulated by $\{d_n c_n^{(k)}\}$. On the other hand, all the signals coming from other interfering tags are modulated by different tags' codes $\{d_n c_n^{(i)}\}$ with $i \neq k$. Differently, the environmental reflected signals (i.e., the clutter component, which includes the structural antenna mode) exhibits modulation by the reader's code $\{d_n\}$ only. Then, to discriminate the useful component (i.e. that reflected back by the k th tag) it is sufficient at reader side to perform a de-spread of the received signal using the $\{d_n c_n^{(k)}\}$ coded sequence.

The tag UWB interface is adopted also for data transmission, then the tag information symbol $\{b_n\}$ is associated to each burst of N_s pulses with symbol time $T_s = T_p N_s$, and it affects the entire sequence of pulse polarity at each symbol time. In general we consider only one active reader at each time according to a reader time division multiple access (TDMA) protocol to minimize the inter-reader interference.

3.5.2 UWB as Add-On of Standard Gen.2 UHF Tag Communication Scheme

Consider now the UWB section as an add-on for the standard Gen2 UHF RFID. Figure 13 shows the

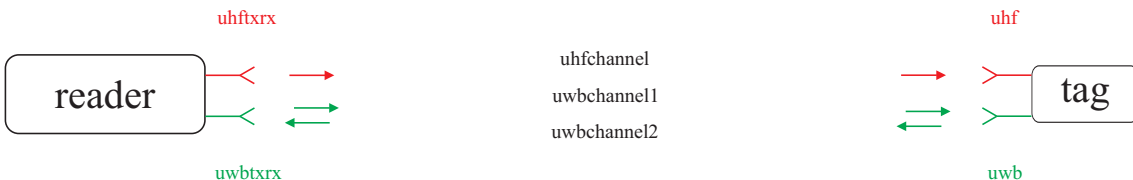


Figure 13: Reader and backward Gen2 UHF-UWB tag

communication scheme reader-tag, where the UWB part is exploited only for ranging purposes, while with the UHF link, data are read from the tag. As shown in Fig. 14, the reader-tag communication takes place during a period T_{cycle} as before: the UHF channel is dedicated to synchronization and data communication while relegating the UWB channel for ranging transmission. The UWB transmitted sequence is identical to the previous case with the only exception that is not modulated according to the sensor's data but only by the spreading code for localization purposes. Therefore only a limited number of symbols is sufficient for ranging purposes.

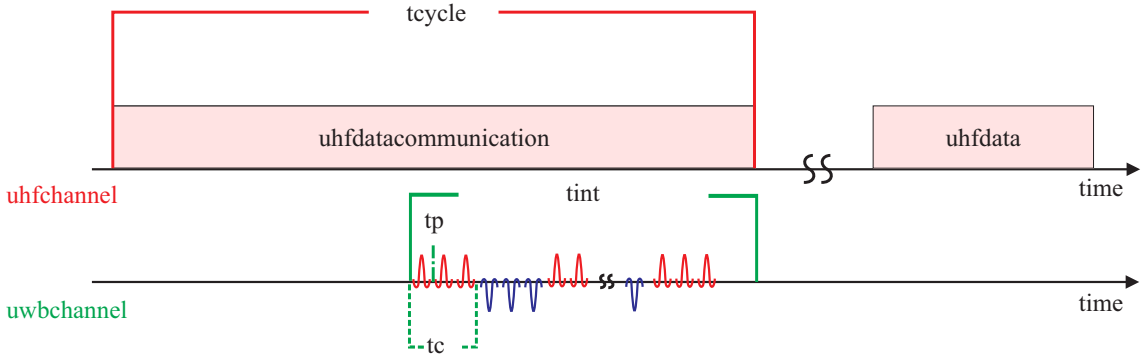


Figure 14: Interrogation cycle backward Gen.2 UWB-UWB tag.

3.5.3 Interrogation signal

The impulse radio UWB (IR-UWB) technique relies on ultra-short (nanosecond scale) pulses that can be free of sine-wave carriers and do not require intermediate frequency processing because they can operate at baseband, thus drastically reducing the hardware complexity and power consumption [9].

As said, in IR-UWB the information is encoded using pulses. Typically the adopted pulse $p(t)$ is derived by the baseband Gaussian pulse $p_0(t) = \exp(-2\pi(t^2/\tau_p^2))$ and its derivatives due to its smallest possible time-bandwidth product which maximizes range-rate resolution and are readily available from antenna pattern. Alternatively, the IEEE 802.15.4a standard suggests the following band-pass pulse with center frequency f_c and root raised cosine (RRC) envelope

$$p(t) = \frac{4\sqrt{2}}{\pi\sqrt{\tau_p}} \frac{\cos((1+\nu)\pi t/\tau_p) + \frac{\sin((1-\nu)\pi t/\tau_p)}{4\nu t/\tau_p}}{1 - (4\nu t/\tau_p)^2} \cos(2\pi f_c t) \quad (14)$$

where parameter τ_p and roll-off factor ν determine the bandwidth $B_W = (1+\nu)/\tau_p$.²

To allow for multi-user communication in a typical IR-UWB communication system, each symbol (bit) is associated to multiple pulses.

In direct-sequence spread-spectrum (DS-SS) schemes, each pulse is modulated according to a pseudo-random binary code $\{c_n\}$ having period N_s and transmitted at regular intervals of T_c seconds usually named, in this case, chips.

The frame (chip) time T_c is usually chosen to be greater than the maximum multipath delay to avoid inter-symbol interference. The information can be associated to pulse polarity leading to pulse amplitude modulation (PAM) signaling or to pulse position thus obtaining a pulse position modulation (PPM) signaling scheme.

As seen before, during T_{cycle} , the reader transmits a sequence of UWB pulses modulated by a periodic binary spreading sequence $\{d_n\}$ of period N_c with $d_n \in \{-1, 1\}$, specific to that particular reader (reader's code). In general, N_{pc} pulses are associated to each code symbol (chip). To accommodate the signals backscattered by tags corresponding to an entire packet of N_t bits, the UWB interrogation contains $N_t = N_r N_s$ pulses, where $N_s = N_c N_{pc}$ is the number of pulses associated to each bit. Pulses are separated by T_p seconds. Then the UWB transmitted signal takes the form

$$s_{\text{reader}}^{\text{UWB}}(t) = \sum_{k=0}^{N_r-1} s(t - kN_c T_c) \quad (15)$$

where $T_c = N_{pc} T_p$ is the chip time and $s(t)$ is the composite sequence given by

$$s(t) = \sum_{n=0}^{N_c-1} d_n g(t - nT_c) \quad (16)$$

²Two different values of τ_p are recommended [9]: $\tau_p = 1$ ns and $\tau_p = 3.2$ ns with $\nu = 0.6$, corresponding to two different bandwidths, $W = 1.6$ GHz and $W = 500$ MHz, respectively.

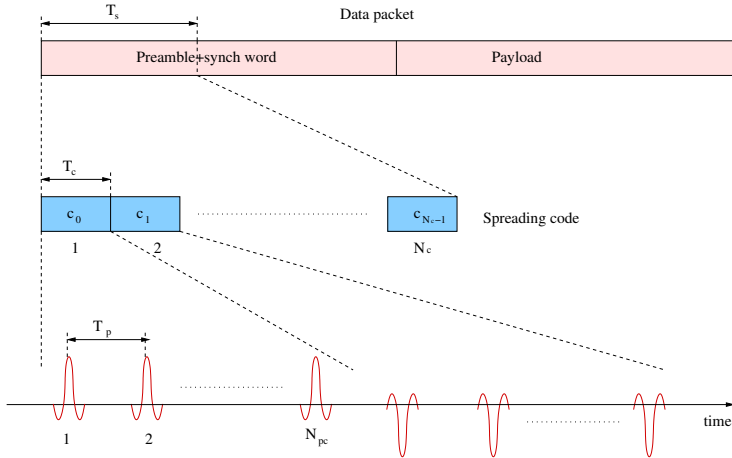


Figure 15: Example of backscattered signal structure, where only the useful component is reported, and $\{d_n\}$ is a sequence of all +1s for simplicity.

with

$$g(t) = \sum_{i=0}^{N_{pc}-1} p(t - iT_p) \quad (17)$$

being the waveform associated to each chip $\{d_n\}$ composed of N_{pc} elementary UWB pulses $p(t)$. The pulse repetition period T_p is chosen so that all signals backscattered by the environment are received by the reader before the transmission of the successive pulse. In indoor scenario $T_p = 100\text{ ns}$ is usually sufficient to this purpose. The transmitted signal in (15) is the same either adopting the stand-alone UWB tag architecture or the backward Gen.2 UHF-UWB one.

The UHF transmitted signal for the UWB-UHF stand-alone tag architecture, is given by

$$s_{\text{reader}}^{\text{UHF}}(t) = \text{rect}\left(\frac{t + \frac{T_{\text{wake-up}}}{2}}{T_{\text{wake-up}}}\right) \cos(2\pi f_w t) + \sum_{n=0}^{N_c-1} \omega_n \text{rect}\left(\frac{t - (n + \frac{1}{2})T_c}{T_c}\right) \cos(2\pi f_w t) \quad (18)$$

where the first term represents the wake-up signal of duration $T_{\text{wake-up}}$ (see Fig. 16) while the second term is the ASK signal (see Fig. 17) in which $\omega_n = 1$ for even n value while $\omega_n = a$ for odd n value ($0 < a < 1$), $N_{\text{wake-up}} = \lfloor \frac{T_{\text{wake-up}}}{T_c} \rfloor$ and f_w is the UHF center frequency. The ASK modulated UHF signal is exploited in the tag to extract the chip-level synchronization signal used to drive the UWB switch in the backscatter modulator.

The UHF transmitted signal for the UWB-UHF Gen 2 tag architecture is regulated by the standard. For more details of reader-tag communication in Second Generation RFID refer to [10].

Generally, if a UWB-UHF stand-alone tag is adopted, a very limited link-budget is available (see Table. 2 and Sec. 4.1 for more details) and to improve the coverage, a large number of pulses per symbol (N_s) is necessary. In Table. 2 an example of link budget in additive white Gaussian noise (AWGN) is given. The transmitting power P_t has been chosen compliant to the Federal Communications Commission (FCC) emission limit in the 3.1 – 4.8 GHz band. Fixing $N_s = 8192$ (corresponding to a processing gain PG = 40 dB) and with a SNR threshold of 15 dB, the maximum distance to correctly detect a passive tag is 3.20 m.

An example of a set of the principal parameters for the two architectures is given in Tab. 3 and Tab. 4. Increasing N_s leads to a symbol time of some ms, consequently the packet transmission time could be very large (> 100 ms) limiting the refresh rate. On the contrary if a UWB-UHF tag compliant with the Gen.2 UHF tag is chosen, there are no constraints for the number of pulses per symbol resulting in a more robust link budget due to a higher processing gain. Moreover, while in the first architecture multiple tags with different codes can be read simultaneously (with parallel receivers), with the second alternative system

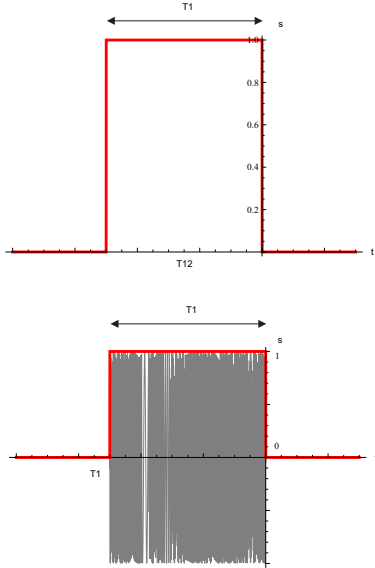
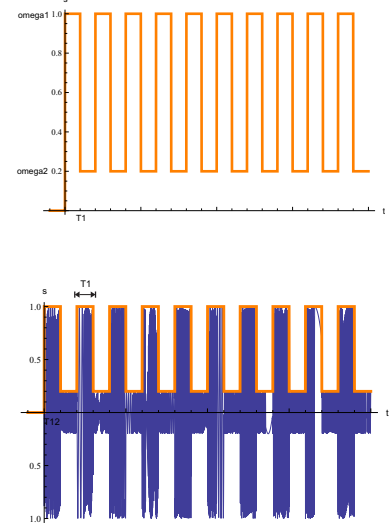


Figure 16: UHF wake-up signal.

Figure 17: UHF synchronization signal (with $a = 0.2$).

only one tag per time is active and a unique spreading code is necessary for ranging thus simplifying the reader structure.

3.5.4 Tag Timing

Each pulse in (17) is backscattered by the tag's antenna as well as by all the surrounding scatterers present in the environment which form the clutter component.

The main task of the receiver section of the reader is to detect the useful backscattered signal (i.e., the tag's antenna mode scattering which depends on antenna load changes) from interference and clutter, given by other scatterers' reflections and the structural mode contributions, which is, in general, dominant.

To make the uplink communication robust to the presence of clutter, interference, and to allow multiple access, a proper backscatter modulation strategy is necessary at tag side. In Sec. 3.5.5, tag code design strategies will be described in order to accomplish such issues.

When switched on, the tag changes continuously its reflection property according to the sign of code symbols (every T_c seconds) and data symbols (every $T_s = T_c \cdot N_c$ seconds being T_s the symbol time).

The UWB switch is controlled by a micro-controller whose purpose is to change the switch status X (short or open circuit) at each chip time T_c according to the data to be transmitted and a zero mean (balanced) periodic tag's code $\{c_n\}$, with $c_n \in \{-1, +1\}$, of period N_c , in order to perform clutter removal, as will be detailed in the following. Specifically, each stand-alone UWB tag information bit $b_k \in \{-1, +1\}$ is associated to N_s pulses³ while in the case of backward Gen.2 UWB-UHF tag the information bit is associated to the UHF packet. In both cases the symbol time results $T_s = T_c N_c = T_p N_s$. Therefore, the backscatter modulator signal, commanding the tag's switch, can be expressed as

$$m(t) = \sum_{k=0}^{N_r-1} b_k \sum_{n=0}^{N_c-1} c_n \Pi \left(\frac{1}{T_c} (t - nT_s - iT_c - \Delta) \right) \quad (19)$$

if the UWB-UHF stand-alone architecture has been chosen or as:

$$m(t) = \sum_{k=0}^{N_r-1} \sum_{n=0}^{N_c-1} c_n \Pi \left(\frac{1}{T_c} (t - nT_s - iT_c - \Delta) \right) \quad (20)$$

³In this way the polarity of the reflected signal changes according to the tag's code during a symbol time, whereas the information symbol affects the polarity of all pulses composing the sequence each symbol time.

Table 2: Link Budget Table.

Symbol	Value & Units	
f_c	UWB central frequency	4GHz
f_w	UHF central frequency	900MHz
c	Speed of Light	$3 \cdot 10^8$ m/s
τ_p	Pulse Width	1 ns
v	Roll-Off factor	0.6
B_W	Bandwidth	$B_W = (1 + v)/\tau_p$
P_t	Transmitted Power	$P_t = \langle p(t) ^2 \rangle / R = \frac{1}{T_p R} \int p(t) ^2 dt$
R	Adaptation impedance	50 Ohm
T_p	Inter-Pulse time	128 ns
G_{reader}	Reader Antenna Maximum Gain	3 dBi
G_{tag}	Tag Antenna Maximum Gain	0 dBi
F	Noise Figure	4 dB
T_0	Reference Temperature	290 K
k_{boltz}	Boltzmann Constant	$1.38 \cdot 10^{-23}$ J K $^{-1}$
SNR_{\min}	SNR threshold	15 dB
N_s	Number of Pulses per Symbol	12800
L_p	Tag Loss	4 dB
M	Supplementary Loss	6 dB
d_0	reference distance	1 m
E_t	Transmitted Energy	$E_t = P_t T_p$
EIRP	Effective Isotropically Radiated Power	$\text{EIRP} = P_t + G_{\text{reader}}$
T_{sist}	System Temperature	$T_{\text{sist}} = F T_0$
N_0	Noise Power Spectral Density	$N_0 = T_{\text{sist}} k_{\text{boltz}}$
PG	Processing Gain	$\text{PG} = 10 \log(N_s)$
PL_{\max}	PL threshold	$PL_{\max}(\text{dB}) = 10 \log\left(\frac{E_t}{N_0}\right) + \text{PG} - \text{SNR}_{\min}$
PL_0	path-loss (PL) at d_0	$PL_0(\text{dB}) = 10 \log\left(\frac{4\pi d_0 f_c}{c}\right)$
d_{\max}	Maximum Distance	$d_{\max} = \sqrt[4]{d_0^4 \frac{PL_{\max}^2 \cdot G_{\text{reader}}^2 \cdot G_{\text{tag}}^2}{PL_0^2 \cdot L_p \cdot M}}$

for the backward Gen.2 UHF-UWB architecture, with $\Pi(t) \triangleq 1$ for $t \in [0, 1]$ and zero otherwise. Note that in general reader and tag have their own independent clock sources and hence they have to be treated as asynchronous. Then the tag's code $\{c_n\}$ is not in general time aligned to the reader's code $\{d_n\}$. The parameter Δ in (20) denotes the clock offset of the tag with respect to the reader's clock.

The receiver scheme performs a de-spreading operation using the combined code $\{c_n \cdot d_n\}$, which identifies both the reader and the desired tag.⁴

3.5.5 Tags Codes Design

According to the tag architecture adopted in GRETA, we now describe possible tag codes solution that have to be accounted when codes are assigned to tags.

⁴Multiple readers can access the same tag by using different reader codes provided that they are designed with good cross-correlation properties.

Table 3: Signal Parameters Choice for Stand-Alone Passive UWB Tag.

Parameter Symbol	Parameter Description	Value	Units
T_p	Inter-pulse time (\geq maximum round-trip time (RTT))	100	ns
$T_c = N_{pc} T_p$	Chip Time	10	μ s
$B_c = 1/T_c$	Chip Rate	0.1	MHz
$T_s = N_c T_c = N_s T_p$	Symbol (bit) Time	1280	μ s
$B_r = 1/T_s$	Bit Rate	0.78125	Kbit/s
N_{pc}	number of pulses per chip	100	-
N_c	spreading code length (number of chips)	128	-
N_s	Processing Gain: Number of emitted pulses per symbol (bit)	12800	-
N_r	Number of bits per packet	150	-
$T_{int} = N_r T_s$	Packet Duration	192	ms
$T_{wake-up}$	maximum time required to switch the tag on	5	ms
T_{synch}	synchronization time	10	μ s
T_{cycle}	interrogation cycle time	-	-
$R_{refresh} = 1/T_{cycle}$	refresh rate ($\leq 1/(T_{int} + T_{wake-up} + T_{synch})$)	5,076	Hz

Table 4: Signal Parameters Choice for backward Gen.2 UHF passive Tag.

Parameter Symbol	Parameter Description	Value	Units
T_p	Inter-pulse time (\geq maximum RTT)	100	ns
$T_c = N_{pc} T_p$	Chip Time	10	μ s
$B_c = 1/T_c$	Chip Rate	0.1	MHz
$T_s = N_c T_c = N_s T_p$	Symbol (bit) Time	1280	μ s
N_{pc}	number of pulses per chip	100	-
N_c	spreading code length (number of chips)	128	-
N_s	Processing Gain: Number of emitted pulses per symbol (bit)	12800	-
N_r	Number of bits per packet	2	-
$T_{int} = N_r T_s$	Packet Duration	2.56	ms
$R_{refresh}$	Gen 2 max refresh rate	up to 200	Hz

3.5.5.1 Stand-Alone UWB-UHF Tag

In stand-alone UWB tags, the design of the spreading code is particularly critical in order to allow multiple access, clutter removal, and robustness to system non-idealities. In fact, the requirements that spreading codes have to fulfill are:

- number of available coded sequences;
- clutter removal capability;
- robustness to wake-up offset;
- multi-user interference mitigation.

The code family chosen has to account for a large number of available sequences if a large number of tags has to be managed, unless the same codewords are re-used.

For what clutter removal capability is concerned, in [7] it has been shown that it can be achieved by

adopting balanced codes (i.e., codes with the same number of +1 and -1 in each codeword).

Tags are simultaneously woken-up after an initial wake-up process which might introduce a time offset (in the order of T_c) causing code shifts of a few chips. Codes orthogonality (or very small peak cross correlation) even in the presence of small shifts, becomes a requirement for the good functioning of the system. For example, zero correlation zone codes [11] allow to extend the orthogonality among codewords for a certain number Z of shifts. Another simple approach is to consider codes with shorter effective length $N_{ce} = N_c / \kappa$, with $\kappa = 2, 3, \dots$, and extend it by a factor κ through simple chip duplication. The benefit of this solution is an enhancement of system robustness to codes shifts while the drawbacks are a lower number of codewords, a potential lower interference mitigation properties, and a lower clutter rejection if an odd code is adopted.

To what concerns the behaviour of codes in synchronous and asynchronous scenario some considerations have to be done. Firstly, consider a synchronous scenario: Orthogonal codes, such as Walsh Hadamard, offer perfect interference removal and perform better than Gold and Kasami pseudo-noise (PN) codes which are not balanced. On the contrary, in asynchronous scenario, orthogonal codes present unsatisfactory cross-correlation properties [12] while Gold and Kasami PN codes are good candidates.

An interesting possibility for the UWB RFID backscatter modulation system is to adopt orthogonal Gold codes [13]. These codes are exactly orthogonal in the synchronous scenario, as they are phase-aligned to assure orthogonality, and maintains the properties of extended Gold Codes (low cross-correlation) in asynchronous scenario. They are constructed by the lengthening of one chip preferentially-phased Gold codes [14], where a code phase optimization process is performed in order to assure proper cross-correlation properties [13]. Therefore, an even code is obtained, which enables the complete clutter cancellation and good interference rejection for various scenarios. The adoption of this codes typology provides the opportunity to reduce the complexity and robustness of the synchronization process by increasing κ even in presence of wake-up synchronization offset and drift.

Summarizing all the previous considerations, we have:

- The tag's code c_n must have zero mean (equal number of +1 and -1) to remove the clutter during the de-spreading operation;
- The tag's code c_n can belong to an *orthogonal codes* set (e.g., Hadamard) if tags codes' generators are synchronous. Up to N_c codewords (simultaneously detectable tags) are in this case available.
- The tag's code c_n must belong to *PN-like code sets* (e.g., Gold, m-sequences) if tags are not synchronized through a wake-up signal. Usually $N \ll N_c$ codewords (simultaneously detectable tags) are available, then very long codes are needed to support a large number of tags;
- Orthogonal Gold codes can perform well both in synchronous and in asynchronous (or quasi-synchronous) scenario. $N = N_c/2$ codewords are available .

3.5.5.2 UWB as Add-On of Standard Gen.2 UHF Tag

In this scenario, tags code assignment is very simple, as the multiple channel access is resolved by the Gen.2 UHF RFID protocol, and the UWB communication is performed in parallel with the UHF link.

To mitigate the clutter effects only one balanced codeword is needed, but no requirements for what synchronous and asynchronous scenario are concerned.

3.5.5.3 Example of codes performance

A first analysis that has been conducted shows the bit error rate (BER) as a function of the number of transmitted pulses N_s in a scenario in which 59 interfering stand-alone UWB tags are uniformly distributed in 1 m around the useful tag that is at 7 m from the receiver. Due to the passive nature of the tag, a two-hop link between the considered tag and the reader has been taken into account and then, a double convolution of the transmitting pulse with the channel impulse response has been performed. Fixing $T_p = 128$ ns and $N_c = 1024$, the channel responses have been obtained by Monte-Carlo simulations, starting from channel responses drawn from the 802.15.4a CM1 channel model [15].

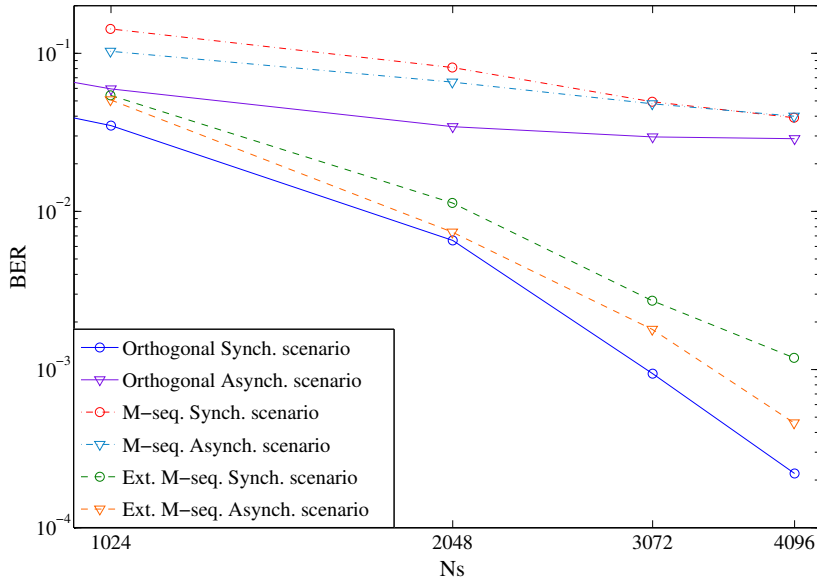


Figure 18: BER vs N_s in multipath 802.15.4a CM1 channel.

The reader is characterized by an antenna gain of 5 dBi.

For what the clutter is concerned, a uniform power delay profile in the overall interval T_p has been taken into account, with paths spaced apart of 0.95 ns, each path's amplitude characterized by Nakagami- m fading, with $m=3$, and a root-mean-squared value of 0.5 mV at the receiver.

In Fig. 18 results for different choices of spreading codes and different synchronization conditions, are depicted. In a quasi-synchronous scenario, where tags' and reader's code generators are synchronized, and the time-of-arrival of the interference components depends only on tags' position, the performance of zero-mean orthogonal Hadamard codes results to be not affected by multi-user interference (MUI) and clutter.

On the contrary, when reader and tags are asynchronous, the performance of the system when using orthogonal codes drastically degrades due to the joint effect of multipath and poor cross-correlation properties of the codes (MUI). For what the m -sequences are concerned, as can be noticed in Fig. 18, significant performance degradation is obtained in the presence of strong clutter since sequences are not balanced. On the other hand, the choice of zero mean codes (extended m -sequences) still confirms to be a good solution to avoid clutter effects at the expense of a slight performance loss due to degraded cross-correlation properties.

In the following, as the de-spreading circuits must be replicated for each of the multiple tags existing in the system in order to perform a simultaneous detection, we will consider a low-complexity energy detector-based receiver architecture.

In order to investigate code properties, we now analyse the tag detection rate as a function of the false alarm rate. A total number of pulses per symbol $N_s = 8192$ is chosen,⁵ in order to counteract the poor link budget, with $T_c = 1.024 \mu s$ and $T_p = 128 \text{ ns}$ (i.e., $N_{pc} = 8$). A reader with 5 dBi antenna gain, a tag considered in the maximum reader's antenna direction equipped with an 1 dBi antenna and 2 dB switch losses have been considered.

Results have been obtained by Monte-Carlo simulations, starting from multipath channel responses with exponential power delay profile and Nakagami- m fading (severity factor $m=3$), a root-mean-squared channel delay-spread of 10 ns⁶ and paths separated of 2 ns apart. A transmitted signal compliant with the

⁵This value derives from the number of pulses necessary to achieve a certain SNR per bit given the maximum reader-tag reading range (link budget constraint).

⁶This value is comprehensive of the two-way link of the backscatter signal.

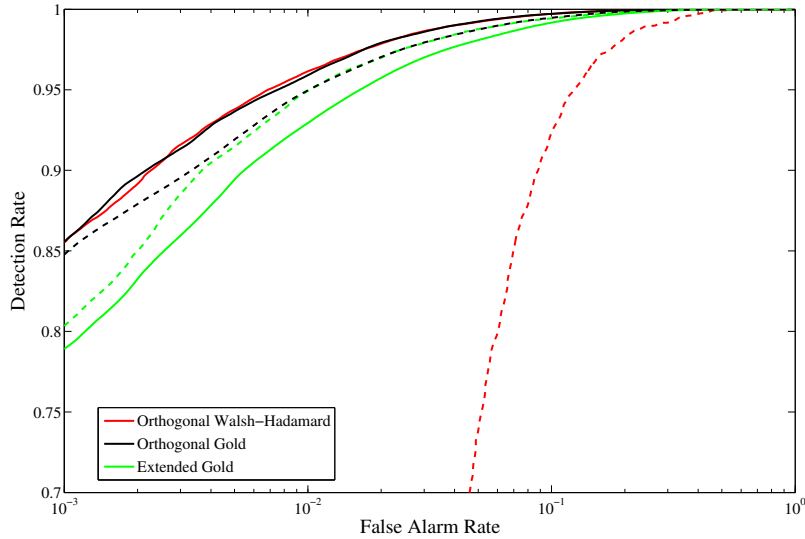


Figure 19: ROC for the tag detection in UWB backscatter system. Continuous lines (—) refer to the perfectly synchronous scenario, dashed lines (--) refer to the asynchronous scenario due to the presence of clock drift, with ideal code phase retrieving.

IEEE 802.15.4a emission mask in the 3–5 GHz is considered.

For what concerns the clutter, a worst-case of uniform power delay profile in the overall interval T_p is considered, with paths spaced 0.95 ns apart, each path with amplitude characterized by Nakagami- m fading, with $m=3$, and a root-mean-squared value of 0.5 mV at the receiver.

In Fig. 19, we report the receiver operating characteristic (ROC) corresponding to perfectly synchronous and asynchronous scenarios with ideal code phase retrieving.

As before, we consider a useful tag placed at 7 m from the reader and 59 interfering tags uniformly distributed in 2 meters around it.

Orthogonal Walsh codes in synchronous scenario represent the benchmark, since the interference is completely removed when they are adopted. On the contrary, their performance drastically degrades when the scenario becomes asynchronous. Extended Gold codes (obtained by lengthening of one chip the Gold codes without any kind of phase optimization when aligned) allow satisfactory detection capabilities both in asynchronous conditions while in synchronous one they present a loss. Orthogonal Gold codes represent instead the best trade-off for both scenarios since they achieve a detection rate higher than 0.8 with a false alarm of 10^{-3} also in the asynchronous scenario, while maintaining the optimal behaviour of Walsh codes in perfectly synchronous scenario.

3.6 Synchronization Schemes

In this section, we introduce the principles and procedures for synchronization in backscattered UWB RFID systems.

We distinguish two important aspects of the synchronization.

- Clock synchronization.
- Code synchronization.

Both the proposed tag architectures proposed in Sec. 3.4.1 relies on the use of UHF signaling for time and frequency synchronization. However, when backscattered UWB is used for communication, there is an extra synchronization effort required due to the need of aligning reader’s and tag’s spreading codes.

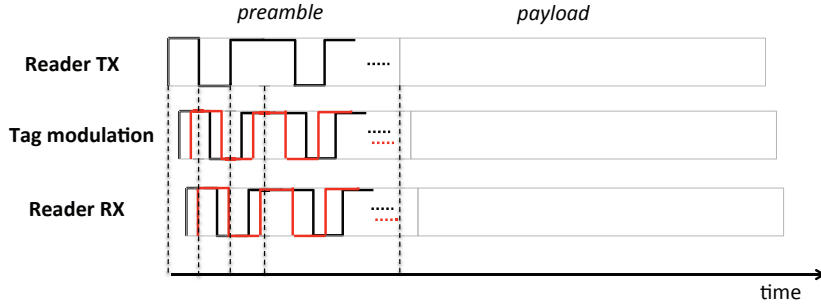


Figure 20: System time evolution for data synchronization architectures.

3.6.1 Clock synchronization

Frequency and time synchronization are critical in backscattered UWB data due to the peculiar system architecture. We assume in this section that both the reader and the tag are equipped with UHF circuitry compatible with the EPC Gen.2 standard [10]. Moreover, we consider separate antennas for UWB and UHF signals at the tag.

The internal clock of the tag might differ from the reader's clock. By keeping a simple tag's implementation, a free running oscillator could be implemented in the tag. However, clock drifts and code offsets become critical problems for the complexity of the reader. Before decoding the received data, transmitter frequency and timing must be synchronized. Nevertheless, the way of synchronizing the transmitter and receiver depends on the structure and the technology used in the communication system.

Powerful acquisition techniques and the TOA estimator robust to clutter, e.g. as those proposed in Xu and Law [16], can be adopted at a reader's side to compensate for clock offset. The complexity of the synchronization algorithms is reduced when tags are equipped with UHF receivers. By the exchange of UHF signaling, the reader can force alignment of the tag's clock. This is performed in EPC Gen.2 devices with standard mechanisms [17, 18] that we describe in the following.

Every reader message must begin with a preamble or a frame-synchronization string. Query command must begin with a preamble to indicate the start of the inventory round while other commands begin with a frame synchronization. A system time representation is reported in Fig. 20.

The reader transmits a continuous wave (CW) to the tag. A Pulse Interval Encoding (PIE) is used in downlink (DL) to transmit data from the reader to the tag. This encoding method implicitly includes the clock to detect the bit (or symbol) boundaries easily at the tag with a small hardware.

The first step in the demodulation process in the downlink (reader-to-tag) is to suppress the carrier by detecting the envelope. The envelope is passed through a trigger which detects the rising and falling edges of the envelope and cleans it from the noise. The output of the trigger is inverted to get the clock which is used in the digital part of the tag and to reset the integrator which integrates the output of the trigger. The data is passed through the digital part in-parallel with the clock if it needs to be processed.

An alternative option for clock synchronization is to use synchronous detectors [19]. However, they are more complex than envelope detectors, and they require a phase-locked loop and a mixer.

3.6.2 Code synchronization

The tag's spreading code is not in general time aligned to the reader's code. Hence the received signal model of UWB backscattering system is significantly different from that of conventional UWB system.

During the interrogation phase, the reader transmits a sequence of UWB pulses with distance T_p , modulated with a binary sequence $\{d_n\} \in \{-1, +1\}$ of length N_c , specific to the reader. Each code symbol (chip) is associated to a sequence of N_{pc} elementary UWB pulses such that there is enough energy to decode the chip. To make the uplink (UL) communication robust to clutter and to allow for multiple access, each tag is designed to change its status at each chip time, according to a periodic code $\{c_n\} \in$

$\{-1, +1\}$ of length N_c . The data information at the tag is then modulated at each symbol time $T_s = N_c N_{pc} T_p$. The backscattered signal at each chip is the combination of reader's and tag's code.

The code synchronization is achieved then in two steps. First, the reader should synchronize with the tag's code. Once the reader and tag are aligned, the reader needs to recover the signal TOA estimation for fine synchronization. The tag's code might include strong clock drift and has a different time base than the signal of the reader. The de-spreading is then performed by considering the composite sequences given by the reader code (not shifted) and local shifted replicas of the tag code. In this way, testing in parallel different tag code shifts, it is possible to evaluate and correct the entity of the tag clock drift by taking the maximum of the de-spreading correlations.

It is then fundamental to design a preamble structure that allows the reader to perform the two-step synchronization properly.

3.7 Energy harvesting component

Research work was oriented at defining a possible architecture for the energy harvesting component. In general, the component is required to wake-up and operate autonomously with very low levels of incident radio-frequency (RF) power, down to few μW . Under these operating conditions, the voltages available on the output of the rectenna are usually very low, down to few hundreds mV. This means that, if the available RF energy in the ambient is the only source, wirelessly powered systems may fail to autonomously operate due to their low available DC voltages. As a matter of fact, in battery-less implementations, sufficient levels of power cannot be exploited by electronic circuits unless the developed voltages on the rectennas are also comparable with the threshold voltage of diodes and transistor, even if sufficient levels of power are available. In addition, in the maximum power point (MPP), rectennas output a voltage which is roughly a half of its open circuit voltage.

In order to guarantee self-activation of the circuit, the rectenna in Fig. 21 should provide the highest possible output voltage. The static transfer characteristics are depicted in Fig. 22. This can be accomplished by reducing the current drawn during the start-up phase and, once activated, switch to a maximum power point tracking (MPPT) mode. However, the rectenna is usually optimized for providing the highest possible power when biased by its optimum load. For this reason, during start-up, the rectenna will be biased poorly, although higher voltages are provided.

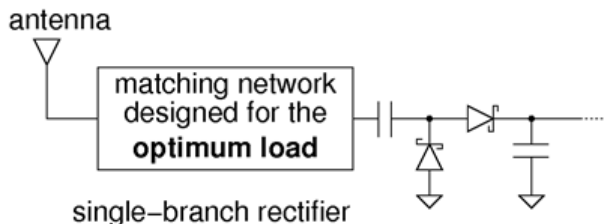


Figure 21: Schematic of a rectenna with a single RF power path

In order to overcome such issues, the following architecture of the energy harvesting component is proposed. Differently from other works, in which start-up circuits are implemented only in the base-band section, the antenna is loaded by a parallel connection of two different rectifier/matching network assemblies to operate alternatively during the start-up and the boost converter operations. The first rectifier and matching network are designed together with the rectenna optimum load to maximize RF-to-DC conversion efficiency.. In this configuration, the DC-DC converter should dynamically bias the rectenna in its MPP condition, in which the available voltage may be lower than the minimum supply voltage required by the converter. The second rectifier and matching network are designed by assuming the input impedance of the converter start-up stage as a load, which should bias the rectenna for providing both the required DC voltage and the DC power needed for circuit operation. In this context, it is not essential to optimize the maximum efficiency: the main purpose is to let the rectenna output the highest possible

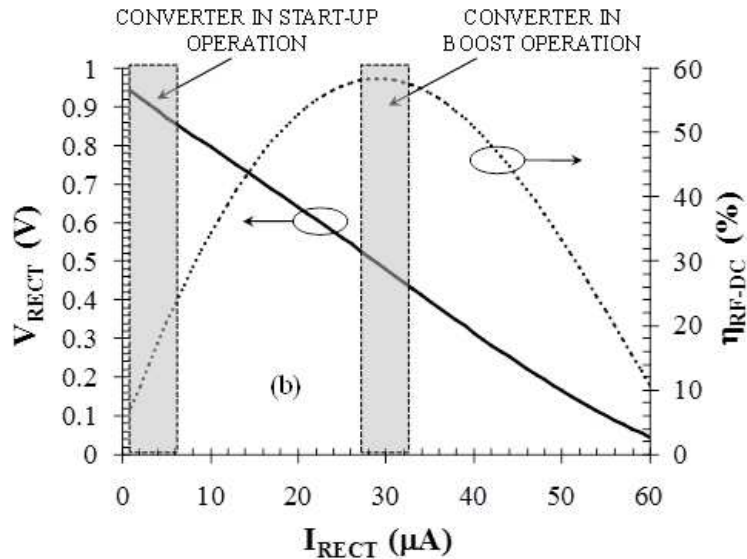


Figure 22: Typical static characteristics of a reference rectenna design.

voltages, in order to fulfill the minimum voltage requirements. Given this primary objective, the rectenna may not be biased in its MPP. Along with this, in order to keep voltage drops low, the current drawn by the start-up circuit should also be the lowest possible. However, this is a necessary condition to allow system activation of a battery-less system from a discharged state when very low input power is available. In such conditions, without these specific optimizations, the energy conversion would not be able to start. The drawback may be a longer start-up time when high input power is available. More specifically, the use of the two-branch rectifier allows to exploit the low voltage and current requirements of a charge pump circuit during start-up, and of a highly efficient switching converter with MPPT during steady-state conversion.

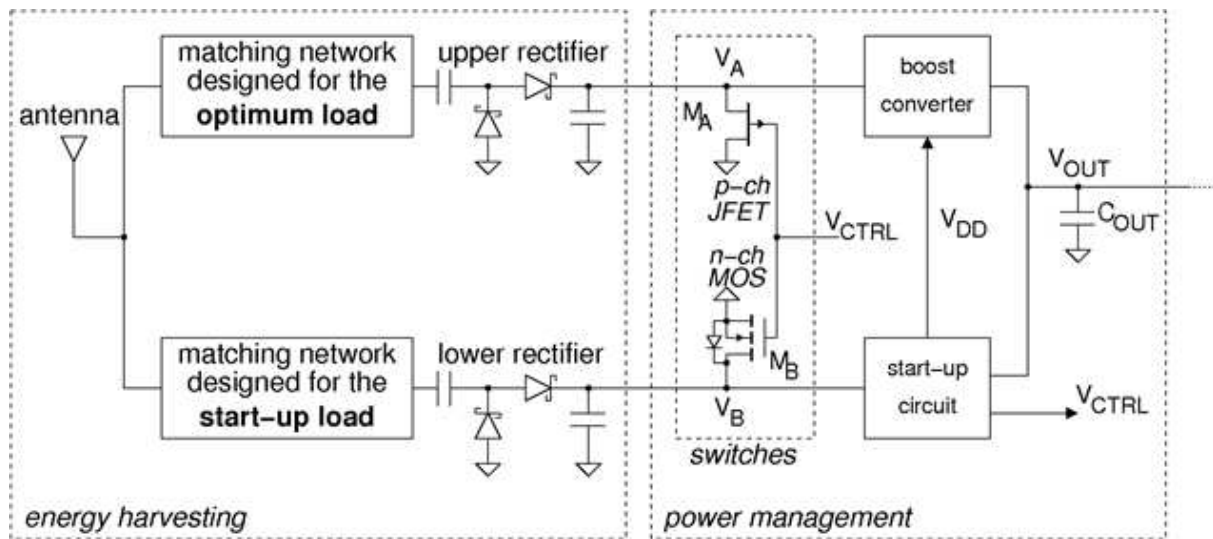


Figure 23: Proposed architecture for the energy harvesting component.

A reference architecture for implementing such double-branch architecture is shown in Fig. 3.7. The switches are shown with reference components in order to show its behaviour, and other implementations are possible. This kind of architecture allows to provide two independent optimization of RF power paths for the two power conversion circuits, which operate in very different operating points. The start-up path

is provides higher voltages and a higher converted power when the start-up circuit is the actual load. When a sufficient voltage is stored on the output capacitor, and input power is sufficient as well, energy conversion can be sustained and the boost converter branch is enabled, with a specific optimization for maximizing the output power. Of course, the coexistence of the two branches, alternatively loaded by a short-circuit, needs to be considered in the non-linear design of each one, in order to accurately predict the effective behaviour. In Fig. 24 the simulated two-branch rectifier reflection coefficient is plotted versus the received RF power P_{RX} : these plots show that the new solution is able to preserve a very good antenna matching to each parallel connected sub-system, all over the received RF-power range addressed in the respective design.

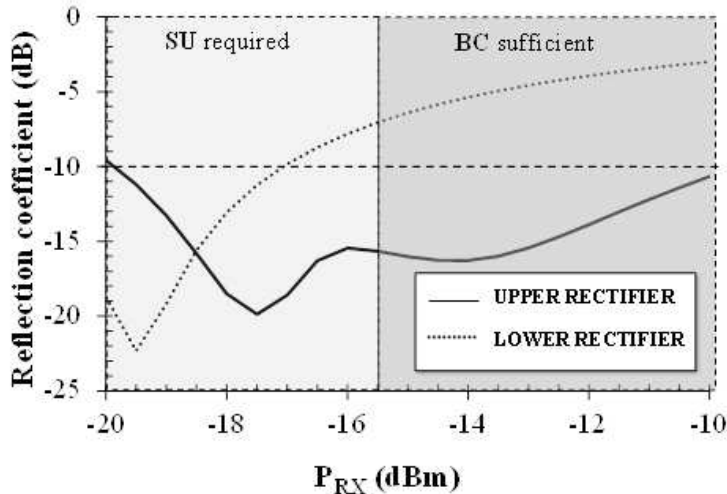


Figure 24: Reflection coefficient at the antenna port of the load-modulated rectifier (solid line: the upper rectifier is loaded by $Z_{BC} \approx 10k\Omega$, its optimum load, and the lower rectifier load is shorted to ground; dashed line: the lower rectifier is loaded by a fixed $Z_{SU} \approx 200k\Omega$ and the upper rectifier load is shorted to ground

3.8 Sensor component

In a sensor architecture a primary role is played by its electrical interface; which detects, amplifies and digitizes the electrical quantity coming from the sensor. The proposed technology is intrinsically useful for many kind of applications thanks to its characteristics of eco-compatibility and low energy consumption. Since several types of sensors are available on the market we opted for a universal sensor interface able to acquire different kind of electrical quantities, although we limited the project to two reference scenarios (*i.e smart band-aid and blood bags tracker*). In this way, the developed green tag is as more general as possible and can be used to detect different physical quantities in different scenarios.

The most suitable architecture for a general sensing electrical interface is based on micro- and nano-power oscillators. In such an architecture it is possible to link the oscillation period to several parameters or components. For instance, variations in capacitance or resistance associated to transduction produce changes in frequency of the generated oscillating waveform, making the electrical interface suitable for both capacitive and resistive sensors. Oscillator-based sensing interface is composed of three elements as shown in fig. 25 [20]:

- the sensing oscillator generating the variable-frequency waveform;
- a reference oscillator generating the base time;
- a time-to-digital converter that could be a counter in its simplest form.

The architecture is intrinsically a low-power structure since it does not require neither operational amplifiers nor ADCs. Accuracy and resolution of the measurement are directly related to the quality (*i.e. jitter*

in time domain and *phase noise* in frequency domain) of the scheme realizing the oscillators.

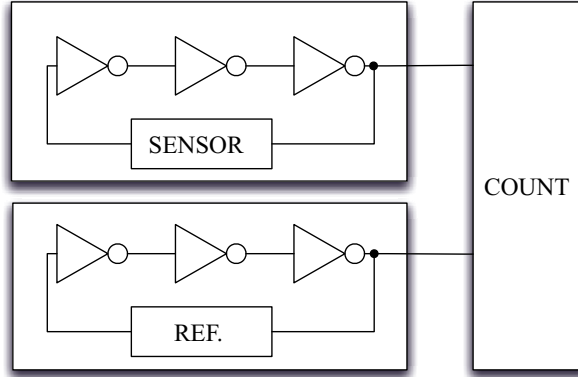


Figure 25: General architecture of oscillator-based sensing interface

Oscillator architectures can be divided in two big categories:

1. *Harmonic oscillators*. Two or more energy reservoirs are required. They can be either of a different type or of the same type, if combined with a resistive element. Harmonic oscillators can be built using only linear component and hence they are producing pure sinusoidal tones.
2. *Relaxation oscillators*. Only one energy reservoir is required in combination with a resistive element and a nonlinear component. The current through or the voltage over the energy reservoir is switched at certain reference levels generating waveforms with a discontinuous first derivative.

A useful equation for phase noise calculation in oscillators is the Leeson's formula [21]:

$$L(f_m) = 10 \log \left\{ \left[1 + \frac{f_0^2}{(2f_m Q_L)^2 \left(1 - \frac{Q_L}{Q_0} \right)^2} \right] \left(1 + \frac{f_c}{f_m} \right) \frac{F k T}{2 P_0} \right\}, \quad (21)$$

where $L(f_m)$ is the ratio of sideband power at f_m frequency and 1Hz bandwidth to total power expressed in dB, f_m is the frequency offset from the carrier, f_0 is the oscillating frequency, Q_L is the quality factor of the circuit accounting for the load, Q_0 is the quality factor without the load, f_c is the flicker corner frequency, F is the noise factor, k is the Boltzmann constant, T is the temperature in Kelvin degrees and P_0 is the average power at oscillator output.

According to (21) the noise performance of an oscillator circuit is directly proportional to its quality factor (Q). Thus, harmonic oscillators based on LC passive components or mechanical resonators exhibit the lowest phase noise possible [22, 23]. However, harmonic oscillators are quite complex and could be difficult to integrated into a silicon chip (e.g. inductor used in LC harmonic oscillators). On the other hand, relaxation oscillators are smaller and easy to integrate in standard CMOS technologies; they dissipate less power but have worst noise performance [24]. For these reasons relaxation oscillators prove to be the best architecture able to achieve the characteristics of eco-compatibility and low energy consumption required by the project. A general scheme for a sensor interface based on relaxation oscillator is shown in 26. Note that the oscillation period is proportional to both capacitance and resistance, following:

$$T_{\text{OSC}} = \frac{C R I_0}{I_1} + t_p, \quad (22)$$

where R , C and I_1 are sensing parameters, I_0 is the bias current and t_p is the reset time.

3.9 UWB backscatter modulator

The tags with passive architectures are characterized by the absence of an active transmitter in order to reduce the circuit complexity and the power consumption. The data transmission is performed by

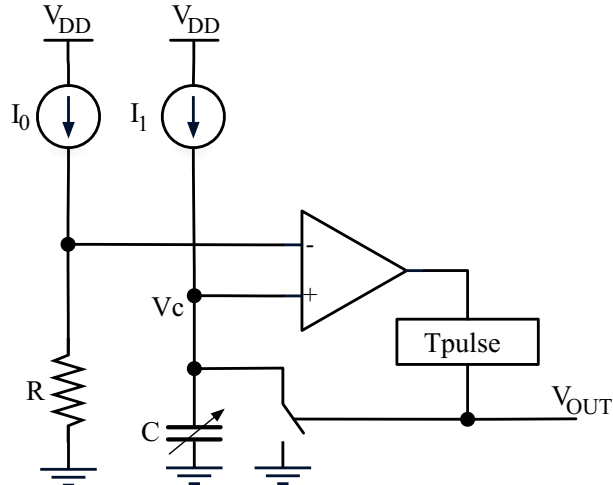


Figure 26: General scheme of relaxation oscillator

modulating the incident wave, provided by the reader, and backscattering the modulated wave to the receiver, by means of a backscatter modulator. The modulation and the reflection of the incident wave is performed by varying the load impedance (reflection due to mismatch) of the tag TX-RX antenna (see Fig. 27). A preliminary study about the backscatter modulator architecture and its operating principle is documented in GRETA Deliverable 1.

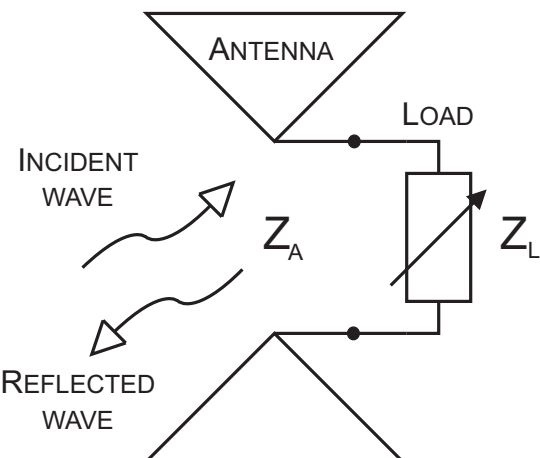


Figure 27: Backscatter modulator operating principle.

Several modulation techniques can be used for UWB communication. The main techniques are:

- amplitude shift keying (ASK);
- phase shift keying (PSK);
- pulse position modulation (PPM);
- pulse amplitude modulation (PAM).

The modulation technique adopted in the present project is the ASK. The different antenna load conditions can be obtained by means of an open circuit (OC) and a short circuit (SC) at the antenna terminals (see Fig. 28). In the two cases the total reflection is achieved with a phase difference between them equal to 180 degrees. The reflection coefficients can be computed with the following equation: $\Gamma_L = (Z_L - Z_A)/(Z_L + Z_A)$, where Z_L is the load impedance and Z_A is the antenna impedance. In the ideal case $Z_L = \infty$ and $\Gamma_L = 1$ for the OC, and $Z_L = 0$ and $\Gamma_L = -1$ for the SC. The OC and the SC can be realized by means of a switch connected to the antennas terminals and controlled by the control unit of the tag (see Fig. 29).

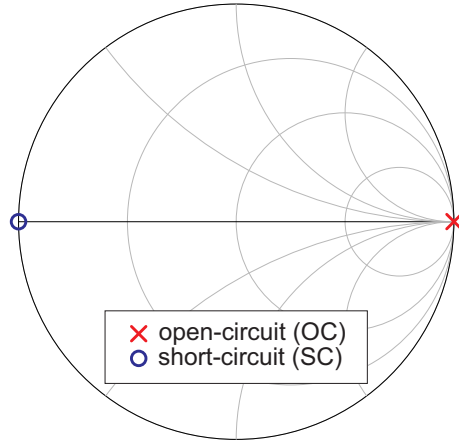


Figure 28: open circuit (OC) and short circuit (SC) on the Smith chart.

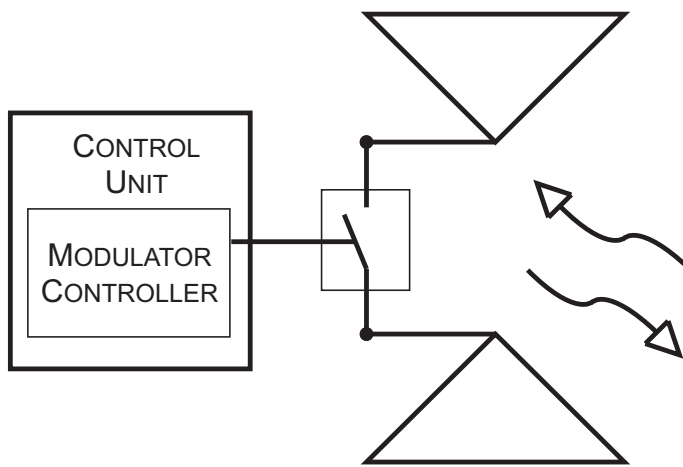


Figure 29: Backscatter modulator architecture with control unit.

The main components for the switch design may be diodes or transistors; these devices are generally characterized by the static and the dynamic power consumption. The static power consumption P_S (eq. 23) is the power dissipated in a static condition and it is due to the bias current flowing on the internal device resistance R_S that is used to maintain the device in a desired state, generally the high logic level (switched-on), when a voltage V_H is applied to the device; the dynamic power consumption P_D (eq. 24) is the power dissipated during the switching (assuming V_H the voltage related to the high logic level and 0 the voltage of the low logic level) and it depends on the charge and discharge of the device parasitic shunt capacitance C_S , and on the switching frequency f_S . Fig. 30 highlights the static and the dynamic power consumption. Devices like BJT and diodes present both the static and dynamic consumptions depending on the operating frequency while, by using MOSFETs and FETs, the static power consumption is drastically reduced thank to the high R_S (only the device leakages contribution to the static power consumption is present). Considering a low operating frequency (about 100 kHz), MOSFETs and FETs are the best candidates for their low power consumption in agreement with the specifications of passive and energetically autonomous tags, considering the backscatter modulator design with IC technology. While, for a backscatter modulator designed with lumped components, the PIN diodes result to be a good compromise between performances and consumptions. Switch structures examples based on one and two transistors are shown in Fig. 31 and an ultra-low power switch architecture is documented in [25]; backscatter modulator architectures based on PIN diodes are shown in Fig. 35. In Sec. 3.9.1 the preliminary results of a backscatter modulator designed with lumped PIN diodes are shown.

$$P_S = \frac{V_H^2}{R_S} \quad (23)$$

$$P_D = V_H^2 \cdot C_S \cdot f_S \quad (24)$$

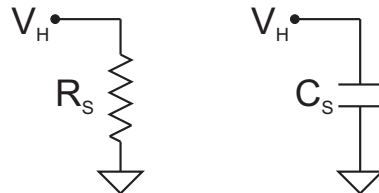


Figure 30: Equivalent circuits of the switch for the static (left) and the dynamic (right) power consumption.

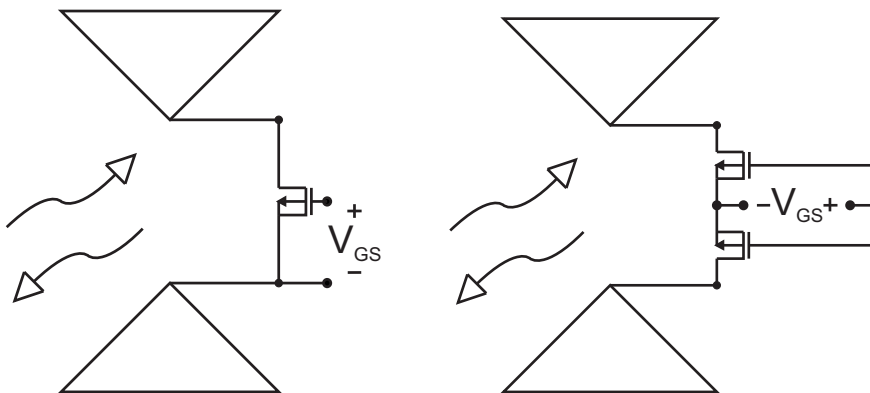


Figure 31: Proposed architectures based on IC technology with one MOSFET (left) and two MOSFETs (right).

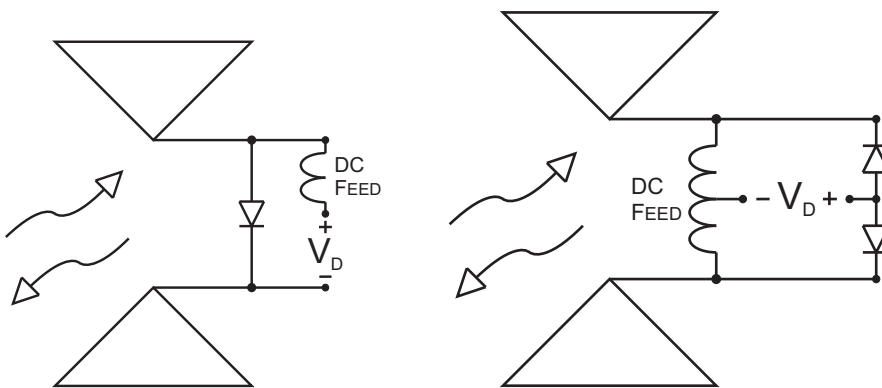


Figure 32: Proposed architectures based on lumped components with one PIN diode (left) and two PIN diodes (right).

The technical specifications of the backscatter modulator, in agreement with the UWB communication standards, are resumed in Table 5. The technology proposed is the UMC Low-voltage CMOS 180nm (or UMC L180). The fundamental advantages of the proposed CMOS technology are its low cost and the low gate delay (or logic gate propagation delay) lower than 60ps.

Table 5: UWB backscatter modulator specification.

Parameter	Value	Description
T_{SW}	1-2 ns	switching time
T_S	10 us	average symbol time
f_S	100 kHz	average switching frequency
B_W	3.1-4.8 GHz	operating frequency band
P_C	10 uW (optimal) - 100 uW (maximum)	power consumption

3.9.1 Preliminary study with lumped diodes

The preliminary results obtained simulating the architectures in Fig. 35 are reported in this section. Two different PIN diodes have been used: the Skyworks SMP1322_079 and the Skyworks SMP1345_079. The simulated schematic are shown in Fig. 33. The reflection coefficients at the antenna terminals are computed for two cases: when the diodes are switched on and off. The antenna is modeled by means of port (impedance equal to 50 Ohm) and the DC blocks are used to avoid the presence of direct current on the antenna (in the real case the DC blocks are not required for unconnected two arms antenna). The DC feeds are required in order to isolate the DC voltage source from the RF signal. The static power consumption is computed measuring the current flowing in the probe item.

The simulations results, in the frequency range 3.1-4.8GHz, are plotted in Fig. 33 and Fig. 33 for the Skyworks SMP1322_079 and the Skyworks SMP1345_079, respectively for both the architectures. A good reflection coefficient magnitude, over 0.95, is achieved in all the cases. A fundamental parameter is the difference between the SC and the OC phases in order to evaluate the correlation between the reflected pulse in the two cases. The deviation of the reflection coefficients from the ideal ones in Fig. 28 is due to the package and diodes parasitics. There is not power consumption when the diodes are switched off (bias voltage equal to 0), but a static power consumption is present when they are switched on.

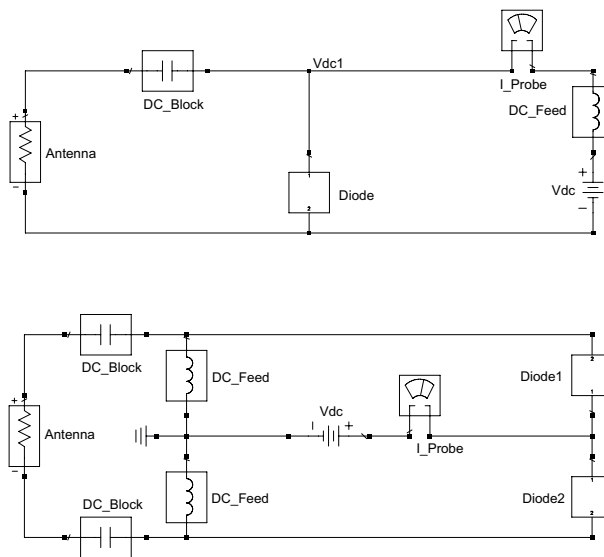


Figure 33: Schematic of the architectures based on lumped components with one PIN diode (top) and two PIN diodes (bottom).

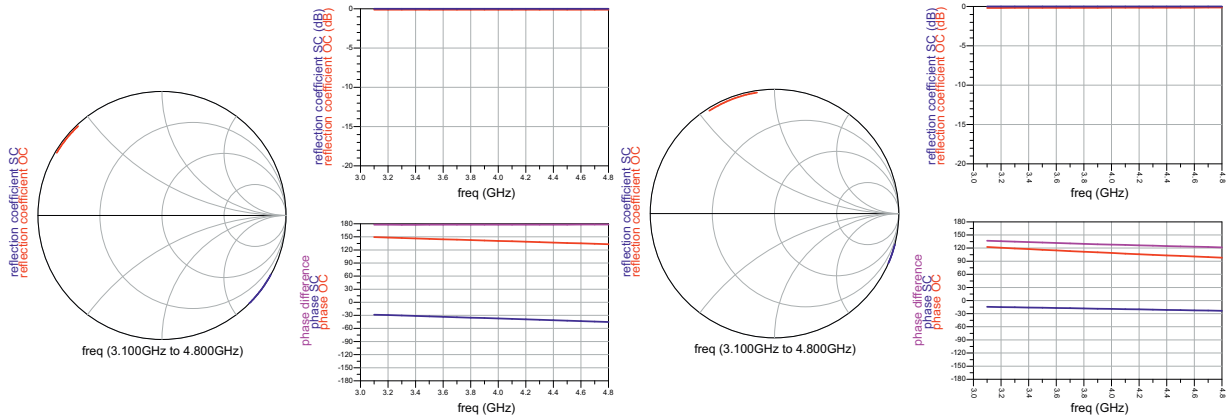


Figure 34: Simulation results of the architecture with one diode (left) and two diodes (right). Diode model Skyworks SMP1322_079. The static power consumption is 0.36 mW and 3.65 mW for the one diode and the two diodes architectures, respectively.

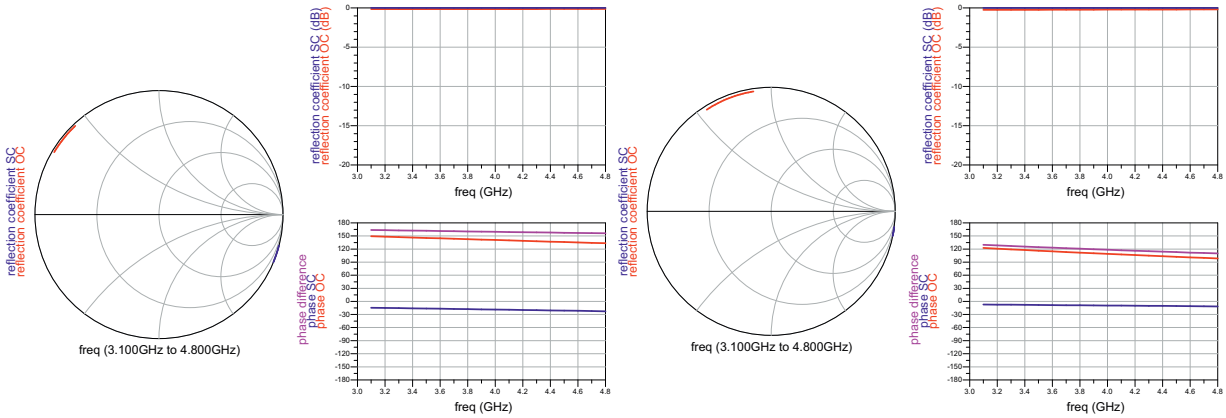


Figure 35: Simulation results of the architecture with one diode (left) and two diodes (right). Diode model Skyworks SMP1345_079. The static power consumption is 1.75 mW and 19.23 mW for the one diode and the two diodes architectures, respectively.

3.10 Antenna system

3.10.1 Harvester antenna

The purpose of this section is to provide a highly efficient rectifying antenna (rectenna) able to collect energy from the environment and to provide sufficient DC power to supply the entire GRETA system. As we mentioned in the previous deliverable DC power collected by ambient RF sources turns out to be extremely variable depending on which scenario we operate in and in most cases is not sufficient to provide an adequate amount of energy, especially in indoor environments [26]. For this reason, we already stated the necessity to exploit dedicated RF showers to provide the required energy. We proposed two different topologies for the harvester antenna, both taking into account the dual functioning of the tag system: harvester antenna and communication antenna in the UWB band. The first architecture consisted on the realization of two different section, each one dedicated to its own single functionality, and therefore two (or more) separated antennas. In this case, for the harvesting section, traditional UHF antennas can be used. A meandered planar dipole [27] operating in the 868 MHz frequency is then considered, due to its high efficiency (limited only by paper substrate losses), low-directivity property and ease of realization in the space around the UWB antenna. A possible implementation is shown in Fig. 36, where a U-shaped dipole is placed near a UWB antenna (an Archimedean spiral antenna, in this case).

This architecture can be further extended by placing two cross-polarized dipoles around the UWB

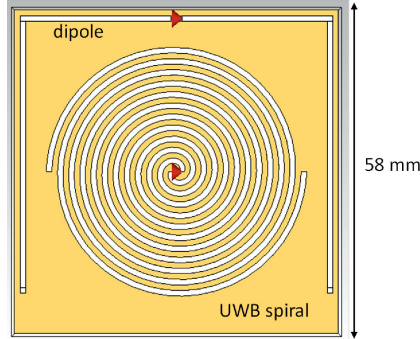


Figure 36: Standard solution: UWB antenna and one dipole harvester antenna on paper substrate.

antenna. This permits to increase the whole system degrees of freedom, since the ability to recover energy from both vertically and horizontally polarized signals allows a random distribution of the tags. A possible implementation of this second topology is shown in Fig. 37

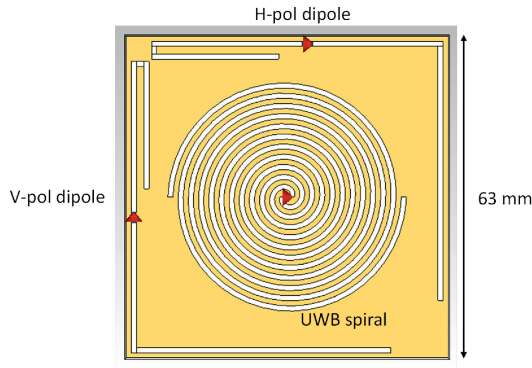


Figure 37: Standard solution: UWB antenna and two cross-polarized dipole harvester antennas on paper substrate.

With this topology efficiencies of the order of 85% with omnidirectional radiation pattern in the plane orthogonal to the horizontal arm of the dipole can be obtained. A much more challenging solution, though, would be that of integrating the communication and harvesting tasks in a single, compact, antenna. We thus decided to investigate also a unique antenna topology, thought as an alternative to the UWB antenna in SIW technology proposed by UNIPV. The RF shower operating frequency, in this case, has to be carefully selected in the available operating bandwidth. A possible solution for harvesting purposes could be the use of frequencies near the lower edge of the UWB band (e.g. WiFi frequency = 2.45 GHz) in order to keep the UWB band completely free for communication. We have thus considered as a possible solution an Archimedean spiral antenna [28] of the same kind reported in Fig. 36. In order to cover the desired band (roughly from 2.4 up to 5 GHz) a 53-mm² paper sheet is adopted (see Fig. 38).

The simulation of such subsystem predicts efficiencies ranging from 75% up to 85%, from 2.4 up to 5 GHz, respectively, and a bidirectional behaviour (orthogonal to the antenna plane) in the whole frequency band. Moreover, in this case circular polarization is automatically guaranteed, which is a highly desirable property as it provides the ability to capture any kind of receiving field. Other UWB antenna topologies have been considered, such as logarithmic spiral antenna [29], in order to compare different topologies performance. Several simulations of this antenna nevertheless showed very similar results in term of radiation properties at the cost of slightly increased overall size. For this reason the Archimedean spiral antenna was kept as UWB antenna topology for all further investigations. In order to evaluate the possibility of a practical usage of the 2.45 GHz as the harvesting frequency, a first estimation of the rectified power PDC was considered. We have thus carried out preliminary optimizations of the matching network

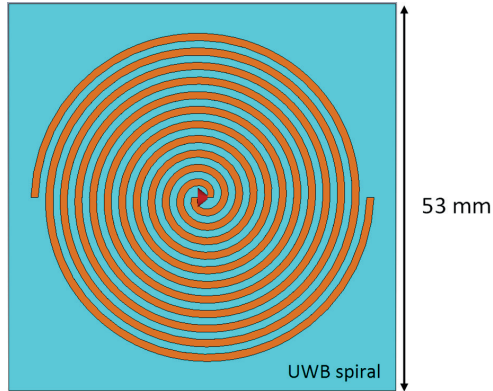


Figure 38: Standalone UWB spiral antenna.

between the harvester antenna and the rectifying section, referring to the 500 mW (27 dBm) maximum ERP for indoor 2.45 GHz-RFID standard [30]. The simulation results have shown how poor the amount of energy can be with this configuration, even in the considered free space conditions: at a distance of merely 2 meters from the RF shower the available rectified power falls under $10 \mu\text{W}$. We therefore decided to investigate the possibility to use the more convenient 868 MHz frequency for harvesting purpose, both for the higher transmission power allowed by the UHF-RFID standard [31] and for the lower free space loss. In a first attempt to define a proper configuration able to provide both 868 MHz harvesting and UWB communication functionality with a single antenna, the original Archimedean spiral topology (see Fig. 38) has been expanded, in order to cover a wider bandwidth including the 868 MHz frequency. UWB antennas such as the Archimedean spiral provide constant behavior over the whole UWB band thanks to their auto-complementarity and auto-similarity properties. According to the auto-similarity property, the Archimedean spiral antenna irradiates like a full wave loop antenna with a circumference equal to the working wavelength λ . Therefore antenna radiation properties remain almost identical by varying the working frequency since the so called active zone, in which the spiral radiates like a loop antenna, moves to a different circumference according to the relation $\lambda = 2\pi R$, where R is the circumference radius. This means that reaching good radiation properties at the 868 MHz frequency implies a remarkable increase of the spiral dimensions. Very good results have been achieved by an Archimedean spiral with lines width of 2 mm and overall dimension of about 130 mm. Radiation efficiencies in the UWB band are slightly higher than 90% and of approximately 86% at the harvesting frequency, while circular polarization is guaranteed in the whole working frequency band. Such a structure however is undoubtedly too big for the assigned goals (maximum substrate side 5-6 cm²) and would inevitably reduce the number of possible applications imagined for the tag. We hence need to find a way to reduce the overall dimensions thus keeping the wanted behaviour over the whole working frequency band. A first attempt in this direction was done implementing the so called gap-loading technique [32] [33], which promises to reduce the antenna dimensions by introducing a capacitive gap between the antenna and an external conductor. Simulations show that by placing an external ring near the outer side of the spiral, a reduction of the structure dimension of about 23% can be obtained without altering the antenna radiation properties. The realized architecture is shown in Fig. 39.

Although the gap-loading technique permits to reach a considerable reduction of the tag size, overall dimensions are still too large compared to those we are looking for. Above-mentioned results led to the investigation of a brand new architecture, which gave very interesting results. The starting point for this new and innovative topology is still the Archimedean spiral previously described (see Fig. 38), but the terminal part of the spiral arms have then been extended along the edge of the paper substrate. In this way the two extensions of the spiral create a structure corresponding to a folded planar dipole. Several studies of this innovative topology showed that the dipole behaviour depends on the whole length of the conductive arm, from the feeding point (center of the spiral) to the outer extremity. We therefore managed to create a structure able to provide a 1.5λ resonant dipole at the harvesting frequency. The

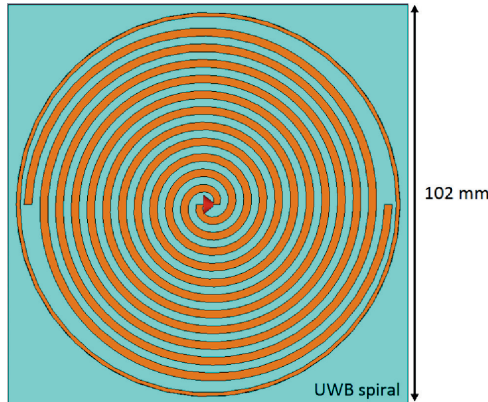


Figure 39: Archimedean spiral antenna working in the (0.868-4.8) GHz band with gap-loading technique

antenna topology is presented in Fig. 40.

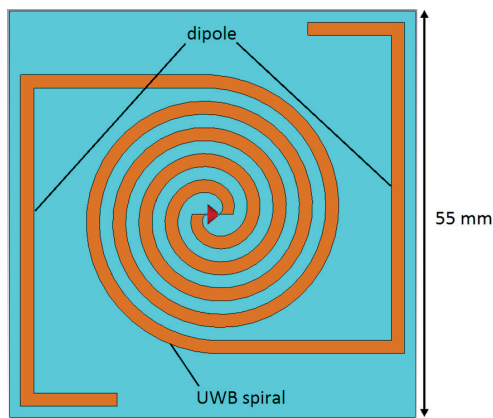


Figure 40: New antenna topology covering UHF and UWB bands

The simulation of such antenna predicts efficiencies in the order of 90% and a bidirectional behaviour in the (3.1-4.8) GHz band (again orthogonal to the antenna plane), while at 868 MHz efficiency is about 63% and an omnidirectional radiation pattern in the plane orthogonal to the horizontal arm of the dipole is obtained. Of course the field radiated by the dipole results to be linearly polarized in the horizontal plane. In Fig. 41 the radiation surfaces at the harvesting frequency and at the UWB center frequency are given.

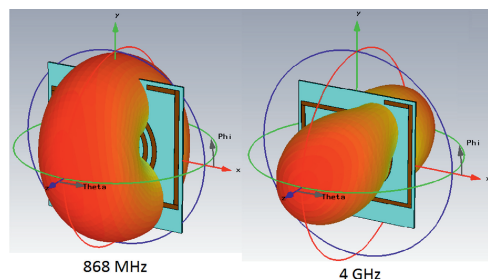


Figure 41: Radiation patterns of the proposed antenna at 868 MHz and 4 GHz

The optimum co-existence of the two antennas is demonstrated by the comparison of the spiral performance with and without the dipole. The corresponding simulated reflection coefficient (normalized on 120Ω) in the UWB band is reported in Fig. 42.

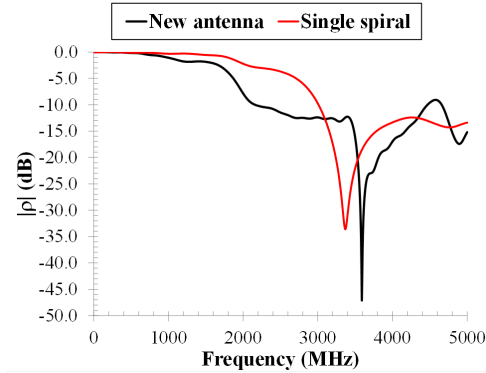


Figure 42: Reflection coefficient behaviour for the new antenna and a standard Archimedean spiral

From inspection of Fig. 43, where the real and imaginary part of the new antenna impedance are reported, it can be easily evinced that the total length of the dipole provides a 1.5λ behaviour (third null value of reactance). This choice is due to a twofold reason: firstly, a standard half-wavelength length could be obtained by a reduction of the spiral number of turns, but at the expense of the spiral performance, especially in the higher frequency range; secondly, the real part of the antenna impedance has extremely low values in the half-wavelength case. This value is about 15Ω in the present topology, while the auto-complementary behaviour of the spiral in the UWB band is demonstrated by the almost constant value of the impedance (about 120Ω).

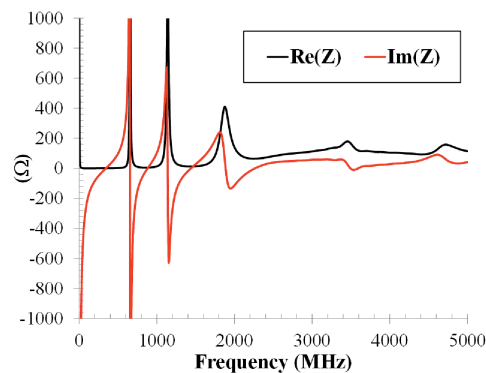


Figure 43: New antenna impedance behaviour in the entire frequency band

3.11 Green Technologies

3.11.1 Selection and EM characterization of paper-based substrates

The low cost is one of the most important features of paper when used as a substrate for microwave applications. This peculiarity derives from the huge amount of paper produced every year. It is intuitive that, due to the large use of paper worldwide, a large number of different types of paper can be encountered in the market.

Physical characteristics of paper

The different types of paper can be classified according to the weight (grams per square meter, GSM), the thickness, the composition and the roughness. It is important to give a brief introduction to every single feature from the perspective of microwave applications.

Common types of paper have slightly different density values, so that considering the value of GSM is similar to considering the sheet thickness. The measure of GSM is a good starting point to evaluate the

Table 6: Physical characteristics of paper samples

Mill	Name	GMS [g/m2]	Thick [um]	Composition	Roughness
Burgo	raw paper	331	500	100% cellulose	low
Burgo	R4	350	350	100% cellulose	low
Burgo	PM1	235	300	100% cellulose	high
Fabriano	Multipaper	300	350	100% cellulose	low
Fabriano	Studio watercolor	300	400	50% cellulose 50% cotton	low
Fabriano	Fabriano 5	300	500	50% cellulose 50% cotton	high
Fabriano	Artistico	300	450	100% cotton	low
Momo	07	350	460	cardboard	low
Momo	07	400	530	cardboard	low
Momo	07	500	665	cardboard	low

substrate thickness in a paper-based device. In the application in SIW components, the substrate thickness is directly related to conductor losses: thicker substrates allow to achieve lower losses. Furthermore, due to the typical non-planarity of thin substrates, the choice of relatively large substrate thickness is preferred. On the other hand, a thicker substrate could be too stiff for those applications that need the bending of circuit (e.g., wearable tags or conformal antennas), thus partially spoiling the paper flexibility properties.

Also the composition of paper affects losses. During the cycle of paper fabrication, three main components are involved: cellulose, cotton and glue. Different percentages of these products lead to different electromagnetic characteristics of the substrate. First of all, the percentage of cellulose and cotton affects the dielectric losses. In the case of a high rate of cotton, the substrate tends to collect humidity, with the consequent increase in power dissipation due to water absorption. Paper intended for artistic purposes is composed of cellulose and cotton in the same quantity, and this leads to high dielectric losses. The value of the dielectric permittivity could not be predicted simply by the paper composition, because all three components could affect the value of permittivity. Generally speaking, paper types with same thickness and lower density likely exhibit lower dielectric permittivity, due to the higher percentage of air-filled space.

Finally, the surface roughness of paper mainly affects conductor losses. In the fabrication process of paper-based SIW devices and circuits, the top and bottom metal layers are implemented by gluing two aluminum sheets at the two sides of the paper substrate. The surface roughness has a direct impact on the metal layers, with a consequent increase in conductor losses.

Selection of the types of paper

The first step that leads to the electromagnetic characterization of paper-based substrates is the search for companies that produce paper and that are potentially interested in the development of special paper for electronic applications. Among them, three companies have been contacted, which have provided different types of paper samples. The companies involved in this activity are:

- Fabriano (Fabriano, Ancona, Italy) [34]
- Cartiera di Momo (Momo, Novara, Italy) [35]
- Burgo Papers (Altavilla Vicentina, Vicenza, Italy) [36].

The characteristics of the provided samples aim to match the constraints mentioned above for microwave applications: high GSM, large thickness, low humidity percentage and low roughness. Table 6 describes the most representative samples of paper substrate that have been received.

Besides the samples provided by the aforementioned paper mills, other four types of paper have been taken into account. The first type is standard photographic paper, which is typically available in one single thickness value of 230 microns. Larger values of substrate thickness can be achieved by stacking more paper sheets: for instance, by using three sheets it is possible to obtain a substrate thick enough for microwave applications. Furthermore, the common 100% cellulose 80 GSM copy paper by Fabriano has



Figure 44: LPKF E33 milling machine.

been tested. In this case, the thickness of the single sheet is 100 microns. Also this thickness value is typically not enough for microwave applications, and the manufactured substrate can be composed by six or more layers. Another substrate taken into account is watercolor paper: in this case, the thickness of a single sheet is 400 microns, which is large enough for intended applications. However, the percentage of cotton and the surface roughness are quite high in this type of paper. Finally, a corrugated paper has been considered. This paper is 1.5 millimeters thick, with a very low density (due to the large content of air) and very high surface roughness.

Fabrication of circuits on paper

A proper manufacturing process for paper-based devices is required, together with the electromagnetic characterization of substrates. A low cost prototyping technology was developed for the fabrication of SIW components on paper. It is based on a milling process by a computer numerical control (CNC) machine, able to etch the metal layer on top of a substrate and to drill via holes, which are strictly required for SIW technology. The milling machine adopted in this project is the E33 by LPKF, shown in Fig. 44, with a tool speed of 33000 rpm. The entire manufacturing process of a paper-based device is divided in two different main steps: the substrate manufacturing and the circuit fabrication.

As mentioned above, several sheets of paper are stacked together to match the required thickness of the substrate, imposed by microwave applications constraints. The layers are glued together by employing a thin film of poly-vinyl-pyrrolidone (PVP) stick glue, which determines a negligible increase in the total substrate thickness. For example, a photographic-paper based substrate is manufactured by using three sheets of paper, thus achieving a total thickness of 690 microns [37]. Moreover, SIW technology requires both top and bottom metal layers, to define the double-grounded substrate. The top metallization is realized by gluing an aluminum film with an epoxy glue. The bottom layer is simply metallized by employing aluminum tape. The difference in the fabrication of the two ground planes relies in the subsequent manufacturing: the top layer is subject to milling processing, whereas the bottom layer is typically untouched. In the case of multi-layer SIW circuits, where both layers need to be processed by milling, also the bottom layer is fabricated by aluminum film and epoxy glue.

When the substrate is completely metallized, it is pressed and heated for four hours at the temperature of 70°C. The adoption of epoxy glue together with the heating process are required to enable the subsequent metal etching by the milling machine. The epoxy glue is applied as a paste and it becomes solid after the heating process. Thanks to this process, the milling tool works better and achieves very good performance in terms of precision and sharpness of circuit edges.

The second step of the manufacturing process concerns the via holes realization and the top layer



Figure 45: An example of SIW paper-based interconnect.

etching, in order to prototype the circuit on the paper-based substrate. These two actions are achieved with the aforementioned CNC milling machine. This machine is equipped with spiral drill tools with a diameter ranging from 200 microns to 2 millimeters. As the SIW technology requires tens of via holes in order to define the lateral walls of waveguide, the CNC milling machine is the best solution to realize a very high number of cylindrical shaped holes in few minutes and with perfect alignment. After the drilling process, the etching of the aluminum film is achieved. The most important tools of the machine have conical and cylindrical shapes with various diameter, starting from 250 microns. These tools are suitable to cut the aluminum films and realize the circuit edges. The thinnest mill tools are used for the circuit edges, whereas bigger tools are used to etch wider areas of aluminum. In this way, the process is very accurate where required (usually close to the circuit edges and between small gaps) and faster elsewhere.

After the process that involves milling machine, the fabrication of SIW requires a final step, which is the metallization of the via holes that define the side walls of the waveguide. In order to metalize the via holes, conductive paste is employed and inserted into the holes. This paste contains silver nano-particles that guarantee high conductivity. A final heating process is required in order to reach the highest conductivity allowed by the paste. The circuit is put in the oven for two hours at 100°C. It is important to remark that, in SIW technology, the presence of broken vias between top and bottom metalized faces leads to significant radiation loss. For this reason, each via hole has to guarantee a good electrical connection between the two faces of the circuit. An example of paper-based circuit manufactured employing the described process is shown in Fig. 45.

Characterization of paper substrates

The selection of the optimal substrate for the realization of efficient microwave circuits is one of the major issues from the technological point of view. Concerning paper, the lack of information about its electromagnetic characteristics is an obstacle for its direct use in the fabrication of microwave circuits. Moreover, there is wide availability of different types of paper, which vary in density, coating, thickness, texture. Therefore, it is essential to adopt a systematic process of characterization of paper substrates in order to derive their electrical characteristics, namely the dielectric permittivity (ϵ_r) and the loss tangent ($\tan \delta$). Several methods have previously been used to characterize microwave substrates, including resonant cavities, transmission line resonators, and measurements of group velocity of microstrip and co-planar waveguide structures. The method adopted in this work concerns the study of the frequency response of a microstrip ring resonator [38].

The structure of the circuit consists of a microstrip ring resonator coupled with the input and output microstrip lines through two gaps (Fig. 46). The value of the gap was selected, taking into account the constraints of the manufacturing process. In the design, the terminal section of the microstrip line was modified to increase the capacitance between the microstrip line and the ring resonator, and consequently to achieve a larger coupling.

The frequency response of the ring resonator presents periodic resonances at the frequencies where the length of the ring corresponds to an integer number of effective wavelengths. This technique permits to determine the dielectric permittivity of the substrate from the analysis of the resonance frequencies of

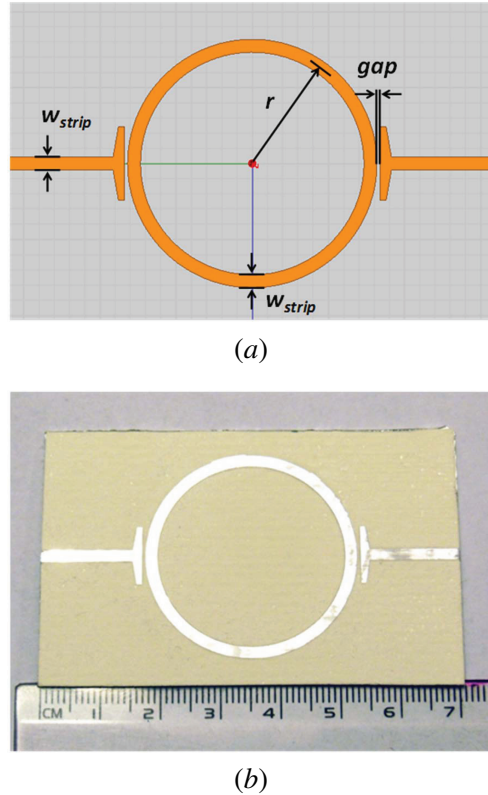


Figure 46: Microstrip ring resonator on paper: (a) geometry of the circuit (dimensions: $r = 16.8$ mm, gap = 0.65 mm, $w_{strip} = 1.9$ mm); (b) photograph of a prototype.

the ring, and the loss tangent from the evaluation of the quality factor of the resonant modes. Specifically, from the physical dimension (ring radius) and the resonance frequencies it is possible to derive the effective relative dielectric permittivity and, eventually, the dielectric permittivity.

The loss tangent of the paper substrate is related to dielectric loss. However, the losses that affected the ring resonator are due to three mechanisms: conductor loss, dielectric losses, and radiation losses. Of course, measurements provide the overall loss, which is a combination of the three effects. In order to determine the sole dielectric loss from measurements, the conductor and radiation losses are computed analytically and subtracted from the total loss calculated from the measured quality factor of the ring [38]. The unloaded quality factor is obtained from the insertion loss and the 3-dB bandwidth measured at the resonant frequency.

The values of the relative permittivity and of the loss tangent of seven different paper substrates, measured with the ring resonator technique, were determined. Starting from the values of ϵ_r and $\tan \delta$ determined by using the formulas in [38], the dielectric permittivity and the loss tangent of the paper were tuned in order to overlapped the simulated and measured frequency response of the ring resonators. An example is shown in Fig. 47. The final values are shown in Table 7 and present a maximum deviation of 4% from the original values. The values of the dielectric permittivity ϵ_r of the paper is in the range of 1.9-2.35 in the frequency band from 2 to 4 GHz for most types of paper, with the only exception of corrugated paper, which has a lower permittivity of 1.46 due to the large presence of air. The values of loss tangent range from 0.037 to 0.06. It is important to note that the results achieved are exposed to uncertainty caused by possible errors due to the ring resonator dimensions, sample thickness, and resonant frequency, etc.

Characterization of the conductor film

The metal employed to define the top and bottom conductive layers of the SIW is the second material

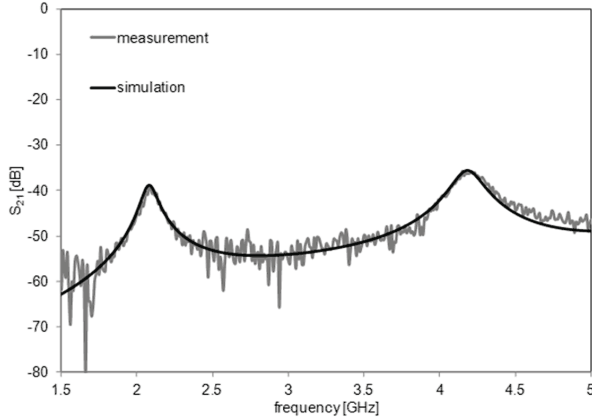


Figure 47: Measured and simulated $|S_{21}|$ of the ring resonator configuration.

Table 7: Measured dielectric permittivity and loss tangent of paper samples

	Dielectric permittivity	Loss tangent
Photographic paper	2.35	0.044
Fabriano Copy 2	2.13	0.06
Watercolor paper	2.09	0.045
Corrugated paper	1.46	0.036
Raw paper	2.11	0.037
PM1	1.9	0.045
Momo 07	2.02	0.041

that requires a proper electromagnetic characterization in terms of surface conductivity σ . The technique selected to characterize the aluminum conductivity is based on a cylindrical cavity resonator at the frequency of 2.45 GHz, developed for the characterization of dielectric materials. The features of the empty cavity are well known in terms of dimensions, resonant frequency and unloaded quality factor. The last one in particular is strictly related to conductor losses. The experimental setup consist in two measurements of the cavity by employing a vector network analyzer (VNA). The first measurement provides the S parameters of the empty cavity, in order to determine the resonance frequency and quality factor Q . Then, the top and bottom walls of the cylindrical cavity are covered with the aluminum films. The S matrix is measured again and new cavity parameters are obtained. Fig. 48 shows the overlap of the measured transmission parameter S_{21} , with and without the aluminum films.

By means of the measured S parameters, the resonance frequency is obtained together with the -3dB bandwidth and the insertion loss. The unloaded quality factor of the cavity is calculated as

$$Q_{\text{unloaded}} = \frac{f_0}{BW_{-3dB}(1 - S_{21lin}(f_0))} \quad (25)$$

where f_0 is the resonance frequency, BW_{-3dB} is the -3dB bandwidth and $S_{21lin}(f_0)$ represents the insertion loss evaluated at the resonance frequency. To evaluate the conductivity of the aluminum foils, we need to separate the contribution of losses due to the top and bottom walls of cavity from the losses of the lateral wall. This is achieved by considering the expression of the unloaded quality factor

$$Q_{\text{unloaded}} = \left(\frac{2a\sqrt{\pi f \mu_0 \sigma_{lat}}}{d \eta_0 \chi \sigma_{lat}} + \frac{2\sqrt{\pi f \mu_0 \sigma_{par}}}{\eta_0 \chi \sigma_{par}} \right)^{-1} \quad (26)$$

where d is the height of the cavity and a the radius. σ_{lat} represents the surface conductivity of the lateral metallic wall, whereas σ_{par} stands for the surface conductivity of the top and bottom parallel walls. By

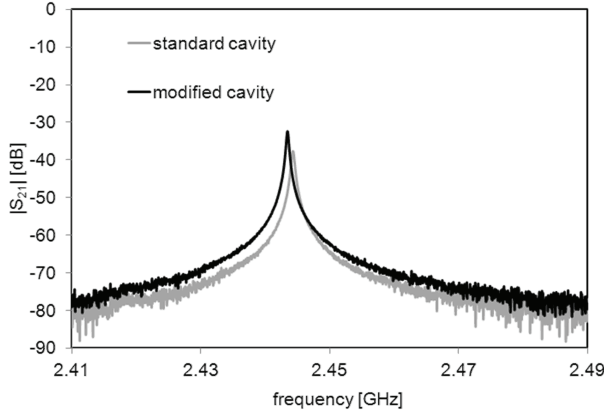


Figure 48: Measured $|S_{21}|$ of the cavity resonator.

employing equations (25) and (26) the conductivity of aluminum film can be achieved. However, in our case, both quality factors resulted approximately 5000, showing that the conductivity of the aluminum foils practically coincides with the conductivity of the solid metal walls of the cavity.

3.11.2 Design of paper-based transmission lines

In this section different types of planar interconnects on paper are analyzed, in order to evaluate the main characteristics of each structure in terms of size, bandwidth, losses and complexity of fabrication process. To this aim, a microstrip, a stripline, and different SIW transmission lines are considered. The electrical parameters of the substrate adopted in the simulations are dielectric permittivity $\epsilon_r = 2.85$, loss tangent $\tan \delta = 0.053$, and conductivity $\sigma_c = 1.5 \cdot 10^7$ S/m.

Microstrip

The first transmission line analyzed has been a microstrip: it was dimensioned in order to exhibit a characteristic impedance of 50Ω (Fig. 49a). The thickness of the substrate is 0.69 mm and therefore the width of the strip is 1.8 mm. Fig. 49b shows the propagation and the attenuation constants of the interconnect in the frequency band of interest. Since only the fundamental mode, which has no cut-off frequency, can propagate in the transmission line, the bandwidth of the structure is very broad. Concerning the losses, it results that they increase with frequency.

Stripline

The stripline was then considered. To obtain a characteristic impedance of 50Ω analyzed with a thickness $h = 0.69$ mm the width of the strip $w = 0.48$ mm (Fig. 50a). Fig. 50b shows the propagation and the attenuation constants of the interconnect in the frequency band of interest. The characteristics in terms of bandwidth are similar to the microstrip, while the losses are higher and the structure results very compact.

Substrate integrated waveguide

Compared to the standard planar transmission lines, SIW interconnects present a larger size and a limited operation bandwidth [39]. In fact, the single-mode frequency range covers one octave, like the standard rectangular waveguide, ranging from the cutoff frequency f_1 of the fundamental (quasi TE_{10}) mode to the cutoff frequency f_2 of the second (quasi TE_{20}) mode, corresponding to a bandwidth $f_2 - f_1 = f_1$. The considered SIW structure has a width $w = 36.3$ mm, metal via diameter $d = 1$ mm and longitudinal spacing $s = 2$ mm, corresponding to a cut-off frequency $f_1 = 2.48$ GHz (Fig. 51a). The substrate thickness is $h = 0.69$ mm. Fig. 51b shows the propagation and the attenuation constants of the interconnect in the frequency band of interest. As already discussed, the bandwidth of the SIW is around 2.5 GHz, which permits to cover the frequency band of interest (3.1-4.8 GHz).

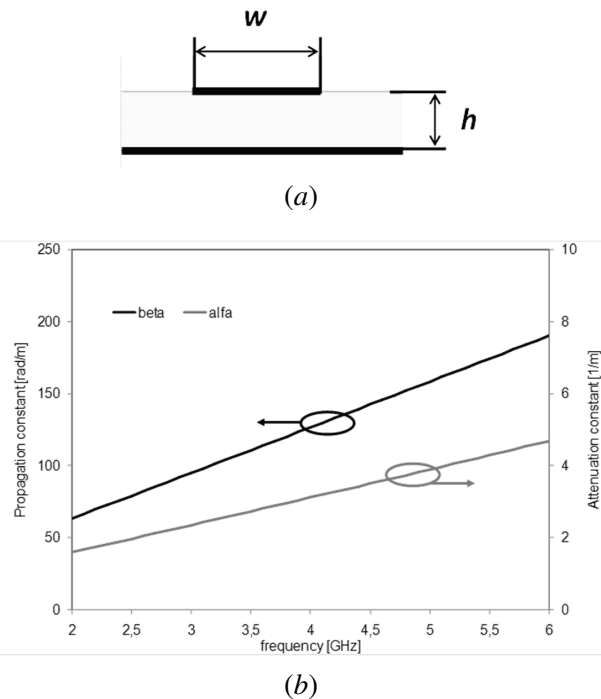


Figure 49: Microstrip line on paper: (a) geometry of the microstrip; (b) propagation and attenuation constants of the microstrip.

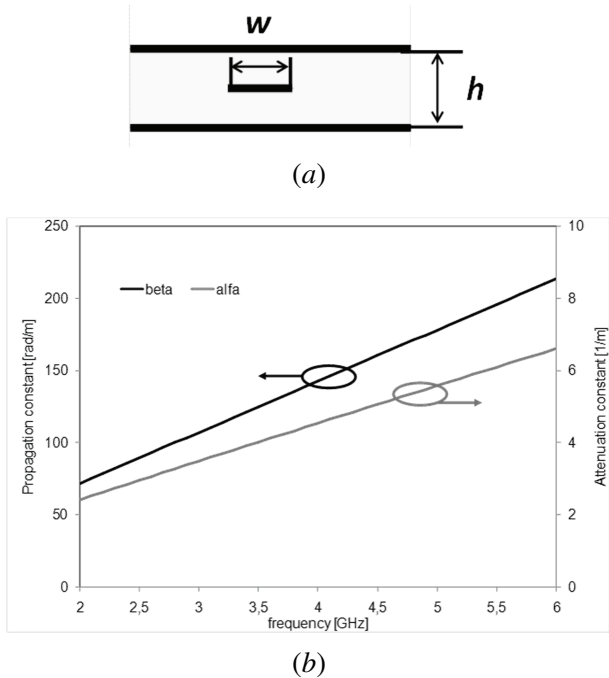


Figure 50: Stripline on paper: (a) geometry of the stripline; (b) propagation and attenuation constants of the stripline.

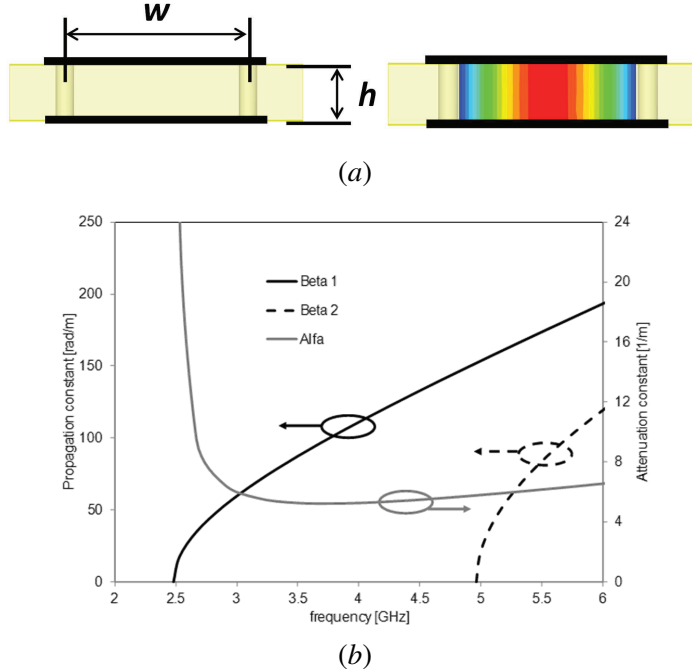


Figure 51: Substrate integrated waveguide interconnect on paper: (a) geometry and electric field pattern of the SIW; (b) propagation and attenuation constants of the SIW.

The losses in SIW structure are high near the cutoff frequency and decrease when increasing the frequency, like in a classical rectangular waveguide. In particular, SIW components are affected by three different mechanisms of losses: the conductive loss (α_C), the dielectric loss (α_D), and the radiation loss (α_R) [40,41]. The first two mechanisms can be encountered also in the analysis of the standard rectangular waveguide filled with a dielectric medium, while the radiation loss it typical of the SIW structure, because of the presence of gaps between the via holes. The total losses of SIW circuit can be approximated as the sum of these three components.

The conductor loss is due to the finite conductivity of the metallic boundaries, namely the top and bottom layers and the lateral rows of metal posts. The height of the substrate plays an important role in the minimization of the conductor loss. In fact, increasing the substrate thickness reduces the conductor loss, since the electric current density on the top and bottom ground planes decreases. Therefore, the power dissipated by Joule effect in these sheets is reduced.

The dielectric loss is due to the electrical characteristics of the substrate material (loss tangent), which defines the level of the dissipated power. While design rules can be applied to reduce the conductor loss, the dielectric one cannot be decreased through variations of the SIW geometry.

Finally, the radiation losses are caused by the gaps between the metallized holes, which determine the leakage of the electromagnetic field. In order to limit this loss, the via holes have to be as close as possible to each other. In particular, the radiation leakage can be considered negligible if $s < 2.5d$, and, taking into account the fabrication constraints, a good solution is to fix $s = 2d$. In the case of the considered SIW on paper, the dielectric loss represents the major contribution of loss (Fig. 52a). Fig. 52a shows the effect of the substrate thickness on the total losses of the SIW structure. Due to the limited contribution of conductor loss, the thickness plays a marginal role.

Folded substrate integrated waveguide

The substrate integrated folded waveguide (SIFW) consists of a two layers structure which permits to reduce the size of the standard SIW while keeping similar propagation characteristics [42]. This new transmission line configuration is composed of two substrate layers with a metallic septum in between: the top and bottom sides of the structure are metallized and two rows of posts define the lateral walls (Fig.

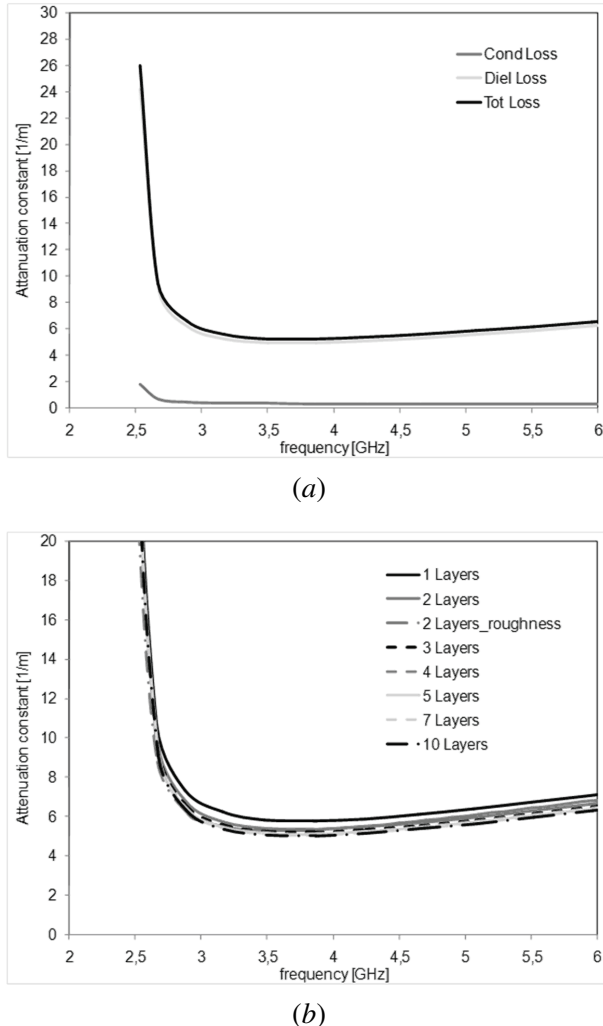


Figure 52: Substrate integrated waveguide interconnect on paper: (a) attenuation constant versus frequency due to different contributions of the SIW; (b) attenuation constant versus frequency in an SIW interconnect for different values of substrate thickness.

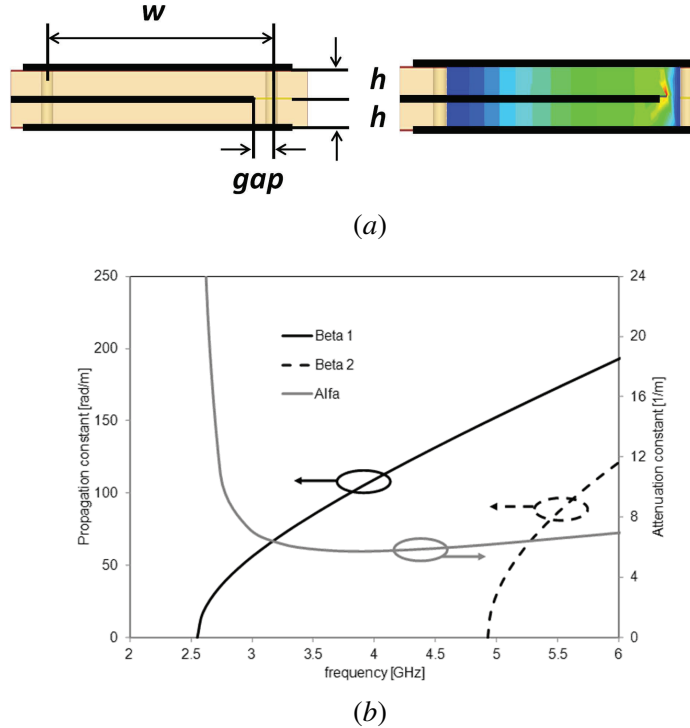


Figure 53: Folded substrate integrated waveguide interconnect on paper: (a) geometry and electric field pattern of the folded SIW; (b) propagation and attenuation constants of the folded SIW.

53a).

By adopting the SIFW structure, a reduction of the width of the waveguide w of a factor two or more can be achieved, depending of the width of the gap gap and the thickness h of the substrate. In our design $h = 0.46$ mm, $gap = 1.3$ mm, and $w = 18.6$ mm.

As shown in Fig. 53b, the SIFW presents a bandwidth slightly narrower than the standard SIW transmission line. In fact, while the cutoff frequency of the TE_{20} remains unchanged on varying of the width of the gap, the cutoff frequency of the fundamental mode increases when the value of the gap increases. Therefore taking into account the size and the bandwidth of the SIFW, the gap should be as small as possible, compatibly with the manufactory constraints, to improve the geometric and electric properties of the component. On the other hand, the presence of a small gap tends to increase losses. In general, the SIFW exhibits larger losses than the corresponding conventional SIW, due to the large amplitude of the electric field in the gap region. Consequently, the loss increase is small for broad gaps and becomes more significant if the gap width is very small. Moreover, extremely narrow gaps make the fabrication process more critical. For these reasons, the gap size was not minimized.

Double folded substrate integrated waveguide

Another configuration of the SIFW was considered: the multilayer substrate integrated folded waveguide [43]. The structure consists of four substrate layers with metallic septa properly located between them. With this configuration, a reduction of a factor four can be easily achieved (Fig. 54a).

The most important enhancement of the multilayer SIFW is the increase in the single-modal bandwidth (Fig. 54b). By properly selecting the width of the four metallic layers, the single-mode bandwidth can be increased more than a factor four. This configuration, however, does not permit to minimize the size of the multilayer SIFW. In our case, $h = 0.46$ mm, $gap = 1.3$ mm, and $w = 11.5$ mm.

Since this structure requires internal vias, the fabrication process is more complex than in the standard SIFW, but it allows to reduce the footprint of the component and to improve its performance in terms of bandwidth.

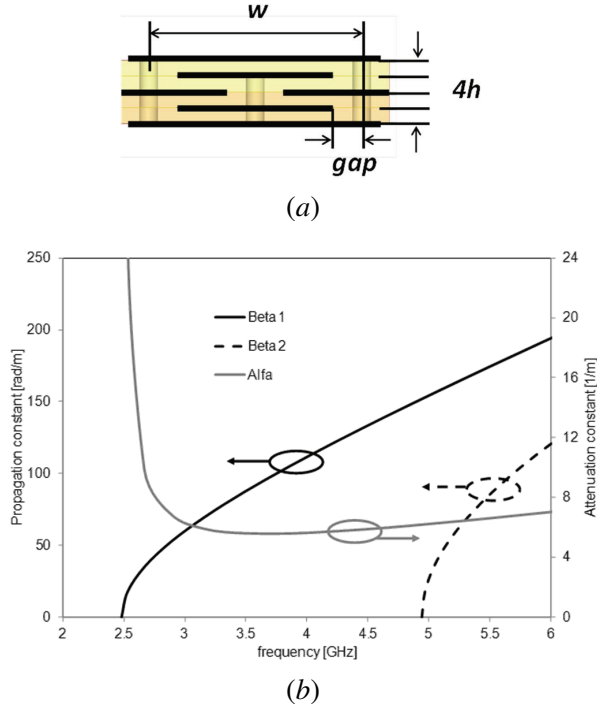


Figure 54: Double folded substrate integrated waveguide interconnect on paper: (a) geometry of the double folded SIW; (b) propagation and attenuation constants of the double folded SIW.

A simpler configuration is shown in Fig. 55a. It permits to achieve the same reduction of the size of the previous configuration but not to increase the bandwidth of the transmission line. In Fig. 55b the attenuation and propagation constants of the modified SIFW with $h = 0.46$ mm, $gap = 1.3$ mm, and $w = 10.3$ mm, are reported.

Half-mode substrate integrated waveguide

Another solution that can be adopted to reduce the dimension of SIW components is the half-mode substrate integrated waveguide (HMSIW) [44]. The structure is based on the conventional SIW with half of the structure removed along the symmetry plane, as shown in Fig. 56a.

Because the symmetry plane is a virtual magnetic wall for the fundamental mode, the field distribution of the TE_{10} mode is not spoiled and the propagation characteristics of the SIW are maintained. On the other hand, the second mode supported by the HMSIW is not the TE_{20} but the TE_{30} : this behavior is the effect of the geometry of the structure that permits only the propagation of the even modes. The single-mode bandwidth is therefore broader than in a classical SIW (Fig. 56b). In order to design the HMSIW the optimization of the width of waveguide w is suggested. In fact, although the cutoff frequency should be the same of a SIW structure with double width, because of the fringing field effect, a slightly correction of w is needed. In our design $h = 0.69$ mm and $w = 17.9$ mm.

Losses in HMSIW are equivalent to the losses in conventional SIW, except in the narrow frequency band close to the cutoff frequency, where a significant radiation leakage is identified.

Half-mode folded substrate integrated waveguide

HMSIW and SIFW can be combined to obtain the half-mode folded substrate integrated waveguide (Fig. 57a) This configuration further improves the characteristics of the substrate integrated waveguide, as shown in Fig. 57b. The following dimensions were adopted: $h = 0.69$ mm, $gap = 1.3$ mm, $w = 9.7$ mm.

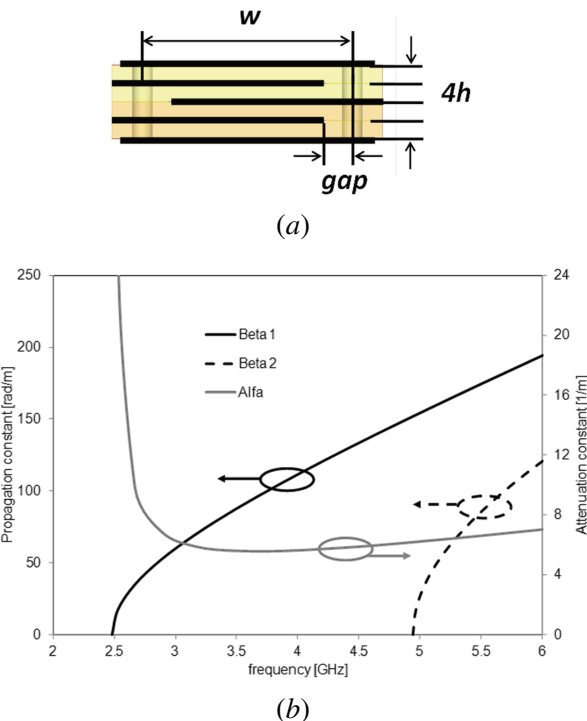


Figure 55: Simpler version of the double folded substrate integrated waveguide interconnect on paper: (a) geometry of the double folded SIW; (b) propagation and attenuation constants of the double folded SIW.

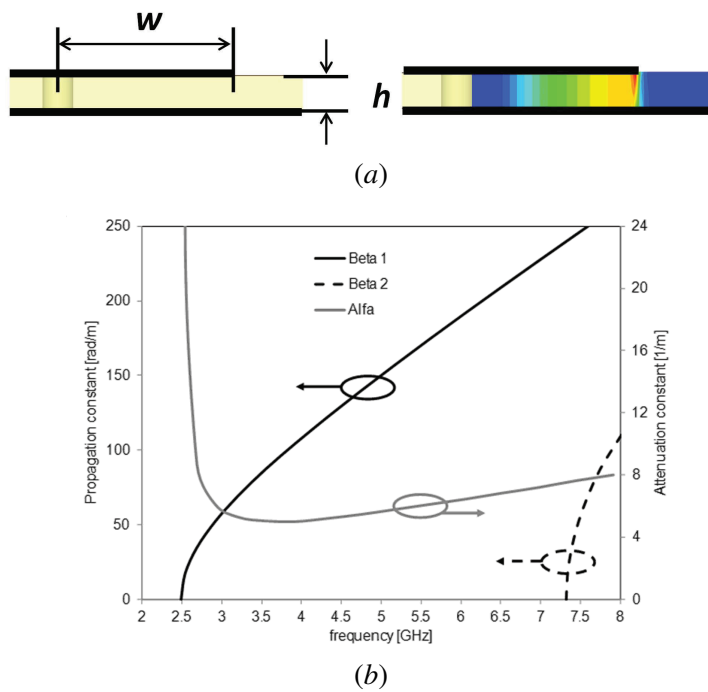


Figure 56: Half-mode substrate integrated waveguide interconnect on paper: (a) geometry and electric field pattern of the half-mode SIW; (b) propagation and attenuation constants of the half-mode SIW.

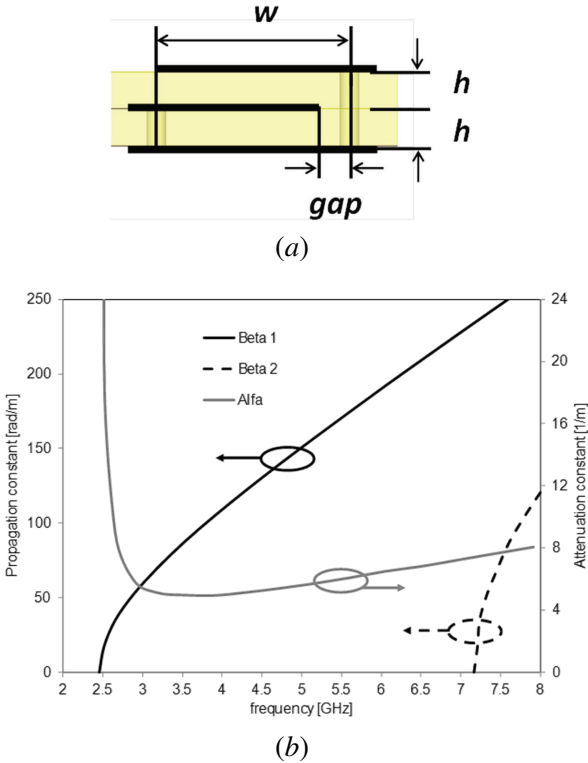


Figure 57: Half-mode folded substrate integrated waveguide interconnect on paper: (a) geometry and electric field pattern of the half-mode folded SIW; (b) propagation and attenuation constants of the half-mode folded SIW.

3.11.3 Design and fabrication of paper-based SIW interconnects

Once the electromagnetic properties of different paper-based substrates have been deeply investigated, the next step is the design, fabrication and measurement of paper-based SIW interconnects. Within the different considered substrates, the photographic paper is chosen as the ideal substrate for prototyping the first set of SIW interconnects. As mentioned above, the thickness of a single sheet of photographic paper is only 230 microns. In order to increase the thickness of the substrate, a stack of three sheets of paper has been adopted. The layers have been glued together with a film of PVP glue, achieving an overall thickness of 690 microns. The metallizations have been realized using two aluminum films, pasted on the top and the bottom of the substrate by using epoxy glue. The substrate is then pressed and heated in an oven at 70°C for 4 hours. During this warm-up process the epoxy glue crystallizes, becoming solid and stiff. This kind of glue is necessary because the layout pattern is manufactured by using a CNC milling machine.

The design of the SIW interconnects is based on the commercial software Ansys HFSS. The considered substrate thickness is 690 microns, the dielectric permittivity is $\epsilon_r = 2.43$ and a loss tangent is $\tan \delta = 0.036$ (these values were carried out using the ring resonator technique, described above). The width of the SIW is set to 39 mm in order to achieve a cut-off frequency of 2.48 GHz. By this way, the standard single-mode bandwidth starts at 3.1 GHz, corresponding to the lower frequency of the UWB commercial bandwidth. The cut-off frequency of the second mode is then 4.96 GHz. With the aim of measure this device, two microstrip-to-SIW tapers have been designed in order to get a return loss lower than -15 dB throughout the entire frequency band and to achieve a 50 Ohm input impedance.

Once the design has been optimized, it is exported through another commercial software to draw the circuit layout. Finally the project is saved in Gerber format and processed through the milling machine software. The circuit is then drilled and milled. In addition, the holes are filled with a conductive paste and the circuit is pressed and heated again for 2 hours at 100°C. The results of the manufactured process

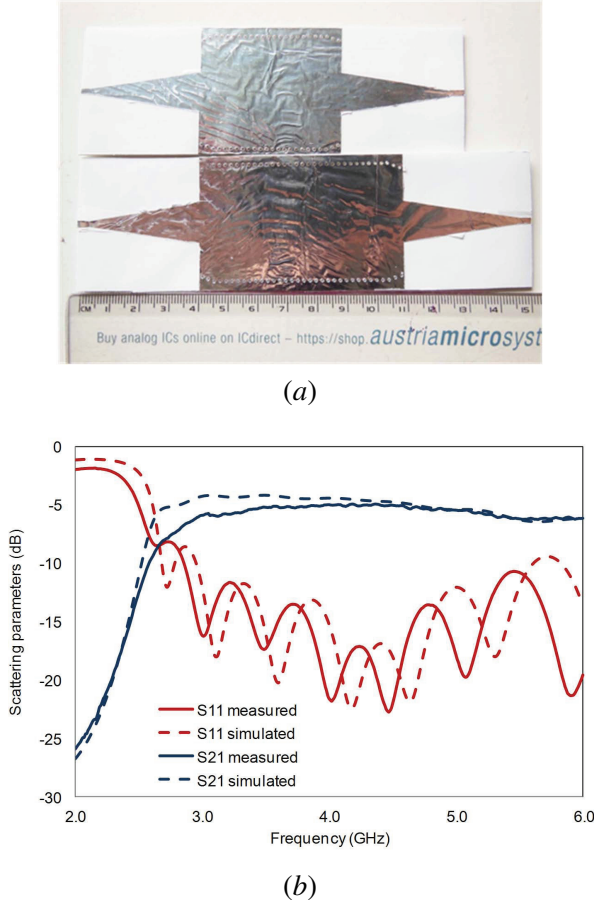


Figure 58: Prototype of the SIW interconnect: (a) photograph of the prototype; (b) simulation and measurement of the scattering parameters.

of two SIW lines are shown in Fig. 58a. The measurements are performed with the VNA Anritsu 37347C from 2 GHz to 6 GHz. In Fig. 58b, the simulated and measured scattering parameters ($|S_{11}|$ and $|S_{21}|$) measured superposed on the simulated ones of the long SIW transmission line.

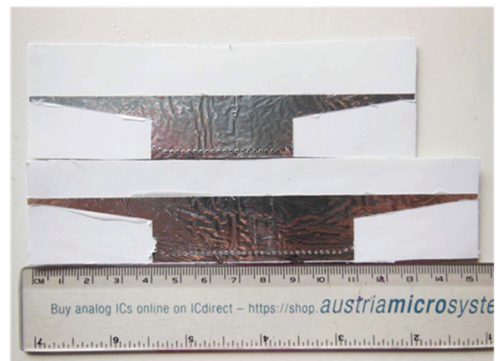
The results shown in Fig. 58b show a good agreement between simulation and measurement. In particular, the return loss is well better than 10 dB in the entire single-mode frequency band and the measured insertion loss well agrees with the simulation. Moreover, the cut-off frequency measured is only slightly different from the simulated one.

Finally, another type of SIW interconnect was designed and manufactured. By using the same substrate based on three sheets of photographic paper, an half-mode SIW was designed along with the microstrip-to-HMSIW transitions. A prototype was manufactured by adopting the same process as the standard SIW. As in the case of the SIW interconnect, two half-mode SIW structures have been designed and manufactured. A picture of the prototypes is shown in Fig. 59a). Fig. 59b shows the good agreement between the simulated and measured scattering parameters.

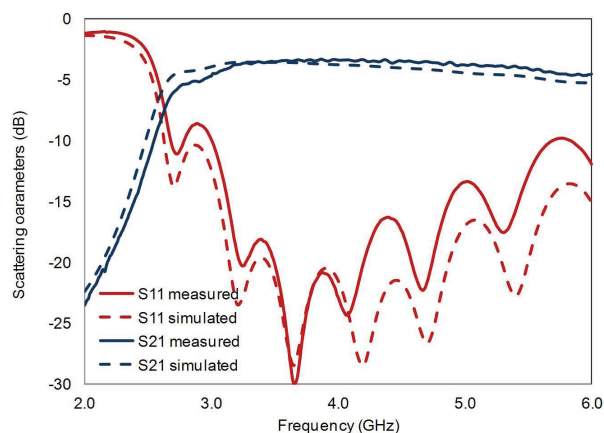
3.12 Localization and tracking algorithm

The purpose of the localization and tracking algorithm is to provide an estimate of tags' position starting from TOA and/or AOA measurements provided by the receiver.

We now describe the Bayesian filtering techniques for localization, tracking, and ordering of tags. A case study with a stream of objects moving on a conveyor belt is presented and preliminary results on their order-of-arrival estimation are shown.



(a)



(b)

Figure 59: Prototype of the half-mode SIW interconnect: (a) photograph of the prototype; (b) simulation and measurement of the scattering parameters.

3.12.1 Bayesian Filtering

The tracking process involves the estimation of position and velocity of the dynamic target. A dynamic system can be fully described by two equations: the evolution equation, which relates the current state vector to the prior state vector, and the stochastic measurement equation, which relates the observation data to the current state vector as

$$\mathbf{p}_n = f_n(\mathbf{p}_{n-1}, \mathbf{v}_{n-1}) \quad (27)$$

$$\mathbf{z}_n = h_n(\mathbf{p}_n, \mathbf{u}_n) \quad (28)$$

where \mathbf{p}_n is the state vector at time t_n , \mathbf{v}_n is the process noise vector, \mathbf{z}_n is the measurements collected by sensors at time t_n , and \mathbf{u}_n is the sensor noise. In general, these two equations are nonlinear. The state estimator, called filter, represent the algorithm for the recursive estimation of the state $\hat{\mathbf{p}}_n$ from the measurements $\mathbf{z}_{(1:n)}$.

The Bayesian filters rely on the quantification of the posterior probability density function (pdf), the positional belief, and require the pdf of the current state conditional on the previous state, and the pdf of the observation state conditional on the current state as [45]

$$p(\mathbf{p}_n | \mathbf{z}_1, \dots, \mathbf{z}_n) = \frac{p(\mathbf{z}_n | \mathbf{p}_n) p(\mathbf{p}_n | \mathbf{z}_1, \dots, \mathbf{z}_{n-1})}{p(\mathbf{z}_n | \mathbf{z}_{n-1})} = C p(\mathbf{z}_n | \mathbf{p}_n) p(\mathbf{p}_n | \mathbf{z}_1, \dots, \mathbf{z}_{n-1}) \quad (29)$$

where C is the normalization constant. Different implementations of the posterior pdf lead to different state estimators. Here, we focus on Kalman Filter and Particle Filter, which are the widest adopted solutions.

3.12.1.1 Kalman Filter and Extended Kalman Filter

When the evolution equation and the stochastic measurement equation are linear, and noises are Gaussian distributed $\mathbf{v}_n \sim \mathcal{N}(0, \mathbf{Q}_n)$ and $\mathbf{u}_n \sim \mathcal{N}(0, \mathbf{R}_n)$ then the equations reduce to

$$\mathbf{p}_n = \mathbf{F}_n \mathbf{p}_{n-1} + \mathbf{v}_{n-1} \quad (30)$$

$$\mathbf{z}_n = \mathbf{H}_n \mathbf{p}_n + \mathbf{u}_n \quad (31)$$

where \mathbf{F}_n and \mathbf{H}_n are assumed known and named state evolution and measurement matrix, respectively. The Kalman Filter represents the mathematical solution of this problem, where the prediction phase is given by

$$\begin{aligned} \hat{\mathbf{p}}_{n|n-1} &= \mathbf{F}_n \hat{\mathbf{p}}_{n-1|n-1} \\ \mathbf{P}_{n|n-1} &= \mathbf{F}_n \mathbf{P}_{n-1|n-1} \mathbf{F}_n^T + \mathbf{Q}_n \end{aligned} \quad (32)$$

where $\hat{\mathbf{p}}_{n|n-1}$ and $\mathbf{P}_{n|n-1}$ are the a posteriori state and covariance estimates at time n given observations up to n . The update phase is given by

$$\begin{aligned} \hat{\mathbf{p}}_{n-1|n-1} &= \hat{\mathbf{p}}_{n|n-1} + \mathbf{K}_n (\mathbf{z}_n - \mathbf{H}_n \hat{\mathbf{p}}_{n|n-1}) \\ \mathbf{P}_{n-1|n-1} &= (\mathbf{I} - \mathbf{K}_n \mathbf{H}_n) \mathbf{P}_{n|n-1} \end{aligned} \quad (33)$$

where \mathbf{K}_n is called Kalman gain and is given by

$$\mathbf{K}_n = \mathbf{P}_{n|n-1} \mathbf{H}_n^T (\mathbf{H}_n \mathbf{P}_{n|n-1} \mathbf{H}_n^T + \mathbf{R}_n)^{-1}. \quad (34)$$

The Extended Kalman Filter is a version of the Kalman filter that allows non-linear evolution and stochastic measurement equations. In particular, when $f_n(\cdot)$ and $h_n(\cdot)$ are non-linear functions, the state evolution and measurement matrix are given by

$$\begin{aligned}\mathbf{F}_n &= \frac{\partial f}{\partial \mathbf{p}} \Big|_{\hat{\mathbf{p}}_{n|n}} \\ \mathbf{H}_n &= \frac{\partial h}{\partial \mathbf{p}} \Big|_{\hat{\mathbf{p}}_{n|n-1}}.\end{aligned}\quad (35)$$

3.12.1.2 Particle Filter

The key idea of particle filters (PFs) is to represent the posterior distribution (the belief), by a set of random samples (particles) with associated weights as

$$p(\mathbf{p}_n | \mathbf{z}_1, \dots, \mathbf{z}_n) \approx \sum_{i=1}^{N_{\text{par}}} w_{n,i} \delta(\mathbf{p}_n - \mathbf{s}_{n,i}) \quad (36)$$

where N_{par} is the number of particles, $\delta(\cdot)$ is the Delta function, $w_{n,i} \geq 0 \forall n, i$ is the weight for particle i at time index n , and $\sum_{i=1}^{N_{\text{par}}} w_{n,i} = 1$. The weights are chosen, for example, using the principle of importance sampling in which a distribution of samples is considered with more dense samples where it is more probable that the object is located. In PF algorithms, the main important recursive steps for evaluating the i th particle can be summarized as follow

$$\mathbf{s}_{n,i} \sim p(\mathbf{p}_n | \mathbf{p}_{n-1}) \quad \text{mobility model} \quad (37)$$

$$w_{n,i} = w_{n-1,i} p(\mathbf{z}_n | \mathbf{s}_{n,i}) \quad \text{perception model}. \quad (38)$$

For Gaussian mobility model, the (37) becomes

$$p(\mathbf{p}_n | \mathbf{p}_{n-1}) = \frac{1}{\sqrt{2\pi}\sigma_m} e^{-\frac{\|\mathbf{p}_n - \mu_n\|^2}{2\sigma_m^2}} \quad (39)$$

where the standard deviation σ_m represents the uncertainty on the target movement, and the mean μ_n depends on \mathbf{p}_{n-1} and intra-node measurements.

We consider independent observations, thus the perception model in (38) is given by

$$p(\mathbf{z}_n | \mathbf{p}_n) = \prod_{i=1}^N p(\mathbf{z}_{n,i} | \mathbf{p}_n) \quad (40)$$

where $\mathbf{z}_{n,i}$ is the i th measurement at time index n . We assume a perception model with Gaussian distribution. For example, if the measurement $\mathbf{z}_{n,i}$ is a distance measurement between the i th reader and the tracked tag, the perception model is given by

$$p(\mathbf{z}_{n,i} | \mathbf{p}_n) = \frac{1}{\sqrt{2\pi}\sigma_p} e^{-\frac{(\mathbf{z}_{n,i} - \|\mathbf{p}_n - \mathbf{r}_i\|)^2}{2\sigma_p^2}}. \quad (41)$$

where \mathbf{r}_i is the position of the i th reader. The standard deviation σ_p depends on both the accuracy of localization technology and signal propagation conditions.

3.12.2 Case Study: Order of Arrival Estimation via Bayesian Tracking

We now present the framework, performance metrics, tracking algorithm implementation, and preliminary results for the order-of-arrival estimation of a stream of objects.

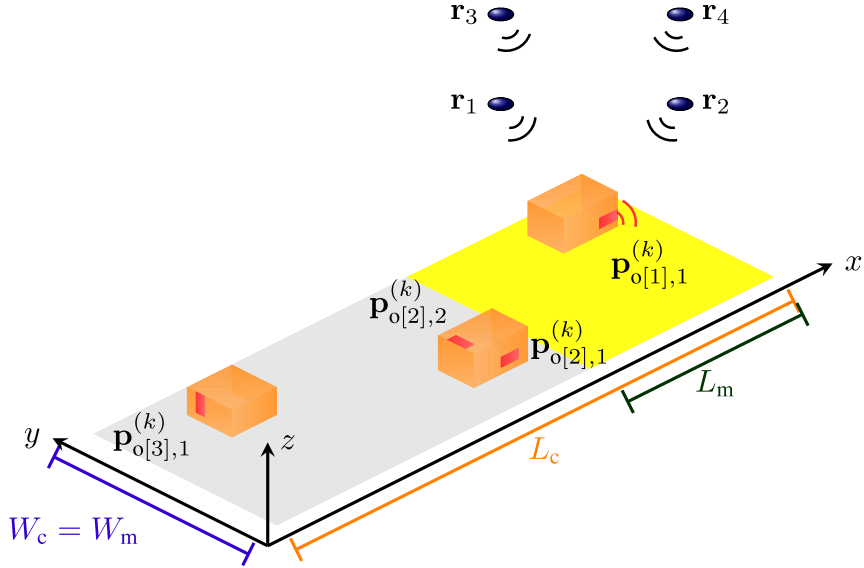


Figure 60: Conveyor belt scenario, the OOA of the objects with respect to the monitored area is indicated by the vector \mathbf{o} .

3.12.2.1 Conveyor Belt Scenario

We consider a stream of N_o objects with index set \mathcal{O} laying on a conveyor belt with length L_c , width W_c , and moving with a known speed vector $\mathbf{v} \in \mathbb{R}^3$ according to a Cartesian coordinate system (see, e.g., Fig. 60). We are interested in detecting, identifying, and estimating the OOA of the objects within a monitored area A_m of length L_m and width W_m of the conveyor belt (i.e., a sorting process). The OOA estimation is determined by the order with which objects leave the monitored area. In particular, \mathbf{o} is the vector representing the true OOA, therefore $\mathbf{o}[k] = l$ indicates that the l th object is the k th to cross the monitored area.

Each object is equipped with N_{to} tags. In particular, the j th tag on the i th object at time index k is in position $\mathbf{p}_{ij}^{(k)} = [x_{ij}^{(k)}, y_{ij}^{(k)}, z_{ij}^{(k)}] \in \mathbb{R}^3$ with respect to the reference system in Fig. 60, $i = 1, \dots, N_o$ and $j = 1, \dots, N_{\text{to}}$.⁷ Time indices correspond to the instants in which measurements are taken by the readers. We consider N_{read} readers, with index set \mathcal{R} . The r th reader is in known position \mathbf{r}_r and transmits signals to detect, identify, and localize the tags in the monitored area. Specifically, in the example shown in Fig. 60, $N_{\text{read}} = 4$, $\mathbf{v} = [v_c, 0, 0]$, $x_{ij}^{(k)} = x_{ij}^{(1)} + k v_c T_u$, $y_{ij}^{(k)} = y_{ij}^{(1)}$ and $z_{ij}^{(k)} = z_{ij}^{(1)}$, where v_c is the constant speed of the conveyor belt along the \vec{x} direction and T_u is the interrogation repetition time (i.e., the difference between two consecutive tag position estimations).

A position estimate $\hat{\mathbf{p}}_{ij}^{(k)}$ is determined for each time index $k \in \mathcal{K}_{ij}$, where \mathcal{K}_{ij} is the set of time indices in which the j th tag of the i th object is detected and identified after that a measurement is taken. The maximum localization update rate is $R_u = 1/T_u$. Let $\mathcal{D} \subseteq \mathcal{O}$ be the set of objects that have been detected at the end of the process. An object is considered detected if at least one of its tags is detected by one reader during the time it is within the monitored area. We define $\mathbf{o}_{\mathcal{D}}$ as the OOA vector conditional on detection, which represents the relative OOA among the objects in \mathcal{D} . Starting from the tag position estimates, the OOA vector $\hat{\mathbf{o}}$ is estimated by considering as object position the tag's position which is greatest with respect to the conveyor direction.

Let $\hat{\mathbf{k}}_o$, $i = 1, \dots, N_o$, be the vector of the greatest time indices at which each object has been detected and localized within the monitored area, i.e., $\hat{\mathbf{k}}_o[1] = n$ if n is the last time index at which the object

⁷Note that the position of each tag at time index k depends on the first position $\mathbf{p}_{ij}^{(1)}$ and varies according to the conveyor belt speed.

indexed by 1 has been detected. This vector is determined based on the tag position estimates

$$\hat{\mathbf{k}}_o[i] = \max\{k \in \mathcal{K}_{ij} : [\hat{x}_{ij}^{(k)}, \hat{y}_{ij}^{(k)}] \in \mathcal{A}_m, j = 1, \dots, N_{to}\}. \quad (42)$$

The OOA vector is estimated by sorting the vector $\hat{\mathbf{k}}_o$ as

$$\hat{\mathbf{o}}[h] = \underset{i \text{ s.t. } \hat{\mathbf{k}}_o[i]=k_h}{\operatorname{argmax}} \left\{ \hat{\mathbf{p}}_{ij}^{(k_h)} \cdot \mathbf{v} : j = 1, \dots, N_{to} \right\} \quad (43)$$

where $k_h = \min \left\{ \hat{\mathbf{k}}_o[i] : i \notin \{\hat{\mathbf{o}}[1], \dots, \hat{\mathbf{o}}[h-1]\} \right\}$ and $\mathbf{a} \cdot \mathbf{b}$ is the scalar product between vectors \mathbf{a} and \mathbf{b} . Note that the length of the vector $\hat{\mathbf{o}}$ is equal to the cardinality of the set \mathcal{D} .

3.12.2.2 Particle Filter Implementation

Tracking algorithm infers the tag position $\mathbf{p}_{ij}^{(k)}$ (i.e., the state vector) at each time index k from a set of ranging estimates (i.e., observations), a mobility model (i.e., relation between the current and the prior state vectors), and the perception model (i.e., relation between the observations and the current state vector). Following a Bayesian approach, the position estimate $\hat{\mathbf{p}}_{ij}^{(k)}$ is determined as the value that maximizes the position belief $b(\mathbf{p}) = p(\mathbf{p} | \hat{\tau}_{ij}^{(1:k)})$, which is the posterior distribution of the state vector given the set of observations $\hat{\tau}_{ij}^{(1:k)} \triangleq \{\hat{\tau}_{ij,r}^{(h)} \text{ s.t. } r \in \mathcal{R}, h = 1, 2, \dots, k\}$. In particular, at each time k , $\hat{\tau}_{ij}^{(1:k)}$ is the vector of RTT estimates and $\hat{\tau}_{ij,r}^{(1:k)}$ is the output of the energy detector at time k if the r th receiver detected and identified the target. Among the possible implementations of Bayesian algorithms, we consider the PF algorithm, which can outperform extended Kalman filter (EKF) in non-Gaussian noisy observations.⁸ In particular, the position belief at time k is represented by a set of N_{par} random samples (particles) at $\{\mathbf{s}_s^{(k)}\}$, with $s = 1, 2, \dots, N_{par}$. Mobility and perception models are used to predict, update, and resample the position belief at each k . In particular, a Gaussian mobility model is given by

$$p(\mathbf{s}_s^{(k)} | \mathbf{s}_s^{(k-1)}) = \frac{1}{\sqrt{2\pi}\sigma_{m,k}} e^{-\frac{\|\mathbf{s}_s^{(k)} - \hat{\mu}_k^{(n)}\|^2}{2\sigma_{m,k}^2}} \quad (44)$$

where $\sigma_{m,k}^2$ depends on the mobility of the target and $\hat{\mu}_n^{(k)} = \mathbf{s}_s^{(k-1)} + \mathbf{v} T_u$, where \mathbf{v} is the conveyor speed vector that is assumed known. A perception model for particles with independent observations, is given by

$$p(\hat{\tau}_{ij}^{(k)} | \mathbf{s}_s^{(k)}) = \prod_{r \in \mathcal{R}} \frac{1}{\sqrt{2\pi}\sigma_{p,k}} e^{-\frac{[\hat{\tau}_{ij,r}^{(k)} c/2 - \|\mathbf{r}_r - \mathbf{s}_s^{(k)}\|]^2}{2\sigma_{p,k}^2}} \quad (45)$$

where $\sigma_{p,k}^2$ depends on the ranging techniques and the propagation conditions.

3.12.2.3 Preliminary Results

We consider an UHF-UWB RFID system composed of 4 readers located on the edge of a monitored area of length $L_m = 2\text{ m}$ and width $W_m = 1.5\text{ m}$, with height 1.5 m with respect to the z axes, as shown in Fig. 60. We consider streams of $|\mathcal{O}^{(n)}| = N_o = 20$ with $n = 1, 2, \dots, N$ objects, where n indicates the n th Monte-Carlo trial and $N = 100$. Objects have parallelepiped shape with two possible dimensions described by the following edge lengths: a) 0.45 m , 0.22 m , and 0.41 m or b) 0.58 m , 0.36 m , and 0.86 m . Each object

⁸ Note that, in general, the set of observations have a non-Gaussian distribution due to multipath and clutter residual.

is equipped with a number of tags $N_{\text{to}} = 1, 2, \dots, 5$; at most one tag per face and no tags on the bottom face. At time index $k = 0$, each object is at a random position within the conveyor belt and the bottom face laying on the conveyor is chosen randomly. Tags are at a uniformly distributed random positions on object faces. To preserve the time resolvability of signals correspondent to different objects, a minimum Euclidean distance Δ_L is required between two tags attached to two different objects. Results are obtained with $\Delta_L = 0.3, 0.5$, and 0.8 m. The conveyor belt has length $L_c = 50\Delta_L$ m to preserve a certain density of objects per meter, and $W_c = W_m$. The conveyor speed vector is $\mathbf{v} = [v_c, 0, 0]$ and it is assumed known with $v_c = 1$ m/s. The same transmitting and receiving UWB antenna is considered for both tags and readers: a 3D simulated radiation pattern of a dipole antenna attached to a reflector has been included in simulation. Frequency selectivity is not considered and we assume the radiation pattern equal to its value at the central frequency $f_c = 4$ GHz. Reader antennas presents a maximum gain of $G_r(f_c, \Theta_r^{(\max)}) = 5.35$ dBi while tag antennas are such that the maximum value of $G_t(f_c, \Theta_t^{(\max)})/L_{\text{tag}} = 3$. Reader antennas are set to have maximum gain toward the center of the monitored area, while the tag antennas have maximum gain towards the direction orthogonal to the object face to which the tag is attached. Wireless propagation and ranging errors are modelled based on geometric visibility. In particular, for a given reader, each tag is assumed undetected when it is in NLOS condition with respect to the reader (i.e., another object obstruct the reader-tag signal path) or when it is in LOS condition with the reader but signal is received with $P_{ij}^{(k)} \leq P_{\text{th}}$, where P_{th} is a given threshold. In particular, we set P_{th} as the received power when a tag is at a distance of 6 m, antennas are oriented in the direction of the maximum gain and $N_s = 8192$.⁹ If a tag is detected, we assume a TOA estimation error uniformly distributed in $[-1, 1]$ ns.¹⁰ Results are obtained considering a maximum update rate $R_u = 5, 10$, and 15 Hz. The tracking algorithm is based on PF with $N_{\text{par}} = 100$, $\sigma_{p,k}^2 = 1$ for all k , and a value of $\sigma_{m,k}^2$ chosen such that the n th estimated particle at time k is within a circle centered at $\hat{\mu}_n^{(k)}$ of radius $|\hat{v}_k|T_L$.

Figure 61 shows the absolute OOA success rate for $R_u = 10$ Hz, various N_{to} , Δ_L , and N_s . It can be seen that, in each setting, R_a increases with N_s but with negligible improvement for $N_s > 2048$. Moreover, by increasing Δ_L the absolute OOA success rate becomes more sensitive to the number of tags per object. For example, varying N_{to} from 1 to 5 increases R_a from 0.03 to 0.08 when $\Delta_L = 0.3$ m, whereas it increases R_a from 0.02 to 0.20 when $\Delta_L = 0.8$ m. This is because the minimum distance between two tags attached to two different objects strongly limits the detection rate by increasing the number of NLOS conditions between readers and tags.

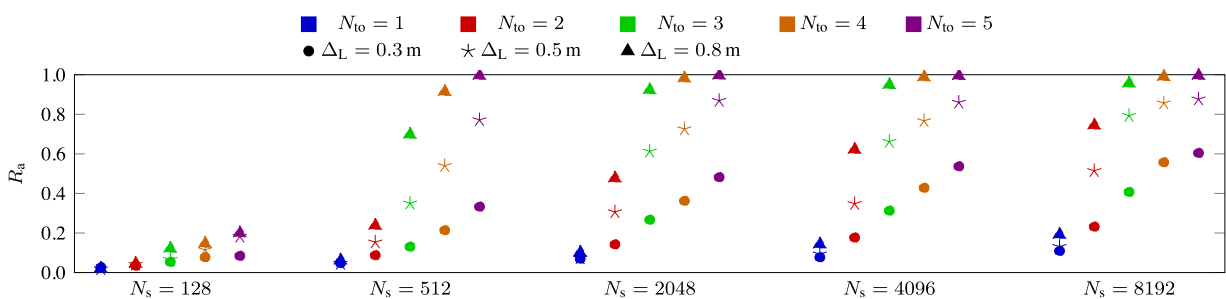


Figure 61: Absolute OOA success rate for $R_u = 10$ Hz and different values of N_s , Δ_L , and N_{to} .

Figure 62 shows the relative OOA success rate R_r and the object detection rate R_d for $\Delta_L = 0.5$ m, $N_{\text{to}} = 3$, and various Δ_L and N_s . It can be seen that the detection rate is more sensitive to the number of collected pulses than the update rate. For example, varying the update rate from $R_u = 5$ Hz to $R_u = 15$ changes R_d from 0.52 to 0.56 with $N_s = 128$, while it changes from 0.52 to 0.86 by increasing N_s from 128 to 512 when $R_u = 5$ Hz. Differently, the relative OOA success rate is very sensitive to the update rate, especially when the number of pulses is low. For example, varying the update rate from $R_u = 5$ Hz

⁹This distance has been measured considering these parameter within the European project SELECT (www.selectwireless.eu).

¹⁰This corresponds to an energy detector with $T_{\text{ED}} = 2$ ns.

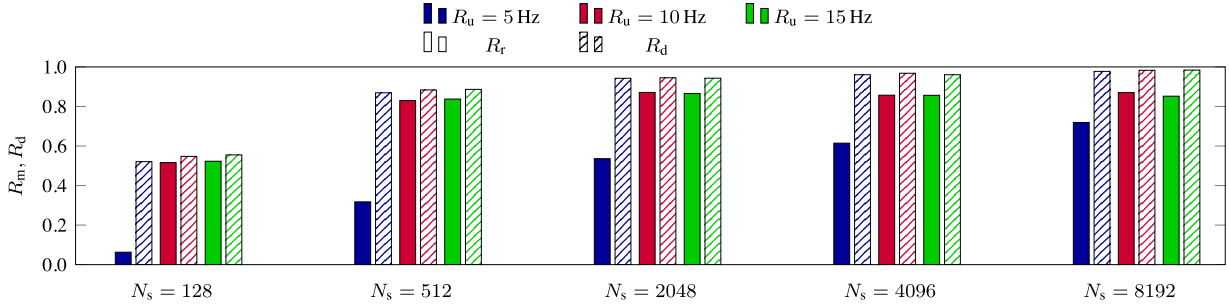


Figure 62: Relative OOA success rate and object detection rate for $N_{\text{to}} = 3$, $\Delta_L = 0.5 \text{ m}$, and different values of N_s and R_u .

$\Delta_L \setminus N_{\text{to}}$	R_m			R_r		
	0.3	0.5	0.8	0.3	0.5	0.8
1	0.53	0.43	0.32	0.42	0.55	0.68
2	0.29	0.16	0.08	0.57	0.80	0.91
3	0.15	0.06	0.01	0.65	0.87	0.98
4	0.08	0.02	0	0.66	0.91	0.99
5	0.05	0.01	0	0.69	0.91	1

Figure 63: Relative OOA success rate and misdetection rate for $N_s = 2048$ and different values of N_{to} and Δ_L .

to $R_u = 10$ changes R_r from 0.06 to 0.52. However, a floor is experienced for $R_u > 5 \text{ Hz}$. Note that this parameter and the floor is strictly related to the monitored area dimension and the speed of the conveyor. Similarly to Fig. 61 the effects of the number of collected pulses becomes negligible for $N_s > 2048$ for both R_a and R_m . This is due to the fact that the number of collected pulses influences the R_d more than the localization accuracy.

The table in Fig. 63 gives the relative OOA success rate R_r and misdetection rate R_m for $N_s = 2048$ and different values of N_{to} and Δ_L . Note that, even when the number of detected object is above the 95%, increasing the number of tag per object is less effective than increasing the distance between two tags Δ_L for the OOA performance. Moreover, increasing the number of tags above 3 has negligible effects on R_r , while it improves significantly the detection rate, especially when the distance between tags Δ_L is short.

3.13 Network Management Protocols

The proliferation of tags and dense RFID deployments poses a number of technical challenges for network protocols. Looking at the big picture, if multiple tags share a radio channel and they try to use it simultaneously, the reader cannot decode successfully the data transmitted by the colliding tags. This issue becomes more serious for an increasing number of active tags, and a MAC protocol is required to rule channel access and reduce collisions.

In this section, we present the most common approaches to channel access in RFID systems. First, we focus on CDMA-based schemes, showing the main features of pseudo-random and orthogonal codes. We also present a model for describing CDMA performance in presence of different channel conditions, and we comment preliminary results obtained from numerical simulations. Then, we introduce the standard ISO 18000-6C MAC and we propose a novel algorithm to adapt the UHF air interface parameters with the use of UWB ranging information.

3.13.1 Anti-collision schemes

Anti-collision schemes are distinguished in contention-free and contention-based multiple access. The first approach uses dedicated resources for packet transmissions. There are various multiplexing approaches: space division (SDMA), frequency division (FDMA), time division (TDMA), and code division (CDMA) multiple access. In SDMA, radio waves are distributed asymmetrically in the space around the reader using directional or smart antennas, and the angles can be exploited to distinguish tags in the read range. With FDMA, different tags use dedicated transmission frequencies, while dedicated time-slots are assigned to tags with a TDMA approach. Finally, the use of a spreading code to support multiple users within the same bandwidth is also called CDMA or spread-spectrum multiple access (SSMA) [46, 47]. In contention-based multiple access, tags compete for the medium and coordinate in a probabilistic way. The ISO/IEC 18000-6 [48] is the reference standard for RFID systems operating in the 860 MHz - 960 MHz UHF frequency range. It adopts and enhances the specifications of the EPCglobal protocol Class-1 Generation-2, which is used by most of the RFID manufacturers [10]. In particular, we focus on the Type C modality, which employs a framed slotted ALOHA collision arbitration with dynamic frame adaptation.

TDMA is the most popular contention-free multiplexing method for RFID applications: it ensures that each tag in range will be detected, given that the amount of time available is sufficient. If this condition is false, the system comes to hard decisions. Therefore, TDMA pushes a RFID network to its limits when a very high number of tags have to be scanned within a given time span.

In comparison to TDMA “hard decisions”, CDMA-based systems take instead “soft decisions” – within a spread-spectrum system, each user is assigned a unique spreading code which is used to modulate their data signals. The transmitted signals for all users are superimposed in time and in frequency, and each additionally RFID tag decreases the overall probability of detection of all tags [47, 49].

Thus, while spread-spectrum for single-user systems is spectrally inefficient, as it uses more bandwidth than the minimum needed to convey the information signal, spread-spectrum multiuser systems can support an equal or larger number of RFID tags in a given bandwidth than TDMA or FDMA.

3.13.2 Spread-spectrum sequences

In a general spread-spectrum system, each tag generates an unique code which is predictable and repetitive, although the code sequences appear to be random. The tag communicates with the reader changing its RF output status according to a combination of the data to be transmitted and the code. On the other side, the reader is able to decode the received signal using the knowledge of the original code.

Specifically, spreading codes are generated deterministically, often using a shift register with feedback logic to create a binary code sequence b of 1s and 0s, having a cyclical output with a maximum period of $2^n - 1$. The binary sequence, also called *chip* sequence, is used to amplitude modulate an antipodal square pulse train with pulses of duration T_c . The resulting spreading code $s_c(t)$ is a *sinc* function in the frequency domain, corresponding to the Fourier transform of a square pulse [50–52].

It is worth noting that, while spreading chip sequences must be generated deterministically, properties of random sequences are useful to gain insight into deterministic sequence design. Following [53], a deterministic sequence that has the balanced, run length, and shift properties as it grows asymptotically large is referred to as a *pseudo-random*, or pseudo-noise (PN), sequence.

Among all linear codes, spreading codes generated from maximal-length (ML) sequences, or *m-sequences*, have many desirable properties. Maximum-length sequences are a type of cyclic code generated and characterized by a generator polynomial, and their properties can be derived using algebraic coding theory. These sequences have the maximum period $N = 2^n - 1$ that can be generated by a shift register of length n – since the sequences are cyclic codes, any time shift of an m-sequence is itself an m-sequence. These sequences also have the property that the modulo-2 addition of a m-sequence, and a time shift of itself, results in a different m-sequence corresponding to a different time shift of the original sequence (shift-and-add property). Finally, the m-sequences have roughly the same number of 1s and 0s over a period: $2^{n-1} - 1$ zeros and 2^{n-1} ones. Moreover, maximal-linear codes have approximately

the same run-length property as random binary sequences. As a result, since m-sequences have the balanced, run length, and shift properties of random sequences, they belong to the class of pseudo-random sequences.

Gold codes represents the most common spreading codes in the family of PN ones. They have worse autocorrelation properties than maximal-length codes, but better cross-correlation properties if properly designed. The chip sequences associated with a Gold code are produced by the binary addition of two m-sequences. Thus, Gold codes are generated by the chip sequences associated with the modulo-2 addition of preferred pairs of m-sequences. These preferred pairs are chosen to obtain good cross-correlation in the resulting sequence. Since they inherit the balanced, run length, and shift properties of the component m-sequences, also Gold codes are pseudo-random sequences.

Kasami chip sequences have similar properties and are also derived from m-sequences. Moreover, Kasami codes have better cross-correlation properties than Gold ones. There are two different sets of Kasami chip sequences that are used to generate Kasami codes, the large set and the small set, and they are both suitable for CDMA applications.

The cross-correlation properties of different spreading codes determines the amount of interference between users – for synchronous users their signals arrive at the receiver aligned in time, while their signals arrive at the receiver with arbitrary relative delay τ when asynchronous.

A set of spreading codes with the cross-correlation of any two sequences $\rho_{ij}(\tau) = 0$, with $\tau = 0, i \neq j$, is called an *orthogonal code* set. Orthogonal codes are an alternative to PN codes, and are widely used in SSMA-based communication systems. For example, orthogonal Gold codes can be generated padding one “0” to the original Gold codes. In fact, 2^n orthogonal codes can be obtained by this simple zero padding, which brings their cross-correlation value from 1 to 0.

As an alternative, Walsh-Hadamard codes might be used. A nice property of this sequences is that they are orthogonal over a symbol time, with the cross-correlation of any two sequences equal to zero. Thus, synchronous users modulated with Walsh-Hadamard codes can be separated out at the receiver with no interference between them.

Orthogonal codes may seem an attractive replacement for PN codes, but the cross-correlation value is zero only when there is no offset between the codes. Hence, as discussed in the next Section 3.13.3, orthogonal codes have an application in perfectly synchronized environments while Gold codes or similar PN sequences are better suited for the asynchronous case.

3.13.3 Spread-spectrum model for RFID tags

As we outlined before, the spreading codes of two tags can be orthogonal, in which case users do not interfere with each other under ideal propagation conditions, or they can be non-orthogonal. In the latter case, users interfere with each other: if there is too much interference between users, the performance of all users degrades.

Multiuser spread-spectrum system performance also depends on whether the system is a downlink channel (one transmitter to many receivers) or an uplink channel (many transmitters to one receiver). The performance differences in uplink and downlink channels result from the fact that all downlink transmitted signals are typically synchronous, since they originate from the same transmitter.

A scenario with one reader and many tags randomly deployed in the environment is an uplink channel – the tags might be all at different distances, and the backscatter signals are received asynchronously. While it is possible to synchronize users on the downlink, where all signals originate from the same transmitter, it is more challenging to synchronize users in the uplink, since they are not co-located. Hence, Walsh-Hadamard codes are rarely used for uplink channels, and it is common practice in existing system to use quasi-orthogonal codes (such as Gold or Kasami codes) or other PN sequences [54].

The choice of the spreading sequence deeply impact the performance of the network, and its features set bounds on the system capacity. ML codes are the largest codes that can be generated by a shift register, and have a period of $2^m - 1$, where m is the length of the shift register, but they provided too few codes. For example, for $m = 7$ we have only 7 codes of length $L = 2^m - 1 = 127$. Differently, we saw before

that Gold codes are generated from a XOR combination of a preferred pair of ML codes. Hence, a set of Gold codes is made up of the $2^m - 1$ codes generated from the multiplication, plus the two original ML codes, giving $2^m + 1$. For example, for $m = 6$ there exist 65 Gold codes (and even more with long Kasami codes) of length $2^m - 1$.

Multiuser spread-spectrum systems where noise can be neglected in the performance analysis are called interference-limited, since noise is negligible with respect to interference. Let's suppose initially that all users have the same transmit power, pseudo-random spreading codes with N chips per symbol, random start times, and random carrier phases. If the interference in a multiuser system has approximately Gaussian statistics, we can derive the output of a BPSK asynchronous receiver. Specifically, the average SINR for asynchronous users on this channel [51] is given by

$$\text{SINR} = \frac{1}{\frac{K-1}{3N} + \frac{N_0}{2E_s}} \quad (46)$$

For interference-limited systems we neglect the noise term N_0 to get the SIR

$$\text{SIR} = \frac{3N}{K-1} \quad (47)$$

Care must be used in applying these standard Gaussian approximations for SINR and SIR, since the SIR and SINR for a given system is heavily dependent on the spreading code properties, timing and carrier phase assumptions, and other characteristics of the system. We can modify the equation above to approximate the SIR associated with non-random spreading codes as

$$\text{SIR} = \frac{3N}{\xi(K-1)} \quad (48)$$

where ξ is a constant characterizing the code cross-correlation that depends on the spreading code properties and other system assumptions. The effect of fading can be captured by adjusting ξ to reflect the average cross-correlation under the fading model. Under the standard Gaussian assumption $\xi = 1$, whereas for PN sequences, $\xi = 2$ or $\xi = 3$, depending on the system assumptions (for more information on ξ please see [51] and references within).

Suppose now that all $K - 1$ interference terms have channel gain $\alpha \gg \alpha_k$. The SIR for the k th user then becomes

$$\text{SIR}_k = \frac{\alpha_k^\gamma N}{\alpha^\gamma \xi (K-1)} \quad (49)$$

so the k th user in the uplink suffers an SIR penalty of α_k/α due to the different channel gains, where γ is the path loss exponent (ideally $\gamma = 2$).

This value of SIR is valid for multiple user all operating at the same distance. However, if we assume that a tag is located at a distance d with respect to a reference distance d_0 , the expression for received power can be referenced to a measurement of power received at any distance in the far-field. For example, if d_0 is in the far-field, then for any distance d greater than d_0 , the power received can be expressed [55] by:

$$P_r(d) = P_r(d_0) \left(\frac{d_0}{d} \right)^\gamma \quad (50)$$

If we assume zero attenuation or reflection due to fading, we can set $\gamma = 2$. Moreover, we can normalize d with respect to the reference distance d_0 . Setting a reference transmission power of 1W, we can rewrite the received power as:

$$P_r(d) = \left(\frac{1}{\beta_k} \right)^2 \quad (51)$$

where $\beta_k = \frac{d}{d_0}$. Similarly, the SIR for the k th node becomes:

$$\text{SIR}_k = \frac{3N}{\beta_k^2 \xi (K-1)} \quad (52)$$

Finally, we can assume that distances d_k are randomly distributed according to $d = X \cdot d_0$, where X is distributed as Rayleigh variable with a probability density function

$$f(x) = xe^{-x^2/2}, \quad x \geq 0, \quad (53)$$

where the scale parameter of the distribution $\sigma = 1$.

We know that the mean of this Rayleigh random variable can be expressed as:

$$\mu(X) = \sigma \sqrt{\frac{\pi}{2}} = \sqrt{\frac{\pi}{2}} \quad (54)$$

hence, using the properties of generalized mean, the average SIR computed over K users can be rewritten as

$$\text{SIR}_{avg} = \frac{\sqrt{\frac{2}{\pi}} 3N}{\xi(K-1)} \quad (55)$$

And the Bit Error Rate (BER) can be computed from the SIR (or SINR) using the following standard formula [50]:

$$BER = \frac{1}{2} \operatorname{erfc}(\sqrt{\text{SIR}}) \quad (56)$$

3.13.4 Preliminary results for the spread-spectrum model

In order to evaluate the detection capabilities of the proposed approach, performances have been investigated using numerical simulations in MATLAB. Results are presented in terms of raw Bit Error Rate (BER) for different noise channel conditions and spreading codes. We consider a PN Gold sequence of length $N = 2^m$ (a 0 was added to the codes to adjust their length to perfect powers of 2). From Section 3.13.2 we also know that the maximum allowed number of tags is $K = 2^m + 1$, which can be rounded to $K = 2^m$ for practical purposes. As a result, for a given value of m , we consider a sequence of length 2^m and a maximum number 2^m of nodes.

The preliminary results obtained by means of simulation are presented in Figures 64 to 66. In all configurations we evaluated the BER as a function of SIR, while we fixed the SNR to 7dB, which corresponds to an error floor of about 10^{-3} without interference, i.e. a single reader-tag channel.

In Figure 64, performance of the reader is presented for an increasing number K of deployed tags in the network and a value of $m = 6$. As expected, the proposed schema handles quite well the interferences: its decoding efficiency degrades smoothly and the average BER remains below 10^{-2} with up to 30 concurrent tags.

Figure 65 compares the decoding efficiency of two PN codes, one with $m = 6$ and the other $m = 4$ under the same channel noise conditions mentioned above. As expected, the performance of the longer code is significantly better because it uses more bandwidth to spread the same information. It is useful to remind that robustness and increase in network size is desirable, but it comes at a price: longer codes means also higher energy consumption and longer delay budget.

Finally, Figure 66 depicts the different performances achievable in presence of nodes deployed at random distances, generated according to a Rayleigh distribution with unitary scale factor. For each possible value of K , we have simulated D random deployments and computed the mean BER for each deployment of K tags. Then, we have extracted the mean BER_K , averaged over all D simulations for a network of K tags. We found that $D = 10.000$ simulations are enough to obtain realistic results: as visible in the figure, the numerical results follow the theoretical curves with high accuracy.

Compared to a RFID network of tags all transmitting at the same reference distance d_0 to the receiver, randomly deployments exhibit on average worse performance – this is not surprising, since some tags might fall quite far from the reader.

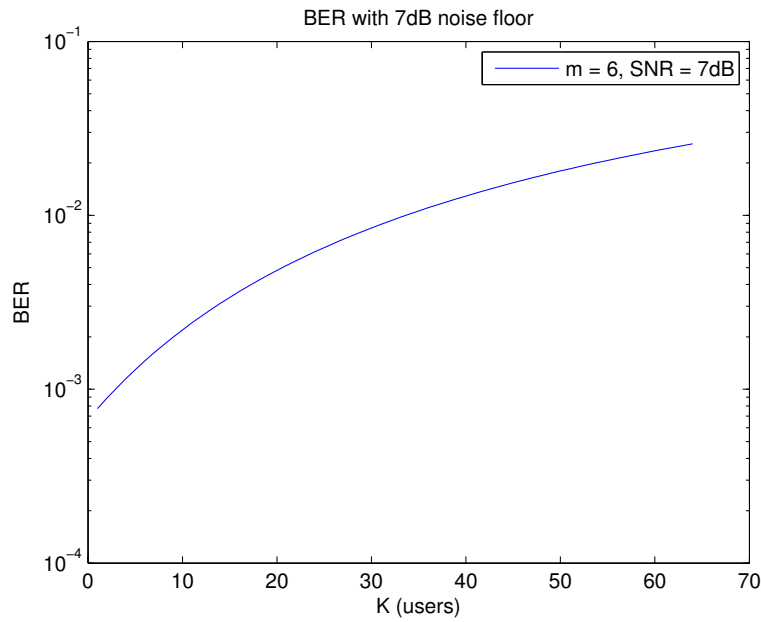


Figure 64: BER as a function of SIR (PN code of length 2^6 and SNR equal to 7dB).

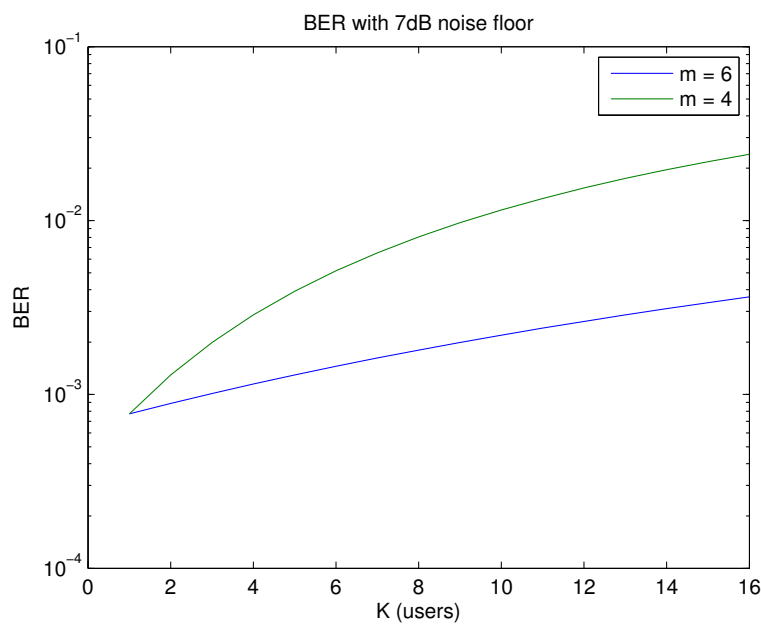


Figure 65: Comparison of BERs obtained with different code lengths (SNR equal to 7dB).

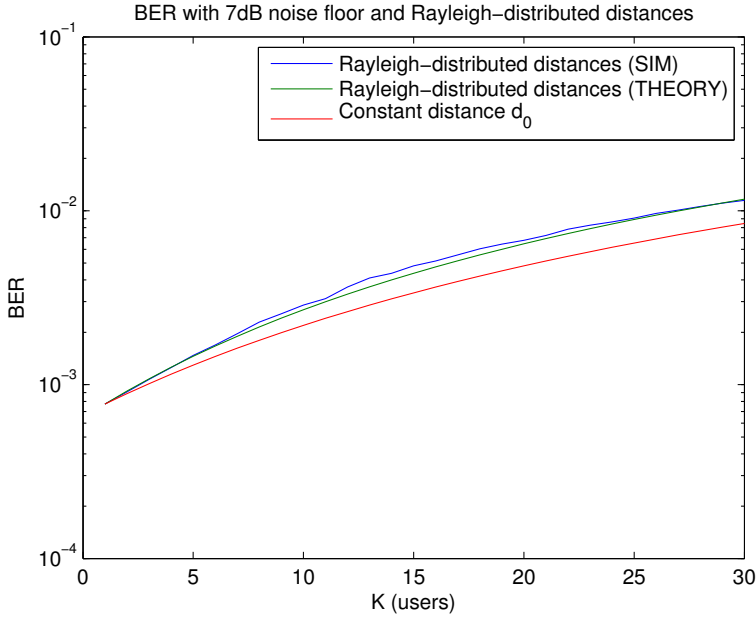


Figure 66: Performance of a network with tags randomly deployed at different distances, distributed as a normalized random Rayleigh variable (SNR equal to 7dB).

3.13.5 ISO/IEC 18000-6C anti-collision protocol

According to the specifications of ISO/IEC 18000-6 MAC, an interrogation round is defined as a sequence of consecutive commands and responses that are issued by the reader and replied back by the tag in order to transmit the tag ID to the reader. A sequence of consecutive interrogation rounds forms an interrogation session. At the beginning of the session, the reader sends a *Query* command with an integer parameter Q , asking every tag to generate a 16-bits random number (RN16) uniformly and to mask Q bits of the generated RN16 to determine their slot counter. At each round, the reader sends *QueryRep* commands in response of which tags decrement the slot counter. Tags respond with their RN16 when their counter counts down to 0, forming a framed slotted ALOHA multi-access system over a duration of 2^Q slots. Assuming that a single tag replies, the reader acknowledges by sending an ACK that includes the received RN16. Every tag decodes the ACK; if the included RN16 matches its own RN16 at a tag, it responds by transmitting its packet (denominated EPC message). After sending the packet, the tag will not respond to *Query/QueryRep/QueryAdj* messages in the same session. A *QueryAdj* command is issued by the reader to instruct all tags to adjust the value of Q and re-select their slot number based on the new Q value according to an adaptive Q algorithm, which we describe next.

The standard Q algorithm in ISO/IEC 18000-6C is based on an additive increase/decrease mechanism, such that the value of Q is either incremented when multiple collisions are detected or decremented after consecutive idle rounds. The increment/decrement rate of Q is specified by a parameter c . A variable Q_{fp} is defined such that at each collision, the value of Q_{fp} is incremented by c . If Q_{fp} exceeds a maximum value Q_{\max} , it is set at Q_{\max} . Similarly, the value of Q_{fp} is decremented by c at each idle round. If Q_{fp} is lower than a minimum value Q_{\min} , it is set at Q_{\min} . The value of Q is selected as the nearest integer to Q_{fp} , i.e., $Q = \text{round}(Q_{fp})$. The value of Q is kept unchanged whenever the interrogation is successful. The ISO/IEC 18000-6 Type C standard [48] sets an initial value of Q as $Q_0 = 4$, while c is in the range $0.1 \leq c \leq 0.5$. Default parameters are $Q_{\min} = 0$ and $Q_{\max} = 15$.

We consider two indicators to evaluate the performance of the MAC as follows [17].

- Query Success Rate (QSR): it defines the average rate at which query commands successfully identify a tag; in other words, it is the average probability of identifying a tag in a query round.
- Tag Interrogation Speed (TIS): it defines the average rate at which tags are successfully identified.

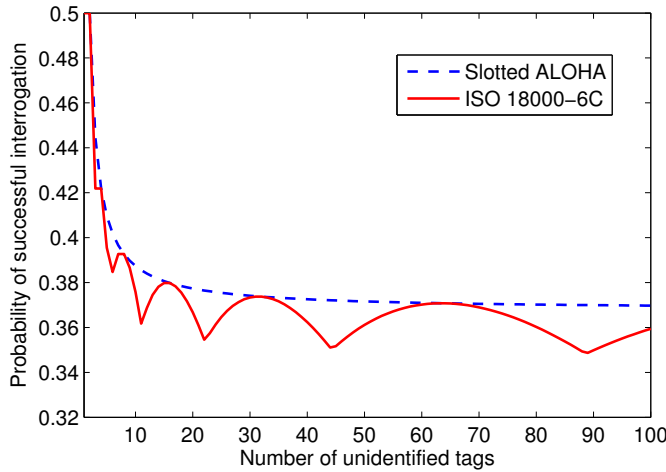


Figure 67: Probability of successful interrogation vs. current number of unidentified tags.

It accounts for the different duration of idle rounds, collided rounds, and successful rounds. Both the QSR and the TIS depend on protocol specifications as well as the number of tags, the distance between the tag and the reader, environment, etc. In this analysis we assume static channel conditions and zero bit-error rate. Moreover, as we are interested on assessing basic performance of the MAC protocol, we here neglect the effects of antenna polarization on determining the communication range of the reader.

In Fig. 67, we report the theoretical probability of successful interrogation vs. the current number of unidentified tags. We compare the classic slotted ALOHA and the ISO/IEC 18000-6C MAC. The probability of successful interrogation of both systems quickly decreases as the number of unidentified tags increases, with theoretical bound at ≈ 0.367 for $N \rightarrow \infty$. For ISO/IEC 18000-6C MAC, local maxima are achieved for $N = 2^Q$, $Q \in \mathbb{Z}$. The result suggests that the performance of the protocol is improved if the average number of tags participating in each query is low (i.e., $N < 20$).

3.13.6 Proposed algorithm for fast identification with ISO/IEC 18000-6C MAC

In this section, we describe the proposed mechanism for fast identification and we compare the performance with the standard ISO/IEC 18000-6C MAC. The ISO/IEC 18000-6C MAC is designed by considering that the number of tags and their position are not known a priori. However, in the presence of UWB modules, the reader can perform accurate and fast ranging in parallel with the ISO/IEC 18000-6C MAC. Then, it is possible to adapt the transmission range of the reader so that the average number of tags in each query is kept under control. The proposed integration works as follows:

UHF power up and UWB ranging

- The reader transmits a continuous-wave UHF signal to power up the tags in its maximum transmission range $RangeMax$.
- The reader sends a sequence of UWB pulses and tags respond by modulating the backscattered UWB signal.
- The reader estimates the number of tags and the relative distance by considering the time of arrival (ToA) of the backscattered signals.

UHF interrogation

- The reader sends a *Query* command with sufficient power to interrogate N_0 tags ($Range0$), and selecting $Q = \lceil \log_2 N_0 \rceil$, where $\lceil \cdot \rceil$ denotes the nearest integer function.
- After $x \leq N_0$ tags have been identified, the reader increases the transmission power of the following *Query* command to reach and include x further tags to the interrogation ($Range1$).
- The transmission range is increased every x successful interrogations until it reaches $RangeMax$.

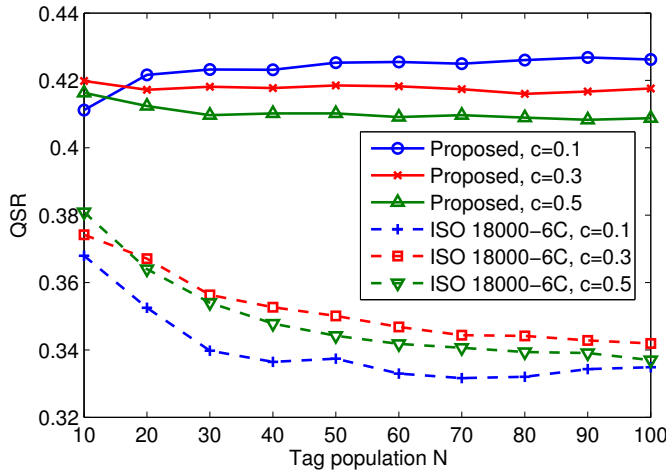


Figure 68: QSR vs. tag population. The proposed approach guarantees 25% improvement to the standard ISO/IEC 18000-6C for large-scale networks.

- Between consecutive *Query* commands, the interrogation proceeds by using *QueryRep* and *QueryAdj* commands according to the standard procedure. The transmission power is set to reach also tags that are interrogated in the next *Query*. By doing so, those tags are already powered when receiving the *Query* command.
- The session ends when all tags have been identified.

We recall that the proposed adaptation is compliant with the ISO/IEC 18000-6C specifications for both the reader and the tag. The optimal choice of the parameters N_0 and x is not straightforward. Every time the reader includes new tags, it has to issue a *Query* command instead of a shorter *QueryAdj* command. Therefore, if N_0 and x are too small, the TIS is negatively affected.

3.13.7 Preliminary results for the proposed enhancement of ISO/IEC 18000-6C MAC

A single reader is deployed to interrogate a population of $N = [10 - 100]$ tags operating with the standard ISO/IEC 18000-6C. The air interface parameters are set to default specifications in [48] for tag modulation rate of 125 KHz. We show the performance results in terms of QSR in Fig. 68 and TIS in Fig. 69 of the standard ISO/IEC 18000-6C MAC and the proposed approach with $N_0 = \min\{N/2, 10\}$ and $x = 5$ for various values of c . We recall that a larger value of c indicates fast adaptation of the backoff window after collided and idle rounds. The proposed mechanism improves the performance of the ISO/IEC 18000-6C MAC in the considered range of tag population and values of c . For $c = 0.1$ and $N = 100$, the proposed mechanism achieves $\text{QSR} \approx 0.43$ with 25% gain with respect to the ISO/IEC 18000-6C, and $\text{TIS} = 513$ tags/s with 7% gain in terms of tag identification speed as the tag population increases.

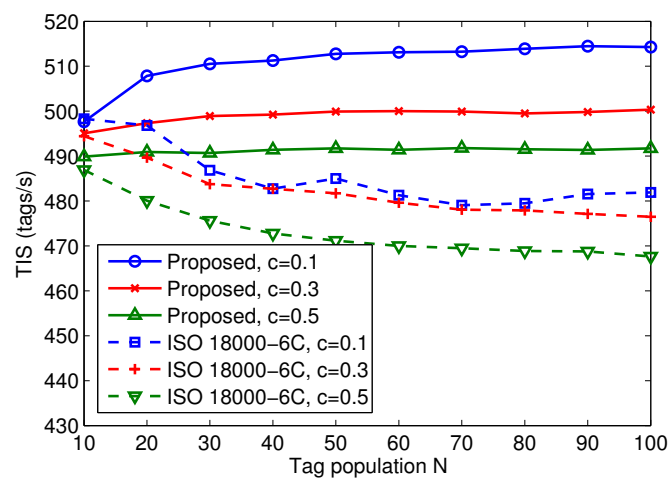


Figure 69: TIS vs tag population. The proposed approach guarantees 7% improvement to the standard ISO/IEC 18000-6C for large-scale networks.

4 LINK AND POWER BUDGET

4.1 Link budget

In this section we provide the link budget analysis of the system previously described, considering different layouts and parameters.

4.1.1 Channel Path Loss

The RRC pulse with central frequency $f_c = 4$ GHz, satisfying the EU-UWB regulation in the 3.1 – 4.8 GHz band has been considered as transmitted waveform are reported in Fig. 70 and Fig. 71. For

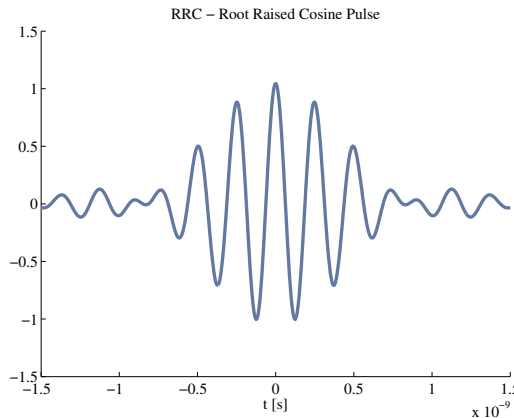


Figure 70: Transmitted pulse.

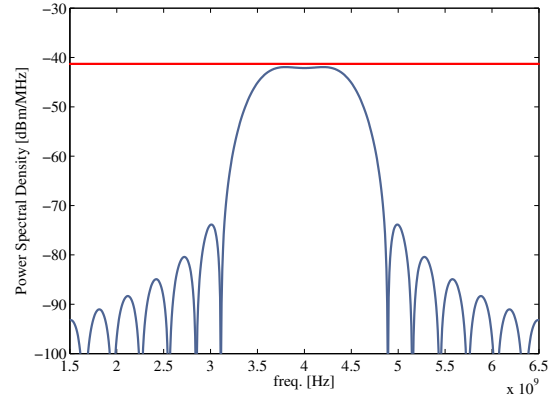


Figure 71: Transmitted pulse's PSD.

what tags' and readers' antennas are concerned, 3D simulated radiation patterns have been included into simulations. We assume the radiation patterns equal to their value at the central frequency neglecting frequency selectivity. The same transmitting and receiving UWB antennas are considered for readers (in a monostatic scenario) and receivers (in a multistatic scenario), that is a dipole antenna attached to a reflector, which presents a maximum gain of 5.35 dBi. When the transmitters cover also the role of amplify & forward (AF) relays (with an amplifier gain of $G_{\text{relay}} = 10$ dB), the receiving unit includes two types of antenna: the dipole attached to a reflector, as before, directed towards the environment where tags are located, and a Yagi-Uda (maximum gain of 13.6 dBi), which is directed towards the transmitter-relay forwarding the signals from and to the tags. The transmitters adopt an UWB patch antenna (maximum gain 7.76 dBi) while for tags we have considered either a dipole antenna (maximum gain 2.15 dBi) and a dipole attached to a reflector, as if attached to a metallic surface. In Fig. 72, the 3D radiation patterns of these antennas are reported.

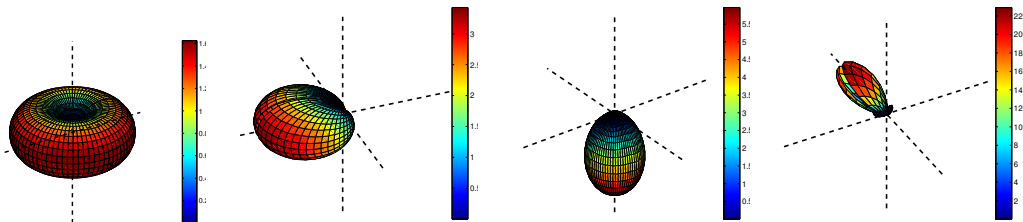


Figure 72: Dipole, Dipole with Reflector, Patch and Yagi-Uda Antenna Radiation Pattern.

Now consider the evaluation of the path-loss for each tag position. The path-loss PL is conventionally defined as

$$PL(d) = \frac{P_{\text{tx}}}{P_{\text{rx}}} \quad (57)$$

where P_{tx} and P_{rx} are the transmitting and receiving powers, respectively.

From the well known Friis formula, the single hop path-loss in dB is given by

$$PL(d) = PL_0(d_0) + 10\beta \log\left(\frac{d}{d_0}\right) - G_1(\theta_{12}, \phi_{12}) - G_2(\theta_{21}, \phi_{21}) + L_{\text{sup}} \quad (58)$$

where d is the distance, d_0 is the reference distance (in the following it will be 1 m), G_i is the gain of the i th antenna, (θ_{ij}, ϕ_{ij}) is the couple of elevation and azimuthal angles under which the i th and j th antenna see each other and L_{sup} accounts for supplementary losses due to the backscattering process (i.e. losses due the internal architecture of the tag, UWB switch, etc.).

$PL_0(d_0)$ is the path-loss (free-space) at the reference distance in dB

$$PL_0(d_0) = 20 \log\left[\frac{4\pi d_0 f_c}{c}\right] \quad (59)$$

Moreover, we can calculate the maximum level of path-loss allowed at the receiver side once the minimum SNR, required to detect the tag, is fixed considering N_s received pulses and added coherently as:

$$\text{SNR} \triangleq \frac{P_{\text{rx}} \cdot T_p \cdot N_s}{N_0} = \frac{P_{\text{tx}} \cdot T_p \cdot N_s}{N_0 \cdot PL(d)} \quad (60)$$

As a consequence we find that:

$$\text{SNR}_{\min} = \frac{P_{\text{tx}} \cdot T_p \cdot N_s}{N_0 \cdot PL_{\max}(d)} \quad (61)$$

Given a possible tag position, we simulated M_c random tag radiation pattern orientations, and for each orientation we compared the received SNR with the minimum SNR_{\min} required at receiver side to detect the tag.

Fixed the n th position, the percentage of times that a tag is detected is given by

$$C^{(n)}(\text{SNR}_{\min}) = \frac{1}{M_c} \sum_{m=1}^{M_c} \mathbf{1}(\text{SNR}_m - \text{SNR}_{\min}) \quad (62)$$

where we have defined the unit step function $\mathbf{1}(x) = 1$ if $x \geq 0$ and 0 otherwise, and SNR_m is the received SNR for the m th Monte-Carlo iteration. At each Monte-Carlo iteration, the orientation of the tag changes and thus, the orientation of its radiation pattern varies as well. The complete list of simulation parameters of both monostatic and multistatic configurations are reported in Tab. 8.

Table 8: Simulation Parameters.

Parameter Symbol	Parameter Description	Value	Units
T_p	Frame Time (pulse repetition period)	128	ns
N_s	Number of emitted pulses per symbol	1	
$EIRP$	Effective Isotropically Radiated Power	-12	dBm
T_w	Pulse Time Duration	1	ns
Γ	Roll-off factor	0.6	
f_c	Central frequency	4	GHz
β	Path-loss exponent	2	
W	Bandwidth	1.6	GHz
F	Receiver Noise Figure	4	dB
L_{sup}	Tag and Implementation Losses	10	dB
M_c	Monte-Carlo iterations	100	

4.1.2 Link Budget Analysis

The aim of this section is to provide the link budget analysis for different scenarios.

The scenarios considered are reported in Fig. 73: in the top figures, a monostatic configuration is depicted in which a reader interrogates a single tag; in the bottom figures, we focus on a multistatic configuration with multiple transmitters and a receiver.

For each scenario two cases are taken into consideration: in the former, the reader's position is $[x_{\text{read}}, y_{\text{read}}, z_{\text{read}}] = [0, 5, 2.5]$ m and the maximum of its antenna radiation pattern is oriented towards the test position $[5, 5, 1]$ (i.e. the mid-point of the tag's trajectory) while the tag moves along a line in front of the reader but at a smaller height (i.e. x_{tag} is the only coordinate which varies, while $[y_{\text{tag}} = 5, z_{\text{tag}} = 1]$ are fixed); in the latter, the reader and the tag are at the same height ($z_{\text{read}} = z_{\text{tag}} = 1$ m), so that the angle under which the tag intercepts the reader's antenna radiation pattern is always correspondent to the reader's maximum gain.

Three transmitters ($N_{\text{tx}} = 3$) are adopted in the multistatic scenario placed at coordinates $[x_{\text{t}1}, y_{\text{t}1}, z_{\text{t}1}] = [2, 5, 4]$ m, $[x_{\text{t}2}, y_{\text{t}2}, z_{\text{t}2}] = [5, 5, 4]$ m and $[x_{\text{t}3}, y_{\text{t}3}, z_{\text{t}3}] = [8, 5, 4]$ m. The Monte-Carlo iterations are set to $M_c = 5000$.

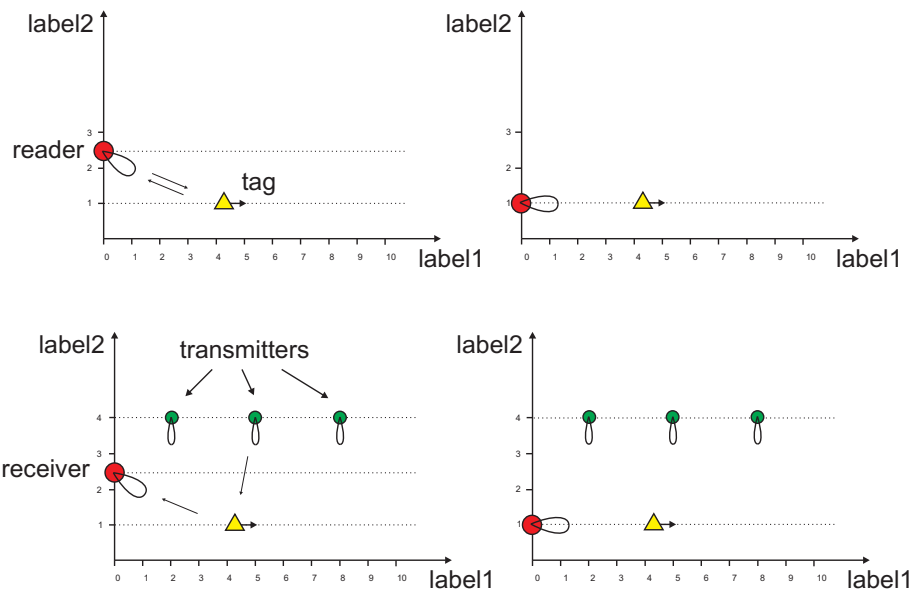


Figure 73: Monostatic (top) and Multistatic (bottom) scenarios with different receiver's height.

Figure 74 reports different values of the average SNR, SNR_{mean} , obtained when the reader and the tag are at the same height ($z_{\text{reader}} = z_{\text{tag}} = 1$ m) in a monostatic configuration. Moreover, we consider the case in which the tag is passive and equipped with a dipole antenna attached to a reflector as more realistic and representative of a situation where a tag attached to an object. The SNR evaluated over $M_c = 5000$ tag's orientation is reported as a function of the tag's distance from the reader. Tag's positions are 0.25 m spaced. In addition, curves for different processing gain N_s are analyzed ($N_s = 512, 1024, 2048, 4096, 8192, 16384$). It is evident that increasing N_s more pulses are accumulated at the receiver section improving the SNR_{mean} , at the expense of a slower refresh rate.

In Fig. 75 the same simulation has been repeated for the multistatic scenario. As we can see, the overall performance improves: For example, for $N_s = 8192$ and $x_{\text{tag}} = 5$ m, the SNR_{mean} considering a monostatic configuration is 0.70 dB while in a multistatic one 13.58 dB. The SNR_{mean} curves are wavy with peaks corresponding to the transmitters' positions. In fact, when the tag's position is $[x_{\text{tag}} = x_{\text{t}i}, y_{\text{tag}}, z_{\text{tag}}]$ with $i = 1, 2, 3$ the path between the i th transmitter and the tag is minimum and the transmitter's patch antenna is intercepted at its maximum gain value.

Now, fixing $N_s = 1$ and adopting the multistatic scenario, we aim at underlying how the SNR_{mean} level changes according to the transmitter-tag distance. To accomplish this task, in Fig. 76 different room

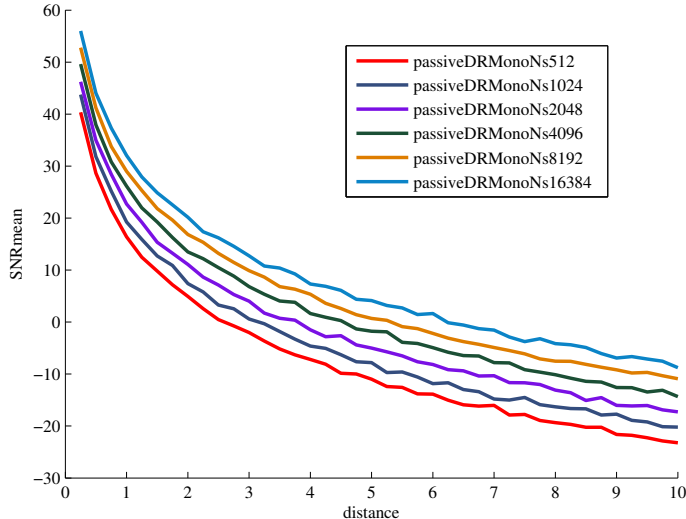


Figure 74: SNR vs distance considering different N_s value in Monostatic Scenario, where a dipole antenna, acting as tag, is considered attached to a reflector.

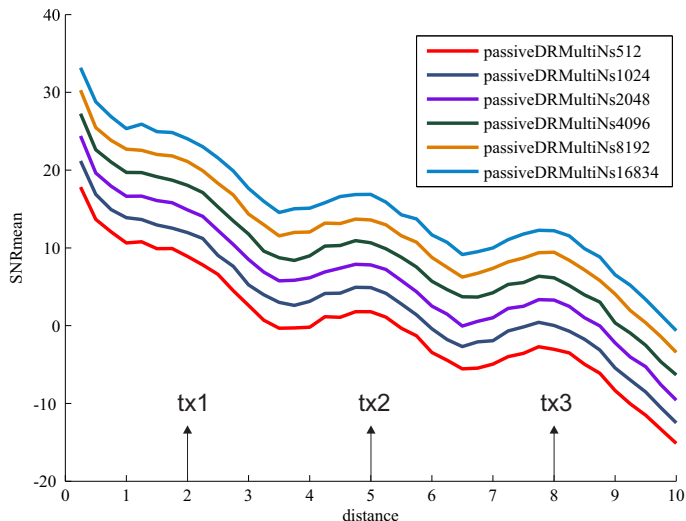


Figure 75: SNR vs distance considering different N_s value in Multistatic Scenario with a dipole with reflector passive tag

heights have been adopted ($z_{\text{room}} = 3, 4, 5$ m). Note that the actual SNR for a given processing gain $N_s > 1$ can be easily obtained by adding (in dB) the processing gain to the reported value of SNR.

In Fig. 77 and 78, we want to stress the idea that different tag's antenna radiation patterns could lead to slightly different SNR_{mean} value. We have considered a passive tag's dipole and a dipole-reflector antenna in monostatic and multistatic scenario. Moreover, in Fig. 78 some performance curves for active tags are shown: Obviously, the case of active tags lead to a better SNR_{mean} as only one-hop is present between the tag and the receiver instead of the two-hops necessary when passive tags are adopted.

In Fig. 79, two different z_{read} are taken into consideration. When the reader and the tag are at the same height and the reader's antenna radiation pattern orients its maximum gain towards the tag's trajectory, the received SNR is higher than the case in which the reader is at a different level (for example $z_{\text{read}} = 2.5$ m) and with the radiation pattern's maximum oriented towards the mid-point of tag's trajectory. In this second case, the maximum SNR_{mean} is achieved when the tag is at $[x_{\text{tag}}, y_{\text{tag}}, z_{\text{tag}}] = [1.5, 5, 1]$ as it represents the best trade-off between reader-tag distance and antennas's gain.

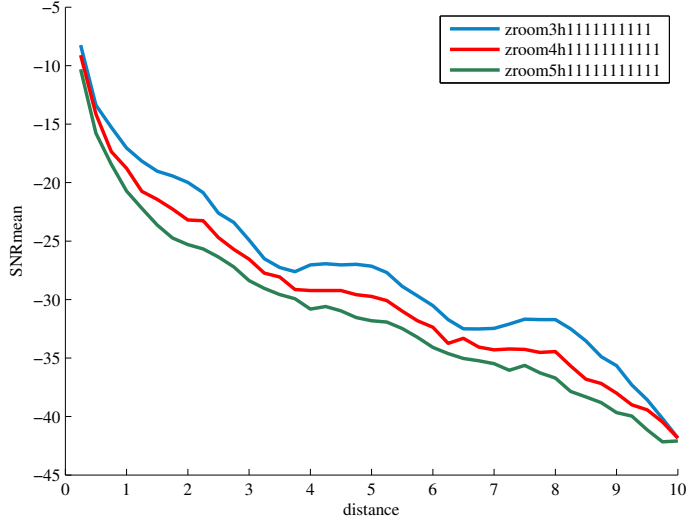


Figure 76: SNR vs distance considering different room heights in Multistatic Scenario with $N_s = 1$.

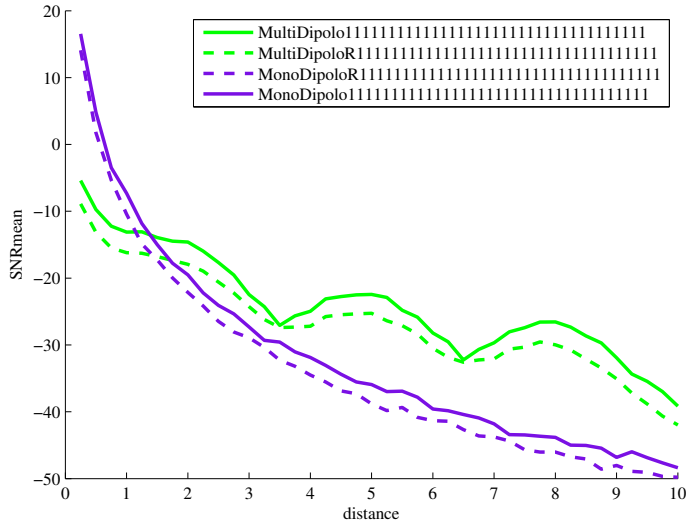


Figure 77: SNR vs distance considering Monostatic and Multistatic Configuration and different tag's antenna pattern (dipole and dipole attached to a reflector) with $N_s = 1$

4.1.3 Coverage Results

In the following, some area coverage results are reported considering the scenarios hereafter depicted. We consider an indoor environment with dimensions $[x_{\text{room}}, y_{\text{room}}, z_{\text{room}}] = [10, 10, 5]$ m in which the tag can move on a grid of points equally spaced of 25 cm at a height of $z_{\text{tag}} = 1$ m.

The following different scenarios are taken into consideration (see Fig. 80):

- *Monostatic scenario*: a reader of coordinates $[x_{\text{read}}, y_{\text{read}}, z_{\text{read}}] = [0, 5, 2.5]$ m is either transmitter and receiver and it sends interrogation signals to detect tags.
- *Multistatic scenario without relay*: in this scenario, a shower of transmitters is placed on the ceiling (in the numerical results we consider configuration for $N_{\text{tx}} = 9, 16, 25$ and 100 shower transmitters) while a receiver is set at the same coordinates of the reader ($[x_r, y_r, z_r] = [0, 5, 2.5]$ m).
- *Multistatic scenario with relaying*: this scenario is the same as the previous one with the exception that the transmitters have the capabilities of forwarding the signal reflected by tags towards the receiver.

These results are obtained taking into consideration the dependence of the path-loss model on:

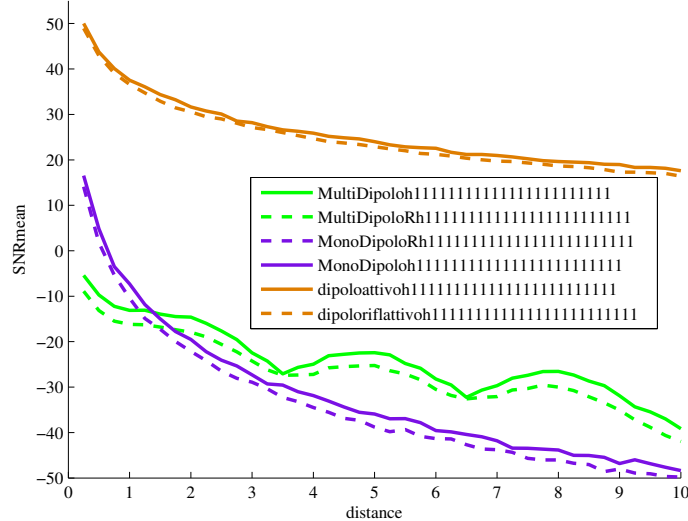


Figure 78: SNR vs distance considering Monostatic and Multistatic Configuration and different tag's antenna pattern (dipole and dipole attached to a reflector) with $N_s = 1$ in both cases of passive and active tag

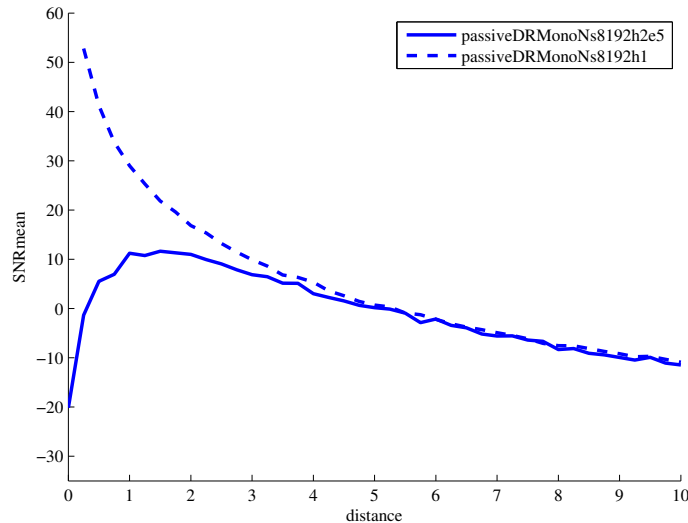


Figure 79: SNR vs distance considering $N_s = 8192$ with $z_{\text{reader}} = 1$ and $z_{\text{reader}} = 2.5$ in Monostatic configuration with dipole-reflector antenna tag and $N_s = 8192$

- room dimension, in particular room height (impacting on transmitters' distance from tag and receiver);
- antenna characteristics (i.e. the beamwidth and the antenna gain);
- the propagation environment: Free space or presence of obstacles;
- active or semi-passive/passive tag;
- SNR threshold at receiver side to perform tag's detection;
- number of transmitters and receivers.

In the following, some coverage maps for different situations are shown: They display the percentage of coverage for each tag position from 0% (blue color) to 100% (red color).

In Fig. 81 we consider an obstacle-free environment (thus, there is no necessity of relaying transmitters as there always exists a LOS path between tags and receivers) with different transmitters configurations. A map of the path-loss value is reported. The tag is equipped with a dipole antenna while in Fig. 82 it is presented the more realistic situation of a dipole antenna attached to a reflector (object).

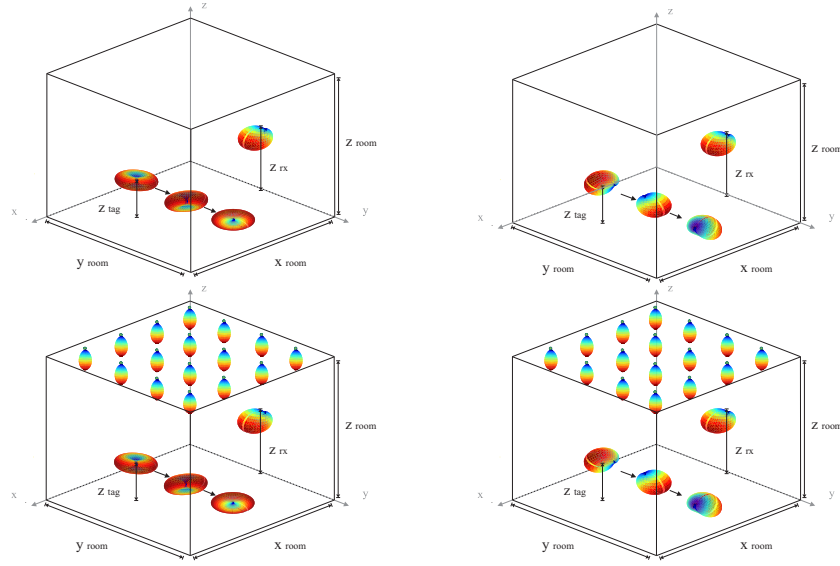


Figure 80: Monostatic and multistatic scenarios considered.

From these results, we stress the idea that an increase of the number of transmitters acting as signal "showers" results in a better coverage. This is due to the fact that the distance between the transmitter and the tag reduces either in comparison with a monostatic configuration. On the other side, increasing the number of shower elements, increases the system cost and complexity, and consequently a trade-off has to be found.

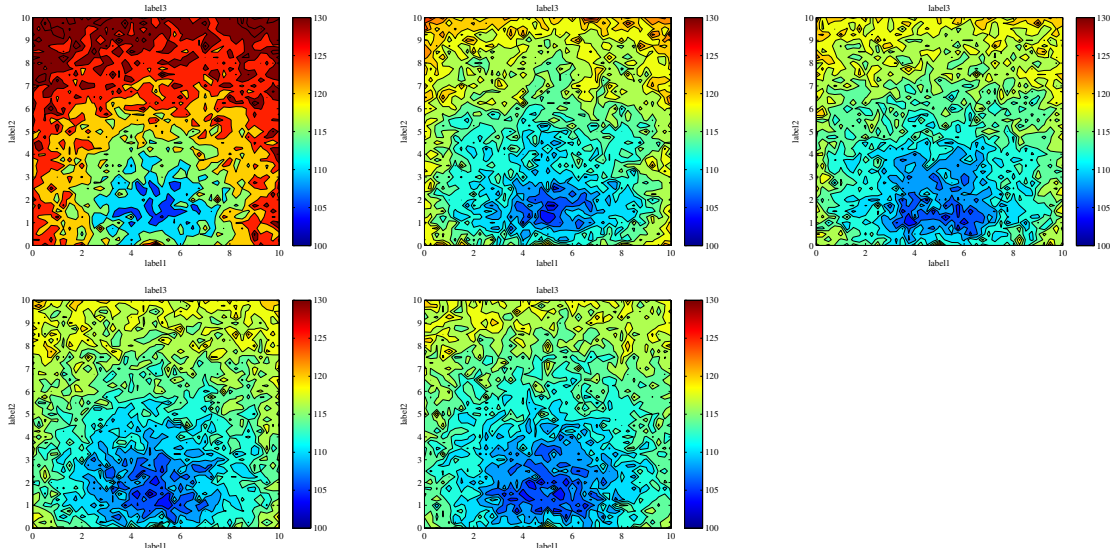


Figure 81: Path-loss in Monostatic and Multistatic Configuration (varying N_{tx}) with a Dipole Tag

Figure 83 shows coverage maps for different room heights and different tag antennas. We have fixed the $SNR_{min} = -35$ dB (with $N_s = 1$) and the number of transmitting units at $N_{tx} = 9$. It is evident that when the height of the room decreases, the coverage increases as the path between the transmitter and the tag shortens. From the comparison between the two different antenna configurations we can deduce that while using a dipole antenna could be beneficial for tag's locations near the receiver, as the pattern is omni-directional in the azimuthal plane, the adoption of a dipole antenna attached to a reflector guarantees a percentage of coverage different from 0 in positions far away from the receiver thanks to the increase

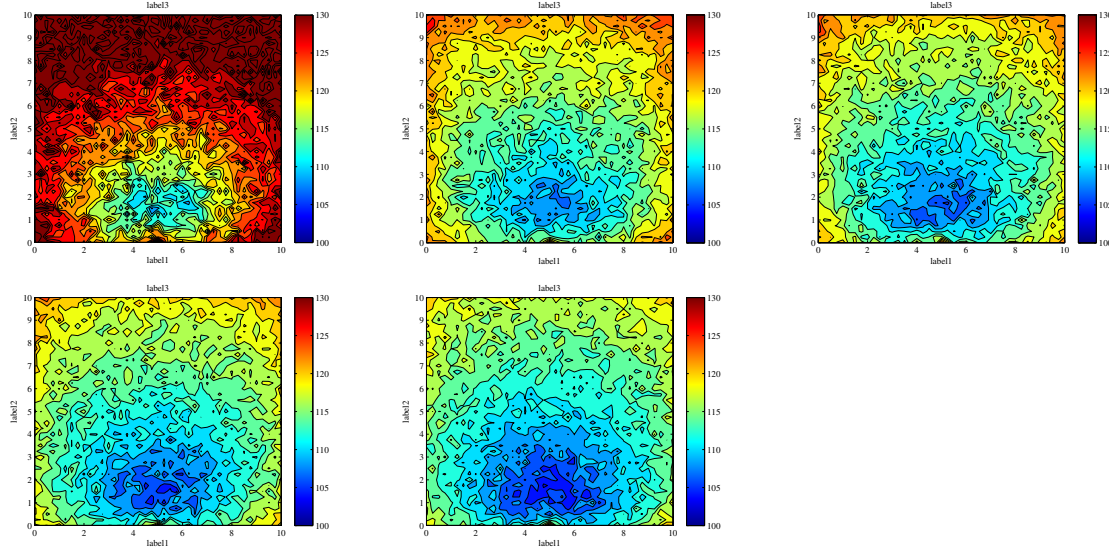


Figure 82: Path-loss in Monostatic and Multistatic Configuration (varying N_{tx}) with a Dipole Tag attached to a Reflector.

antenna gain.¹¹

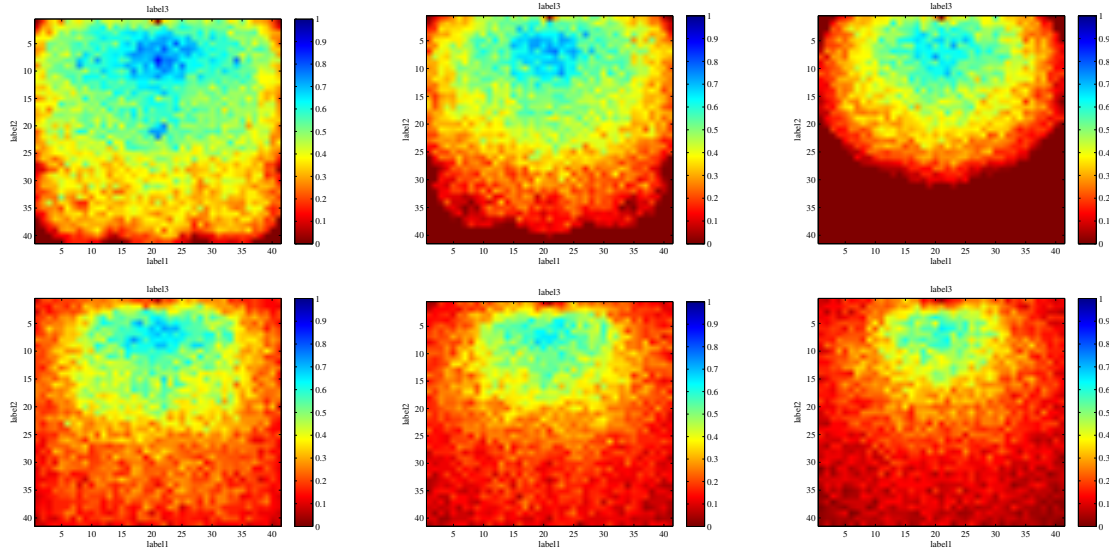


Figure 83: Coverage in Multistatic Configuration without relay, $SNR_{min} = -35$ dB, $N_{tx} = 9$ transmitters varying z_{room} and the tag's antenna ($[x_r, y_r, z_r] = [10, 5, 2.5]$)

In Fig. 84 a similar coverage comparison is conducted in which a dipole tag attached to a reflector can move in the environment with two different transmitters configuration (in particular 9 and 16 transmitters at the ceiling) and $SNR_{min} = -35$ dB. Obviously, the configuration with more transmitters results in a better coverage.

The previous results are in line with the analysis carried out in Sec.3. In fact, the adoption of passive tags which reflect the incident signals lead to a poor coverage, as two-hops have to be accounted to compute the path-loss between the transmitters and the receiver. Such limited link budget can be overcome, for example, by increasing the processing gain and/or by exploiting antenna arrays in the receiver.

¹¹In presence of a reflector behind the tag, the antenna is more directive, and thus for certain directions the link budget is more favourable [56].

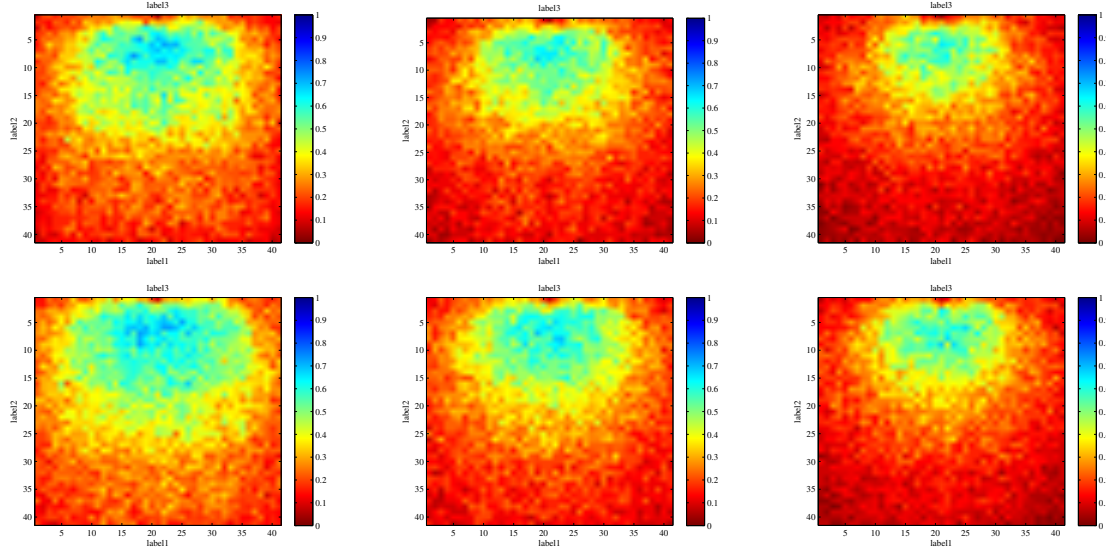


Figure 84: Coverage in Multistatic Configuration without relay, $\text{SNR}_{\min} = -35 \text{ dB}$, passive Dipole-Reflector tag varying N_{tx} ($[x_r, y_r, z_r] = [10, 5, 2.5]$)

For completeness, in the following, we investigate the advantages in adopting active tags. In Fig. 85 a coverage analysis considering active tags is shown. In this case, we have no shower of transmitters as it is the tag itself at sending the signal to the receiver. As we have only one-link (i.e. active tag-receiver) instead of two (i.e. transmitter-passive tag-receiver) the coverage improves even when the SNR requirements are more severe (we have considered different value of $\text{SNR}_{\min} = [5, 15, 20] \text{ dB}$).

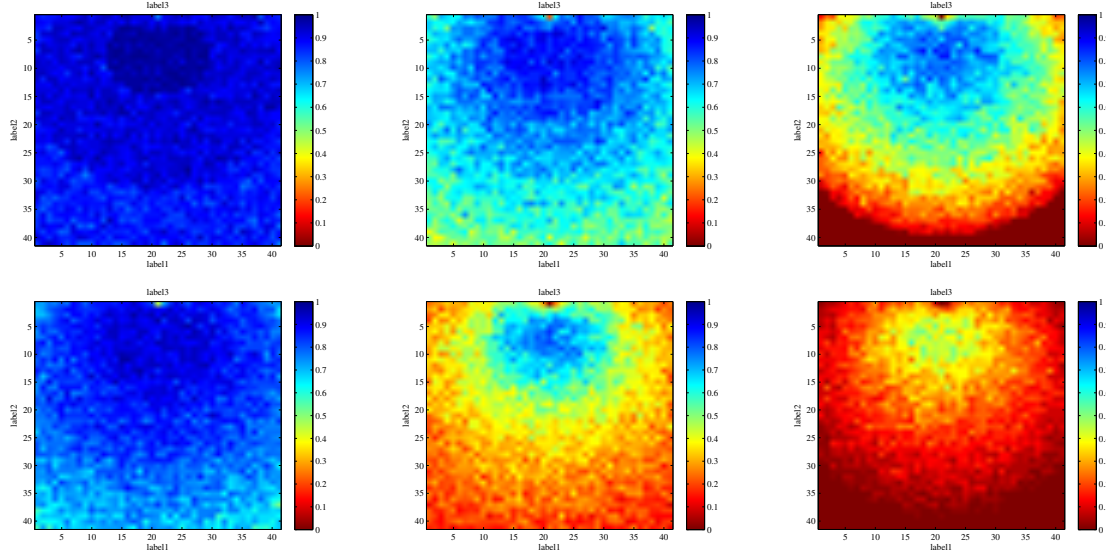


Figure 85: Coverage map in Multistatic without relay Configuration, $N_{\text{tx}} = 9$, active tags varying the SNR requirement and tag's antenna ($[x_r, y_r, z_r] = [10, 5, 2.5]$)

Until now we have considered an obstacle-free environment. From this point we aim at focusing our attention to a more complicated scenario with one or more obstacles that could create a NLOS condition between tags and the receiver.

Figure 86 different situations are depicted when a signal blocking obstacle is present in the room. In the first row of the figure, the case in which passive tags are adopted is taken into consideration: In the monostatic case only the tags between the reader and the obstacle could be covered, all the

tags beyond the obstacle can not reflect the signal coming from the reader; in the multistatic scenario with non-regenerative relay (i.e. the transmitters could forward the signal reflected by the tag), fixed $\text{SNR}_{\min} = -45 \text{ dB}$ as done for the monostatic case, the coverage does not improve. Now, in order to detect tags beyond the obstacles even if the transmitters have the double functionality of relay, we have to fix $\text{SNR}_{\min} = -60 \text{ dB}$. Unfortunately, even if relays are adopted, the link between tags and receiver includes two or three-hops which highly degrade the path gain: In fact, in case of receiver-tag LOS condition, we have a two-hop link (transmitter-tag and tag-receiver), whereas in case of NLOS we have three hops (transmitter-tag, tag-relay, relay-receiver).

In the second row, the case with active tag is considered. Differently from the the case of passive tags, the transmitters act as relays only in the tag to receiver link. As before, a comparison between the monostatic configuration and the multistatic one is presented fixing a more strict SNR requirement ($\text{SNR}_{\min} = -15 \text{ dB}$). Lowering the threshold $\text{SNR}_{\min} = -20 \text{ dB}$ almost all the possible tag test positions are covered even in presence of a completely blocking obstacle (e.g. a metallic obstacle).

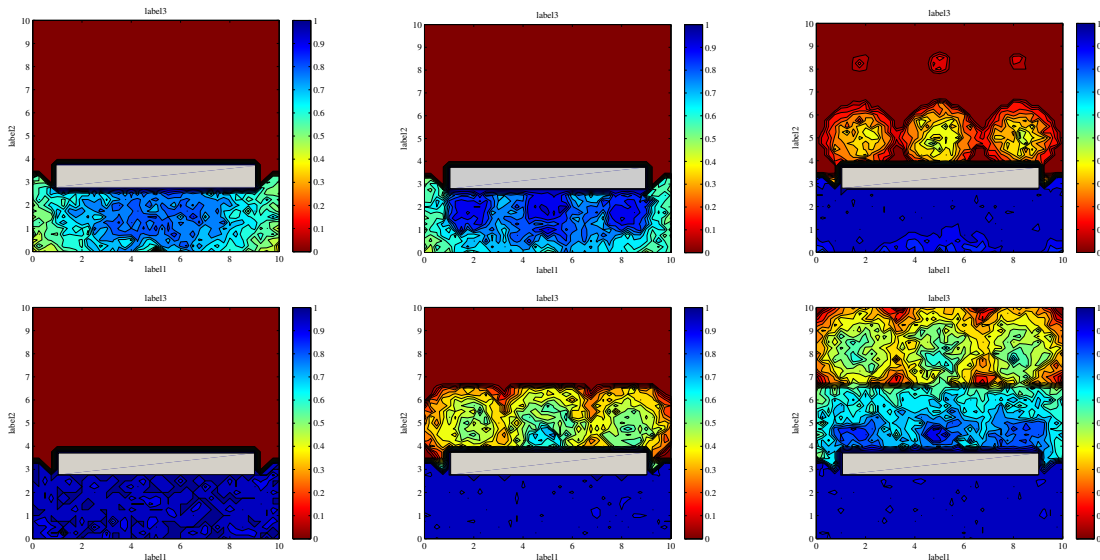


Figure 86: Scenario with one obstacle, $z_{\text{room}} = 4 \text{ m}$, $G_{\text{relay}} = 10 \text{ dB}$ varying the nature of the tag (passive or active), the SNR requirements and the configuration.

In Fig. 87 we have considered an active dipole tag and we have compared the monostatic and the multistatic scenario varying the room's height (3, 4, 5 m) and fixing the SNR_{\min} at -15 and -20 dB .

Figure 88 displays an indoor environment with more obstacles. In particular, we have considered two obstacles and we have repeated the same analysis as before: Comparison between active and passive tags with different SNR requirements at receiver side (-20 and -45 dB respectively) is reported. As before, we can see that only the multistatic with relay case with active tag guarantees a total coverage with only one receiver node and two metallic obstacles.

In Fig. 89, two receivers in positions $[x_{\text{r}1}, y_{\text{r}1}, z_{\text{r}1}] = [0, 5, 2.5] \text{ m}$ and $[x_{\text{r}2}, y_{\text{r}2}, z_{\text{r}2}] = [10, 5, 2.5] \text{ m}$ are considered. In the first row of the figure, the case of a free-space room is depicted while in the second row the case of two obstacles is reported.

To conclude, the coverage analysis has shown that in backscatter mode (passive tag) the available link budget is very limited. Active tags provide a good coverage (in LOS) but they are not battery less and hence not green. Some solutions to overcome the poor link budget have been presented. In particular, the adoption of UWB showers (multistatic scenario) can increase the coverage for moderate roof heights and the use of non-regenerative relays (multistatic scenario with relays) improves the coverage in the presence of obstacles.

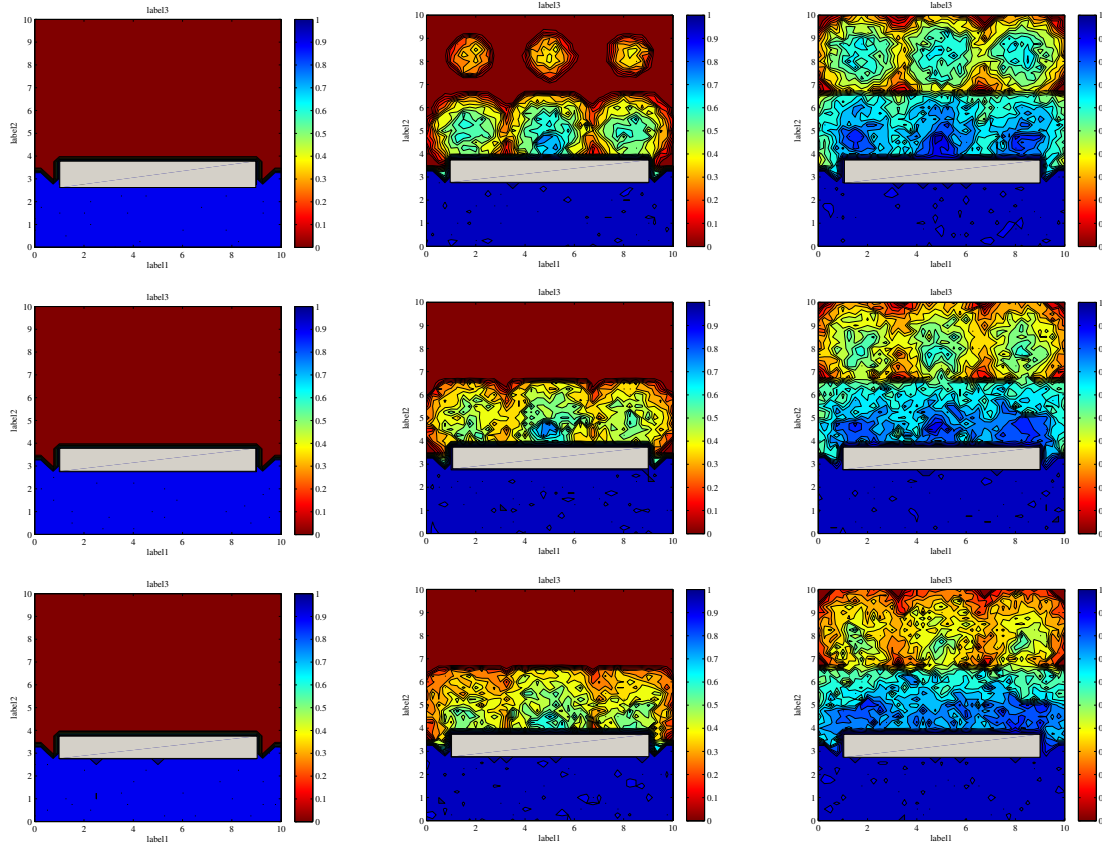


Figure 87: Scenario with one obstacle and different room heights and SNR requirements, active dipole tag, $G_{\text{relay}} = 10 \text{ dB}$

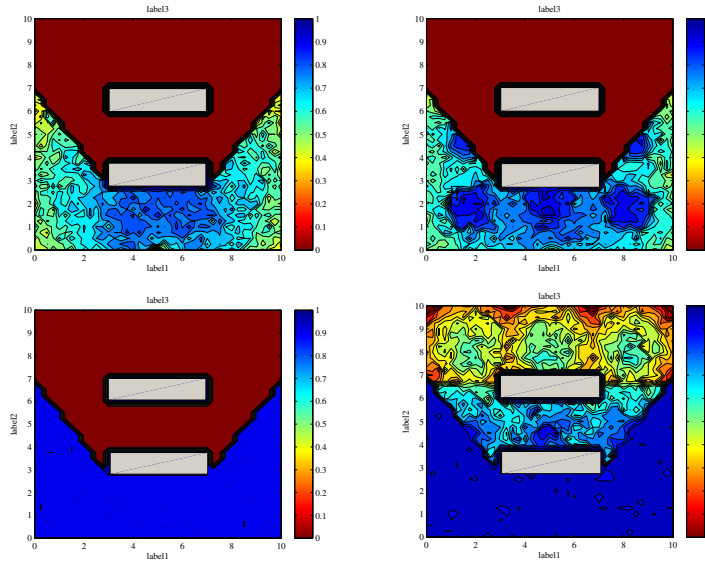


Figure 88: Scenario with two obstacles, dipole tags, $z_{\text{room}} = 4 \text{ m}$.

4.2 Power budget

In this section, power requirements for backscatter communications are analysed. In order to provide a reference value, the power requirements are computed by assessing the dynamic switching power required

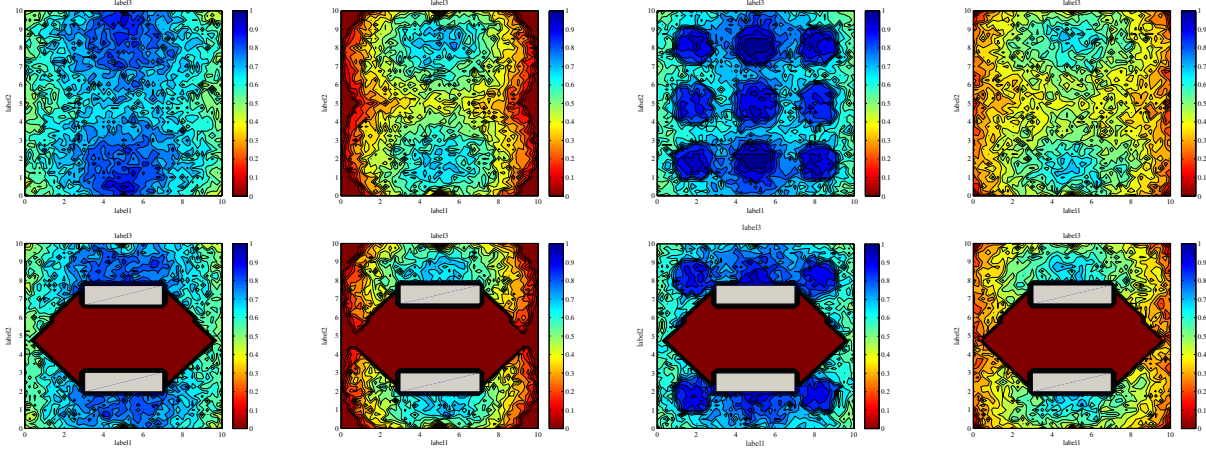


Figure 89: Scenario with two receivers with and without obstacles

to drive a field-effect transistor (FET) switch (see Fig. 90)

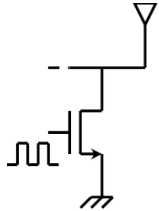


Figure 90: Reference model for assessing power requirements of backscatter communication.

Some preliminary estimates of the main system parameters can be performed. The input capacitance of the gate of the FET can be assumed to be in the order of tens of pF, $C_{SW} = 10\text{pF}$, which ensures a channel resistance of few Ω s, which can be safely be assumed as a short circuit. Let also N_s be the number of switching required for transmitting a bit of information: $N_s = 512 - 16384$. A typical supply voltage for the integrated circuit can be assumed to be $V_{DD} = 1.8\text{V}$. Other assumptions are related to the intrinsic static current of the power conversion circuit, $I_{CONV} = 200\text{nA}$ in state of the art designs. In micro-power contexts, the overall conversion efficiency can be as low as $\eta_{CONV} = 50\%$. Due to law regulations, the power P_{RF} transmitted by the RF shower should be lower than 2 W. Given these assumptions, a preliminary energy budget can be proposed. The energy required for driving the switch throughout the transmission of a single bit can be estimated as:

$$E_{bit} = N_s C_S V_{DD}^2 \quad (63)$$

In addition, the power made available by the energy harvesting circuit can be estimated as:

$$E_{HARV} = (P_{DC} \eta_{CONV} ?V_{DD} I_{CONV}) t \quad (64)$$

A single operation of single bit transmission can be safely performed when $E_{HARV} = E_{bit}$. The required exposure time to the RF shower for transmitting 1 bit can be obtained with the intersection of the two curves, i.e. the constant parametric energy requirement and the time-varying harvested energy. Figure 91 shows the results obtained with different parameter sets.

Besides this, other limitations may arise due to the geometric requirements of the storage capacitor, which should be able to store the required energy amount in the limited geometries of the green tag. For this purpose, the energy available on the storage capacitor can be estimated as:

$$E_{STORE} = \frac{1}{2} C_{STORE} V_{STORE}^2$$

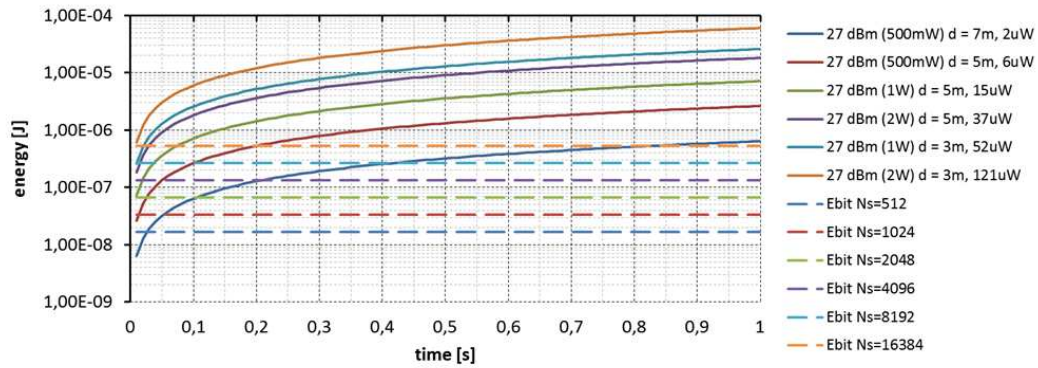


Figure 91: Power budget for backscatter communication.

The energy requirement for transmitting 1 bit of information can be compared with the energy on the storage capacitor as a function of its capacitance and voltage. The results are shown in Fig. 92.

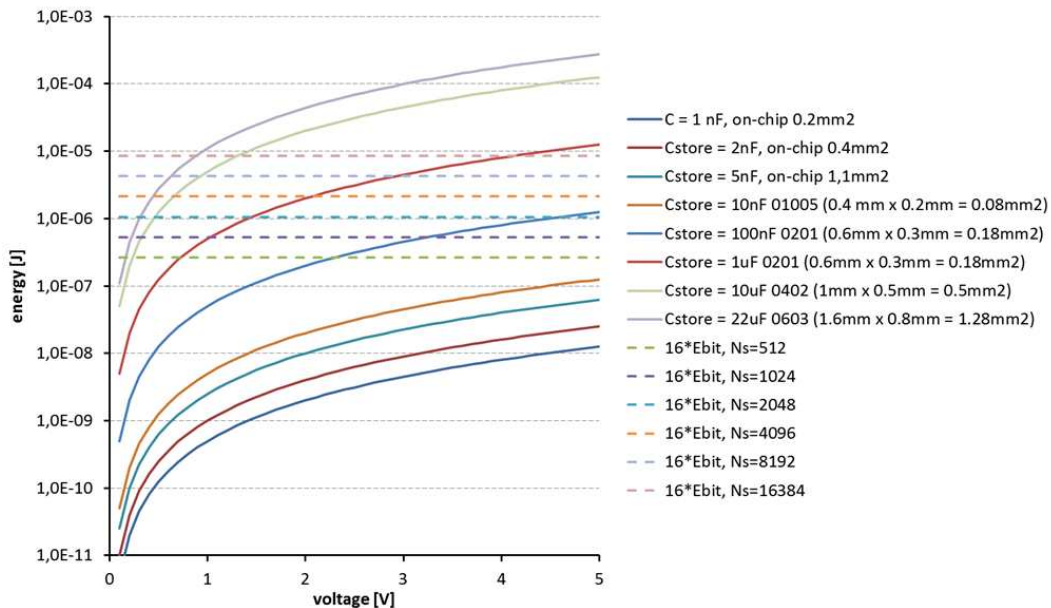


Figure 92: Comparison of energy requirement for transmitting 1 bit of information with the energy stored on the output capacitor as a function of its voltage.

5 DEMONSTRATOR DEFINITION

Among the objectives that the GRETA project has to accomplish, there is the development of an experimental test-bed which shows the feasibility of the main idea behind the project. This will be accomplished in 2 steps: first local test beds at some partners' premises will be set up to test separately single components and functionalities; then an integrated and final test bed will be built at UNIBO providing the final GRETA demonstrator. In Fig. 93 the main contributions to the development of system components are illustrated. In the following the preliminary local test beds and facilities will be briefly described.

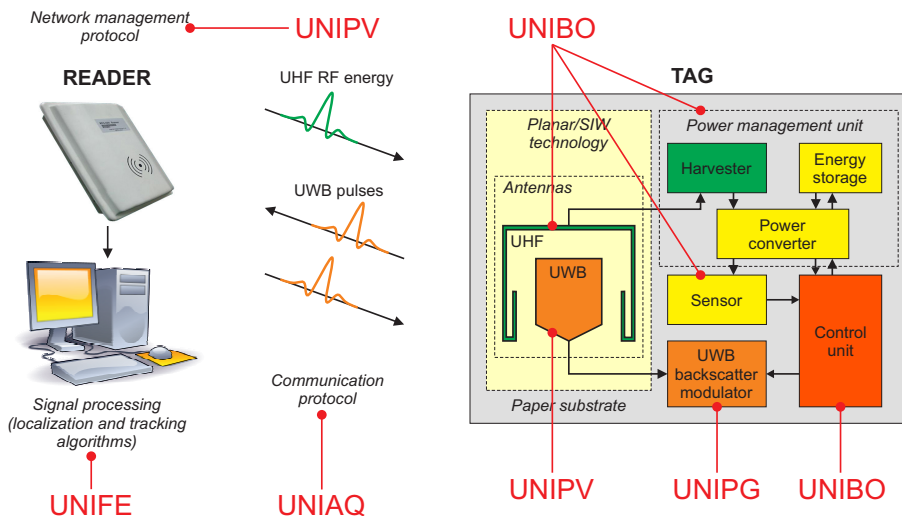


Figure 93: Contributions.

5.1 University of Bologna

A preliminary test-bed is shown in Fig. 94, and its main purpose is to provide a measurement campaign both at UWB and UHF bands. The purpose is to test energy harvesting components and UWB backscatter properties of UWB antennas.

The test-bed is composed as follows:

- transmitter section: it includes an arbitrary waveform generator (tektronik AWG7122G 12 Gs/s), an UWB and UHF amplifier and antennas;
- receiver section: it consists of an UWB antenna and amplifier, an oscilloscope (tektronik TDS 6604) to analyze the received waveform;
- tag section: it is divided in a UHF and a UWB sections interconnected to each other. The UHF part contains an antenna, an energy harvester and a microcontroller while the UWB part mainly consist of an UWB switch.

5.2 University of Ferrara

The proposed measurement set-up, realized with the instruments which are at disposal at University of Bologna at Cesena, can be tested in an ideal and controlled environment as the anechoic chamber which is in the laboratory of the University of Ferrara. Once the system has been tested, further measurements will be carried out in real indoor environments.

5.3 University of Perugia

Available measuring equipment:

- 30 square meter clean room (1000 class under laminar air-flow);

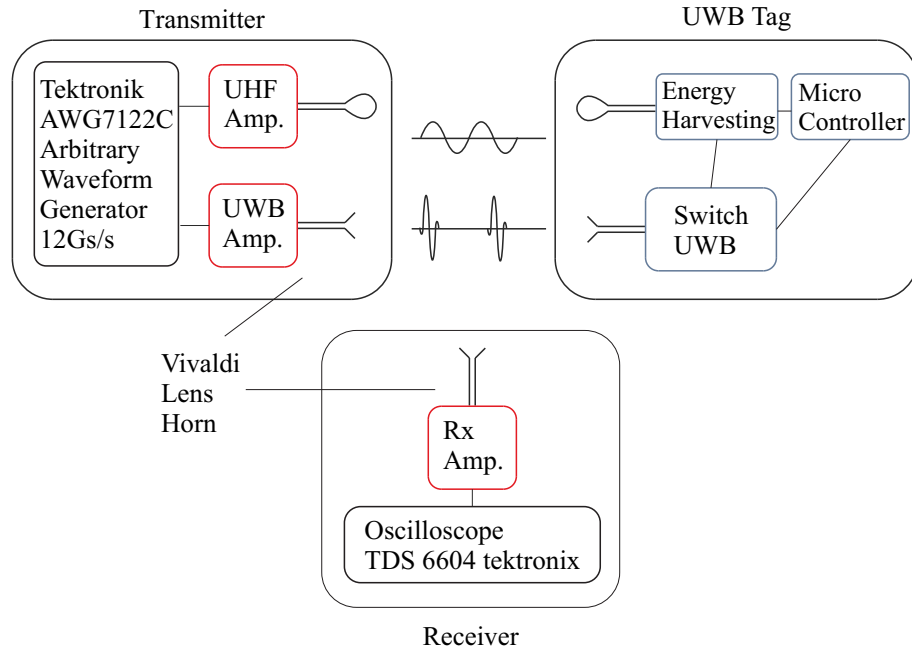


Figure 94: Test Bed Architecture.

- manual WEST-BOND wedge-bonding machine;
- semiautomatic ALESSI probe station equipped with micromanipulators, 50Ohm coplanar probes for on-wafer measurements up to 40GHz and CASCADE calibration substrate;
- Agilent E4407B 9kHz-26.5GHz Spectrum Analyser;
- Vector Network Analyser Agilent PNA N52230A 10MHz-40GHz equipped with a K coaxial calibration kit;

6 DISSEMINATION ACTIVITY

In this section the dissemination activity carried out and planned by the research units is reported.

6.1 University of Bologna

Papers

- M. Dini, M. Filippi, A. Costanzo, A. Romani, M. Tartagni, M. Del Prete, D. Masotti, "A Fully-Autonomous Integrated RF Energy Harvesting System for Wearable Applications", Proceedings of 43rd European Microwave Conference (EuMC) (Nuremberg), 6-11 ottobre 2013, pp. 987-990, ISBN 978-2-87487-031-6 (invited paper)
- D. Masotti, A. Costanzo, P. Francia, M. Filippi, A. Romani, "A Load-modulated Rectifier for RF Micropower Harvesting with Start-up Strategies", IEEE Trans. Microwave Theory Tech., to be published on Feb 2014 issue (invited paper)
- V. Zambianchi, E. Paolini, and D. Dardari, "Information transmission via source of opportunity signals: Piggyback communications," in IEEE International Conference on Communications (ICC), Budapest, Hungary, Jun. 2013.
- N. Decarli and D. Dardari, "RFID and radar localization: A position error bound analysis," in IEEE International Conference on Communication (ICC), Budapest, Hungary, Jun. 2013.
- N. Decarli, F. Guidi, and D. Dardari, "A novel joint RFID and radar sensor network for passive localization: Design and performance bounds," IEEE Journal of Selected Topics in Signal Processing, Special Issue on Non-cooperative Localization Networks, 2013.
- N. Decarli, A. Guerra, A. Conti, R. D'Errico, A. Sibile, and D. Dardari, "Non-regenerative relaying for enhanced network localization," IEEE Transaction on Wireless Communications, 2014
- B. Sobhani, E. Paolini, A. Giorgetti, M. Mazzotti, and M. Chiani, "Target tracking for UWB multi-static radar sensor networks," IEEE Journal of Selected Topics in Signal Processing, Special Issue on Non-cooperative Localization Networks, 2013.
- B. Sobhani, M. Mazzotti, E. Paolini, A. Giorgetti, and M. Chiani, "Effect of state space partitioning on bayesian tracking for UWB radar sensor networks," in 2013 IEEE International Conference on Ultra-Wideband (ICUWB), Sept 2013.
- M. Del Prete, D. Masotti, M. Dini, M. Filippi, A. Costanzo, A. Romani and M. Tartagni, "A Fully-Autonomous Integrated RF Energy Harvesting System for Wearable Applications", 2013 EuMC European Microwave Week, Oct 2013.
- A. Costanzo and D. Masotti, "Design of RF energy harvesting platforms for power management unit with start-up circuits", PowerMEMS (13th International Conference on Micro and Nanotechnology for Power Generation and Energy Conversion Applications), London Dec. 2013.

Presentations

- GTTI/SIEM workshop Ancona 24-26 June 2013 (Chiani)
- GRETA Project presentation at RAI TG3 (Chiani)
- GRETA Project presentation at ClassTV (Dardari)
- GRETA Project presentation at Packology, Rimini 11-14 Giugno (Costanzo)
- Organization of the IEEE Workshop on Advances in Network Localization and Navigation (ANLN) at ICC 2013, Budapest, June 9-13 (Dardari)
- Seminar at Université Catholique Louvain, 3/7/2013 (Dardari)
- Organization of the EUMW Roma Workshop, October 2014 (Costanzo)
- Organization of the IEEE 2nd Workshop on Advances in Network Localization and Navigation (ANLN) at ICC 2014, Sidney, 2014 (Dardari)

6.2 University of Ferrara

- N. Decarli, A. Guerra, A. Conti, R. D'Errico, A. Sibile, and D. Dardari, "Non-regenerative relaying for enhanced network localization," IEEE Transaction on Wireless Communications, 2013, in publication.
- A. Conti, D. Dardari, M. Guerra, L. Mucchi, and M. Z. Win, "Experimental Characterization of Diversity Navigation," IEEE Systems Journal, 2013, in publication.
- S. Bartoletti, A. Giorgetti, and A. Conti, "Sensor Radars with Subset Diversity," in IEEE International Conference on Communication (ICC), Budapest, Hungary, Jun. 2013.

6.3 University of L'Aquila

The University of L'Aquila plans to submit papers to major journals and conferences in the area of wireless communications for the whole duration of the project: IEEE Transactions on Communications, IEEE Transactions on Wireless Communications and IEEE Transactions on Vehicular Technology are retained as major archival journals, while IEEE ICC, IEEE Globecom, IEEE WCNC and IEEE ICUWB are considered major conferences for disseminating our results.

The following papers have been published or accepted for publication:

- P. Di Marco, C. Fischione, F. Santucci, and K.H. Johansson, *Modeling IEEE 802.15.4 networks over fading channels*. IEEE Transactions on Wireless Communications (accepted with minor revision).
- N. Rendevski and D. Cassioli, *BER of IEEE 802.11ad OFDM Radios vs. Carrier Frequency in Real 60 GHz Indoor Channels*, ICC 2014, Sydney, Australia, June 2014. (to be presented)
- D. Cassioli and N. Rendevski, *A Statistical Model for the Shadowing Induced by Human Bodies in the Proximity of a mmWaves Radio Link*, ICC 2014 WS on 5G, Sydney, Australia, June 2014. (to be presented)
- M. Vari and D. Cassioli, *mmWaves RSSI Indoor Network Localization*, ICC 2014 WS on ANLN, Sydney, Australia, June 2014. (to be presented)
- P. Di Marco, F. Santucci, and C. Fischione, *Modeling anti-collision protocols for RFID systems with multiple access interference*, IEEE ICC 2014, Sydney, Australia. June 2014. (to be presented)
- R. Alesii, R. Congiu, F. Santucci, P. Di Marco, and C. Fischione, *Architectures and protocols for fast identification in large-scale RFID systems*, IEEE ISCCSP 2014, Athens, Greece. May 2014. (to be presented)
- P. Di Marco, C. Fischione, F. Santucci, and K.H. Johansson, *Effects of Rayleigh-lognormal fading on IEEE 802.15.4 networks*. IEEE ICC 2013, Budapest, Hungary. June 2013.
- M. Di Renzo, C. Merola, A. Guidotti, F. Santucci, and G.E. Corazza, *Error Performance of Multi-Antenna Receivers in a Poisson Field of Interferers: A Stochastic Geometry Approach*, IEEE Transactions on Communications, Vol.:61 Issue:5 Pag.:2025 -2047, May 2013.
- A. Guidotti, V. Buccigrossi, M. Di Renzo, G.E. Corazza, and F. Santucci, *Outage and symbol error probabilities of dual-hop AF relaying in a Poisson field of interferers*, IEEE WCNC 2013, April 2013.

In addition, the following presentation is reported:

- D. Cassioli, *Millimeter-waves wireless communications*, XI International Conference ETAI 2013, Ohrid, Macedonia. 26-28 Sept. 2013. Plenary Talk.

6.4 University of Pavia

The TLC and RS group of the University of Pavia intends to submit papers to the following conferences and journals: ICC 2015 and/or GLOBECOM 2015, IEEE Trans. on Wireless Communications and/or IEEE Trans. on Communications.

- R. Moro, S. Kim, M. Bozzi, M. Tentzeris, "Inkjet-Printed Paper-Based Substrate Integrated Waveguide (SIW) Components and Antennas," International Journal of Microwave and Wireless Technologies, Vol. 5, No. 3, pp. 197–204, June 2013.
- S. Kim, B. Cook, T. Le, J. Cooper, H. Lee, V. Lakafosis, R. Vyas, R. Moro, M. Bozzi, A. Georgiadis, A. Collado, and M. Tentzeris, "Inkjet-printed Antennas, Sensors and Circuits on Paper Substrate," IET Microwaves, Antennas and Propagation, Vol. 7, No. 10, pp. 858–868, July 16, 2013.
- M. Bozzi, "Substrate Integrated Waveguide (SIW) Technology for the Next Generation of Microwave and mm-Wave Systems," 34th Progress in Electromagnetics Research Symposium (PIERS 2013), Stockholm, Sweden, August 12-15, 2013 (invited paper).
- S. Kim, R. Moro, M. Bozzi, S. Nikolaou, M. Tentzeris, "Inkjet-printed Wearable Microwave Components for Biomedical Applications," 7th European Conference on Antennas and Propagation (EUCAP 2013), Gothenburg, Sweden, April 8–12, 2013.
- R. Moro, S. Kim, M. Bozzi, and M. M. Tentzeris, "Implementation of Substrate Integrated Waveguide (SIW) by Inkjet-printing on Paper Substrate," 34th Progress in Electromagnetics Research Symposium (PIERS 2013), Stockholm, Sweden, August 12-15, 2013.
- M. Bozzi and R. Moro, "Low-Cost Fabrication, Eco-Friendly Materials, and Easy Integration: the New Technological Paradigm for the Future Wireless Sensor Networks," 43rd European Microwave Conference (EuMC2013), Nuremberg, Germany, Oct. 6-11, 2013.
- M. Bozzi and R. Moro, "SIW Components and Antennas Based on Eco-friendly Materials and Technologies: State-of-the-Art and Future Applications," IEEE Topical Conference on Wireless Sensors and Sensor Networks (WiSNet2014), Newport Beach, CA, USA, Jan. 19-22, 2014.
- P. Gamba, E. Goldoni, P. Savazzi, P.G. Arpesi, C. Sopranzi, J. Durfour, "Wireless Passive Sensors for Remote Sensing of Temperature on Aerospace Platforms", WiSEE 2013

6.5 University of Perugia

The main focus of the University of Perugia research team is the design of the backscatter modulator described in section 3.5. The results expected from this activity research are the design and the measures performed on the on-chip prototype.

The dissemination plan will be the following:

- submitted paper to IEEE International Microwave Symposium 2014;
- submitted paper to IET Science, Measurement & Technology Journal;
- further submissions of journal paper to IEEE Journal of Solid-State Circuits and/or IEEE Microwave and Wireless Components Letters; submission of conference paper to IEEE International Microwave Symposium 2014 and/or IEEE RFID-Technologies and Applications 2014.
- F. Alimenti, L. Roselli, "Theory of Zero-Power RFID Sensors Based on Harmonic Generation and Orthogonally Polarized Antennas," Progress in Electromagnetic Research, vol. 134, 2013, pp. 337-357.
- F. Alimenti, C. Mariotti, P. Mezzanotte, M. Dionigi, M. Virili, L. Roselli, "A 1.2 V, 0.9 mW UHF VCO Based on Hairpin Resonator in Paper Substrate and Cu Adhesive Tape," IEEE Microwave and Wireless Component Letters, vol. 23, n. 4, April 2013, pp. 214-216.
- L. Valentini, M. Cardinali, M. Mladjenovic, P. Uskokovic, F. Alimenti, L. Roselli, J. Kenny, "Flexible Transistors Exploiting P3HT on Paper Substrates and Graphene Oxide Films as Gate Dielectrics: Proof of Concept," Science of Advanced Materials, vol. 5, n. 5, May 2013, pp. 1-4.
- S. Kim, C. Mariotti, F. Alimenti, P. Mezzanotte, A. Georgiadis, A. Collado, L. Roselli, M.M. Tentzeris, "No Battery Required: Perpetual RFID-Enabled Wireless Sensors for Cognitive Intelligence Applications," IEEE Microwave Magazine, vol. 14, n. 5, July-August 2013, pp. 66-77.
- F. Alimenti, P. Mezzanotte, S. Giacomucci, M. Dionigi, C. Mariotti, M. Virili, L. Roselli, "24-GHz Single-Balanced Diode Mixer Exploiting Cellulose-Based Materials," IEEE Microwave and Wireless Components Letters (to appear).

- M. Virili, F. Alimenti, L. Roselli, P. Mezzanotte, M. Dionigi (2013). Organic frequency doubler RFID tag exploiting 7.5-MHz wireless power transfer 2013 IEEE Wireless Power Transfer (WPT). Proceedings of 2013 IEEE Wireless Power Transfer (WPT) 33- 36, In:2013 IEEE Wireless Power Transfer (WPT). 15-16 May 2013, Perugia.
- L. Aluigi, T.T. Thai, M.M. Tentzeris, L. Roselli, F. Alimenti (2013). Chip-to-package wireless power transfer and its application to mm-Wave antennas and monolithic radiometric receivers 2013 IEEE Radio and Wireless Symposium. Proceedings of 2013 IEEE Radio and Wireless Symposium 202- 204, In:2013 IEEE Radio and Wireless Symposium. 20-23 January 2013, Austin, TX.
- L. Valentini, J. M. Kenny, F. Alimenti, L. Roselli, "Planar MOSFET Devices on Paper Substrate Using Graphene Oxide Film as Gate Dielectric", in Proc. of European Microwave Conference 2013, 6-11 Oct. 2013, Nuremberg, GE
- C. Mariotti, F. Alimenti, P. Mezzanotte, M. Virili, S. Giacomucci, L. Roselli, "Modeling and characterization of copper adhesive tape microstrips on paper substrates", in Proc. of European Mi- crowave Conference 2013, 6-11 Oct. 2013, Nuremberg, GE

REFERENCES

- [1] D. Dardari, N. Decarli, A. Guerra, and A. Conti. Enhanced localization coverage with non-regenerative UWB relays. In *20th European Signal Processing Conf. (EUSIPCO)*, Bucharest, Romania, Aug. 2012.
- [2] N. Decarli, A. Guerra, A. Conti, R. D'Errico, A. Sibille, and D. Dardari. Non-regenerative relaying for network localization. *IEEE Trans. Wireless Commun.*, PP(99):1–12, 2013.
- [3] N. Decarli, F. Guidi, and D. Dardari. A novel joint RFID and Radar sensor network for passive localization: Design and performance bounds. *IEEE J. of Selected Topics in Signal Processing*, February 2014.
- [4] N. Decarli, F. Guidi, A. Conti, and D. Dardari. Interference and clock drift effects in UWB RFID systems using backscatter modulation. In *IEEE Int. Conf. on Ultra-Wideband (ICUWB)*, pages 1–5, Syracuse, USA, sep 2012.
- [5] F. Guidi, N. Decarli, D. Dardari, C. Roblin, and A. Sibille. Performance of UWB backscatter modulation in multi-tag RFID scenario using experimental data. In *IEEE Int. Conf. on Ultra-Wideband (ICUWB)*, pages 484 –488, sept. 2011.
- [6] D. Dardari, R. D'Errico, C. Roblin, A. Sibille, and M.Z. Win. Ultrawide Bandwidth RFID: The Next Generation? *Proc. IEEE*, 98(9):1570 –1582, 2010.
- [7] D. Dardari, F. Guidi, C. Roblin, and A. Sibille. Ultra-wide bandwidth backscatter modulation: Processing schemes and performance. *EURASIP J. on Wireless Commun. and Networking*, 2011:47(1), 2011.
- [8] F. Guidi, D. Dardari, C. Roblin, and A. Sibille. Backscatter communication using ultrawide bandwidth signals for RFID applications. In *D. Giusto et al. (eds.), The Internet of Things: 20th Tyrrhenian Workshop on Digital Communications*, pages 251–262, Pula, Sardinia, ITALY, September 2009.
- [9] IEEE standard for information technology - telecommunications and information exchange between systems - local and metropolitan area networks - specific requirement part 15.4: Wireless medium access control (MAC) and physical layer (PHY) specifications for low-rate wireless personal area networks (WPANs). *IEEE Std 802.15.4a-2007 (Amendment to IEEE Std 802.15.4-2006)*, pages 1–203, 2007.
- [10] EPCGlobal. Class 1 generation 2 UHF air interface protocol standard v.1.0.9. 2005.
- [11] Biqi Long, Ping Zhang, and Jiandong Hu. A generalized QS-CDMA system and the design of new spreading codes. *IEEE Trans. Vehicular Tech.*, 47(4):1268 –1275, nov 1998.
- [12] A. Goldsmith. *Wireless Communications*. Cambridge University Press, 2005.
- [13] H. Donelan and T. O'Farrell. Method for generating sets of orthogonal sequences. *Electronics Letters*, 35(18):1537 –1538, sep 1999.
- [14] R. De Gaudenzi, C. Elia, and R. Viola. Bandlimited quasi-synchronous cdma: a novel satellite access technique for mobile and personal communication systems. *IEEE J. Selected Areas in Commun.*, 10(2):328 –343, feb 1992.
- [15] A.F. Molisch, K. Balakrishnan, D. Cassioli, C-C. Chong, S. Emami, A. Fort, J. Karedal, J. Kunisch, H. Schantz, U. Schuster, and K. Siwiak. IEEE 802.15.4a channel model - final report. 2005.
- [16] Chi Xu and ChoiL Law. Toa estimator for uwb backscattering rfid system with clutter suppression capability. *EURASIP Journal on Wireless Communications and Networking*, 2010(1):753129, 2010.

- [17] Chonggang Wang, M. Daneshmand, K. Sohraby, and Bo Li. Performance analysis of RFID generation-2 protocol. *IEEE Transactions on Wireless Communications*, 8(5):2592–2601, 2009.
- [18] M. Mohaisen, HeeSeok Yoon, and KyungHi Chang. Radio transmission performance of epcglobal gen-2 rfid system. In *Advanced Communication Technology, 2008. ICACT 2008. 10th International Conference on*, volume 2, pages 1423–1428, 2008.
- [19] Alexey Borisenko, Miodrag Bolic, and Majed Rostamian. Intercepting uhf rfid signals through synchronous detection. *EURASIP Journal on Wireless Communications and Networking*, 2013(1):214, 2013.
- [20] Yu-Shiang Lin, D Sylvester, and D. Blaauw. An ultra low power 1V, 220nW temperature sensor for passive wireless applications. pages 507–510, Sept 2008.
- [21] A.K. Poddar, U.L. Rohde, and A.M. Apte. How Low Can They Go?: Oscillator Phase Noise Model, Theoretical, Experimental Validation, and Phase Noise Measurements. *IEEE Microwave Magazine*, 14(6):50–72, Sept 2013.
- [22] V. De Smedt, P. De Wit, W. Vereecken, and M.S.J. Steyaert. A $66 \mu \text{W}$ 86 ppm / $^{\circ} \text{C}$ Fully-Integrated 6 MHz Wienbridge Oscillator With a 172 dB Phase Noise FOM. *IEEE Journal of Solid-State Circuits*, 44(7):1990–2001, July 2009.
- [23] U. Denier. Analysis and Design of an Ultralow-Power CMOS Relaxation Oscillator. *IEEE Transactions on Circuits and Systems Part I: Regular Papers*, 57(8):1973–1982, Aug 2010.
- [24] van Tuijl E. J. M. Klumperink E. A. M. Wienk G. J. M. Geraedts, P. F. J. and B. Nauta. Towards minimum achievable phase noise of relaxation oscillators. *Int. J. Circ. Theor. Appl.*, 2012, 2012.
- [25] G. De Vita, F. Bellatalla, and G. Iannaccone. Ultra-low power {PSK} backscatter modulator for {UHF} and microwave {RFID} transponders. *Microelectronics Journal*, 37(7):627 – 629, 2006.
- [26] H.J. Visser and R.J.M. Vullers. Wireless sensors remotely powered by rf energy. pages 1–4, 2012.
- [27] Kin-Lu Wong. Planar antennas for wireless communications. 2003.
- [28] B. Wang and A. Chen. Design of an archimedean spiral antenna. pages 348–351, 2008.
- [29] W. Wiesbeck, G. Adamiuk, and C. Sturm. Basic properties and design principles of uwb antennas. *Proceedings of the IEEE*, 97(2):372–385, february 2009.
- [30] ETSI EN 300 440-1 V1.5.1. Electromagnetic compatibility and radio spectrum matters (erm); short range devices; radio equipment to be used in the 1 ghz to 40 ghz frequency range. march 2009.
- [31] ETSI EN 302 208-1 V1.1.2. Electromagnetic compatibility and radio spectrum matters (erm); radio frequency identification equipment operating in the band 865 mhz to 868 mhz with power levels up to 2 w. march 2006.
- [32] S. Qu, C. Ruan, and Q. Xue. A planar folded ultrawideband antenna with gap-loading. *IEEE Transactions on Antennas and Propagation*, 55(1):216–220, january 2007.
- [33] C. Ding, C. Ruan, L. Peng, and J. Chu. A novel archimedean spiral antenna with uniplanar ebg substrate. 2008.
- [34] <http://fabriano.com/>.
- [35] <http://www.cartieramomo.com/>.
- [36] <http://burgopapers.com/>.

- [37] F. Lolli, M. Virili, G. Orecchini, M. Dionigi, F. Alimenti, P. Mezzanotte, and L. Roselli. Electromagnetic characterization of paper-glue compound for system-in-package on paper (sipop) future developments. *IEEE Microwave and Wireless Components Letters*, 22(10):545–547, Oct 2012.
- [38] Li Yang, A. Rida, R. Vyas, and M.M. Tentzeris. Rfid tag and rf structures on a paper substrate using inkjet-printing technology. *IEEE Transactions on Microwave Theory and Techniques*, 55(12):2894–2901, Dec 2007.
- [39] Ramesh Garg, Inder Bahl, and Maurizio Bozzi. *Microstrip Lines and Slotlines, Third Edition*. Artech House, 2013.
- [40] M. Bozzi, L. Perregrini, and Ke Wu. Modeling of conductor, dielectric, and radiation losses in substrate integrated waveguide by the boundary integral-resonant mode expansion method. *IEEE Transactions on Microwave Theory and Techniques*, 56(12):3153–3161, 2008.
- [41] L. Perregrini M. Bozzi, M. Pasian and K. Wu. On the losses in substrate integrated waveguides and cavities. *International Journal of Microwave and Wireless Technologies*, 1(5):395–401, Oct 2009.
- [42] N. Grigoropoulos, B. Sanz-Izquierdo, and P.R. Young. Substrate integrated folded waveguides (sifw) and filters. *IEEE Microwave and Wireless Components Letters*, 15(12):829–831, Dec 2005.
- [43] B. Sanz Izqueirdo, N. Grigoropoulos, and P.R. Young. Ultra-wideband multilayer substrate integrated folded waveguides. In *Microwave Symposium Digest, 2006. IEEE MTT-S International*, pages 610–612, June 2006.
- [44] Wei Hong, Bing Liu, Yuanqing Wang, Qinghua Lai, Hongjun Tang, Xiao-Xin Yin, Yuan-Dan Dong, Yan Zhang, and Ke Wu. Half mode substrate integrated waveguide: A new guided wave structure for microwave and millimeter wave application. In *Infrared Millimeter Waves and 14th International Conference on Terahertz Electronics, 2006. IRMMW-THz 2006. Joint 31st International Conference on*, pages 219–219, Sept 2006.
- [45] F. Gustafsson, F. Gunnarsson, N. Bergman, U. Forssell, J. Jansson, R. Karlsson, and P.-J. Nordlund. Particle filters for positioning, navigation, and tracking. *IEEE Trans. Signal Processing*, 50:425–437, February 2002.
- [46] C. Mutti and C. Floerkemeier. CDMA-based RFID systems in dense scenarios: Concepts and challenges. pages 215–222, Las Vegas, USA, April 2008.
- [47] Andreas Loeffler. Using cdma as anti-collision method for rfid - research & applications. In Prof. Cornel Turcu, editor, *Current Trends and Challenges in RFID*. InTech, 2011.
- [48] ISO 18000 Part 6. Information technology automatic identification and data capture - radio frequency identification for item management air interface. 2003.
- [49] Joseph M. Aein. Multiple access to a hard-limiting communication-satellite repeater. *Space Electronics and Telemetry, IEEE Transactions on*, 10(4):159–167, 1964.
- [50] Davide Dardari, Francesco Guidi, Christophe Roblin, and Alain Sibille. Ultra-wide bandwidth backscatter modulation: Processing schemes and performance. *EURASIP Journal on Wireless Communications and Networking*, 2011:47(1), 2011.
- [51] Andrea Goldsmith. *Wireless Communications*. Cambridge University Press, 2005.
- [52] Abdelkrim Hamza and Gerard Salut. Idma based anti-collision in rfid networks. *International Journal of Wireless Information Networks*, 20(3):235–240, 2013.
- [53] Solomon W. Golomb. *Shift Register Sequences*. Aegean Park Pr, 1981.

- [54] Hsiao-Hwa Chen. *The Next Generation CDMA Technologies*. Wiley, 2007.
- [55] Theodore S. Rappaport. *Wireless Communications: Principles and Practice (2nd Edition)*. Prentice Hall, 2002.
- [56] F. Guidi, A. Sibille, and C. Roblin. Interaction of uwb tag backscattering with close metallic reflectors. *IEEE Antennas Wireless Propagat. Lett.*, In publication 2014.